# MEASUREMENTS OF FLUCTUATING AIR LOADS

## ON A CIRCULAR CYLINDER

Thesis by

Louis Vincent Schmidt

In Partial Fulfillment of the Requirements

For the Degree of

Doctor of Philosophy

California Institute of Technology

Pasadena, California

1963

## ACKNOWLEDGMENT

This work is dedicated to the memory of our daughter, Tina Marie.

# ABSTRACT

Measurements were made of the unsteady air loads, both lift and drag, developed on a circular cylinder when exposed to flow in the supercritical Reynolds number range from $0.38 \times 10^6$ to $0.75 \times 10^6$. The three dimensional nature of the flow, which is a consequence of the flow separation effects, is recognized. The statistical character of spatially varying random type fluctuating air loads is presented in the form of cross-spectral densities and cross-correlation coefficients. Information of this type has application to the problem of determining the response of a cylindrical structure when exposed to air loads.

The extreme sensitivity of the flow to surface irregularities in the supercritical Reynolds number region is reported including the effects upon the local and spatial character of the fluctuating loads. Local values of steady state lift could be induced by suitably orienting surface disturbances on the forward portion of the cylinder.

# TABLE OF CONTENTS

# LIST OF FIGURES

LIST OF FIGURES (cont'd)

Figures in Appendix

LIST OF FIGURES (cont'd)

## NOTATION

A. List of Symbols:

D    Diameter of cylinder

f    Frequency, cycles per second

$P_x$    Static pressure at location (x)

q    Dynamic pressure, $q = \frac{1}{2} \rho V^2$

t    Time

V    Velocity of undisturbed flow

x    Axial coordinate along cylinder axis, $x = 0$ at the base

$\rho$    Mass density of fluid

$\nu$    Kinematic viscosity of fluid

$\gamma$    Ratio of damping to the critical damping

$\tau$    Time lag

$\theta$    Angular coordinate for cylinder surface, zero reference

    is forward stagnation point

$\phi$    Power spectral density

$\Phi$    Co-spectral density, real part of cross-spectra

$\Psi$    Quad-spectral density, imaginary part of cross-spectra

$\chi$    Correlation length, dimensionless

Note:   Other symbols are defined in text when introduced.

B. Superscripts:

$\overline{(\ )}$   Mean average, equals $\displaystyle \lim_{T \to \infty} \frac{1}{2T} \int_{-T}^{T} (\ )\, dt$

C.  Subscripts:

$( )_{\ell^2}$        Refers to lift at station $x_1$ and to lift at station $x_2$

$( )_{d^2}$        Refers to drag at station $x_1$ and to drag at station $x_2$

$( )_n$        Refers to normalized term, applicable to $\phi$,    , and

D.  Dimensionless coefficients:

$C_L$        Local lift force coefficient $= \dfrac{\text{Lift force/unit span}}{qD}$

$C_D$        Local drag force coefficient $= \dfrac{\text{Drag force/unit span}}{qD}$

$C_p$        Static pressure coefficient $= \dfrac{P_x - P_{ref.}}{q}$

R        Reynolds number of cylinder $= VD/\gamma$

S        Strouhal number (non-dimensional frequency) $= fD/V$

# SECTION I

## INTRODUCTION

The flow of an incompressible viscous fluid past a circular cylinder has been the subject of numerous studies through the years, but in spite of the basic simplicity of the geometric form, problem areas still remain that are difficult to treat analytically or to measure experimentally. One of these areas of interest relates to the fluctuating lift and drag loads that a circular cylinder experiences when placed in a flow normal to its axis of symmetry, as a consequence of the fluctuating pressures acting on the cylinder.

The ability of the wind to produce vibrations in wires (Aeolian tones) has been know for a long time. It was Strouhal (1) who first showed in 1878 that the frequency of these tones was directly proportional to the relative air velocity and inversely proportional to wire diameter. When the frequency of the tone coincided with a wire resonance frequency, the sound level was reinforced. Further understanding was provided by Lord Rayleigh (2) in 1879. In a classically simple experiment, he disclosed that the motion of a taut string, when exposed to a chimney draught, was in a direction perpendicular to the air velocity, a result which was thought to be quite remarkable at the time.

The periodic nature of the wake was established later. It was in 1911 that von Karman (3) related his theory of the vortex street which initiated many investigations of the wake behind bluff bodies. Outstanding among the problems outlined in von Karman's stability

papers was the problem of the mechanism controlling periodic
vortex shedding. There is still no suitable theoretical treatment
for this problem. The literature on the subject of vortex shedding
behind cylinders is quite extensive, with notable reviews being given
by Goldstein (4) in 1938, Rosenhead (5) in 1953, and Humphreys (6)
in 1959.

The vortex shedding phenomena can be considered in terms
of the cylinder Reynolds number, R, which is a dimensionless
number expressing the interaction of viscous and inertial forces in
a flow for geometrically similar bodies. The regions of interest will
be classified in order of increasing Reynolds number as subcritical,
supercritical, and transcritical in a manner proposed by Roshko (7)
in 1960. These regions are separated by transition zones, with the
lower, or critical, transition occurring in the range of $2 \times 10^5 <$
$R < 5 \times 10^5$ while the upper transition occurs in the range of
$1 \times 10^6 < R < 3.5 \times 10^6$. In the subcritical regime, the character
of the flow in the wake is predominantly periodic, and a laminar flow
separation occurs on the cylinder forward of the maximum thickness
point. The supercritical flow regime is characterized by a more
turbulent wake without the appearance of any dominant frequencies,
and the flow separation point has moved rearward in the manner of
turbulent separation. In the range of transcritical flows, Roshko (7)
has observed that the wake exhibits periodicity and the separation is
turbulent.

The steady state values of drag force coefficient, $C_D$,
exhibit well known traits in these flow ranges. In the subcritical

range ($1 \times 10^3 < R < 3 \times 10^5$), the value of $C_D$ is between 1.0 and 1.2; $C_D$ drops markedly in the lower transition zone such that it attains a value of $C_D = 0.25$ to $0.35$ in the supercritical range; and the value of drag begins to rise in the upper transition zone until a steady value of $C_D = 0.7$ is obtained in the transcritical flow range.

The character of the fluctuating loads can be described in a parallel manner by classification according to flow ranges. Based on observations made in the subcritical Reynolds number range (e.g., Macovsky (8) and Keefe (9)), it has been found that the unsteady lift load is of the same order of magnitude as the steady state drag value while the unsteady component of drag is an order of magnitude lower. It was Fung (10) in 1958 who first presented measurements in the supercritical range. His results showed that in comparison to values in the subcritical range the fluctuating lift load had decreased in value while the unsteady drag was relatively unaltered. In the subcritical range, the unsteady loads are periodic in nature and have a non-dimensional frequency (Strouhal number), $S = 0.2$. As the lower transition is approached, the fluctuating loads begin to exhibit a random modulation of amplitude. In the supercritical range, the unsteady loads lose signs of periodicity and are best described using power spectrum concepts.

The knowledge of fluctuating loads in the supercritical (and transcritical) flow regions has engineering application to current problems of import dealing with the response of large cylindrical objects such as smokestacks and missiles on launch pads, when exposed to surface winds. In general, it has been reported

(References 11 and 12) that the response of a smokestack smoothly increases with increasing wind velocity (primarily responding in a direction normal to the wind velocity) and that the frequency of the motion remains constant at the smokestack's fundamental value. This suggests that the structure behaves as a narrow band-pass filter and is responding to forces which are random in nature. The physics governing smokestack vibrations is also applicable to missiles on open launch pads. In the case of missiles, structural weight is quite critical, which in turn places more emphasis on understanding the problem. Ezra and Birnbaum (13) have reported in 1960 the results of wind-tunnel measurements made on a dynamically similar model. One of the highlights of their measurements is the strong dependence of the root bending moment upon nose shape. They showed that the unsteady loads on a cantilevered cylindrical body could be modified by nose configuration. However, their measurements do not yield any information with respect to the spanwise distribution of fluctuating load.

Macovsky (8) in 1958 noted that the unsteady lift loads on a two-dimensional cylinder model were three-dimensional in character. Investigations by Keefe (9) in 1961 showed that altering the axial location of chordwise fences had a noticable effect upon the fluctuating forces. The results of Macovsky and Keefe in the subcritical range are in accord with the observations made by Fung (10) in the supercritical range, namely "that the axial correlation of the fluctuating forces are important and that significant changes can be induced by end effects and by small axial geometrical perturbations". The

instrumentation used by previous investigators had limitations since it has not been possible in the past to evaluate the axial correlation of unsteady loads, even though the three-dimensional nature of flow over a two-dimensional type circular cylinder has been recognized.

In view of the previous remarks, the purpose of the investigations presented here can be stated as being to establish an experimental technique for measuring unsteady loads and their axial correlation with the intent of applying these methods to the response analysis of a cylindrical structure that is excited by spatially random forcing functions. The background for this problem has been presented by Fung (14) in 1960, including a basic formulation of the structural response equations when the forcing function is a spatially dependent random variable.

A brief description of the experimental equipment is presented in Section II. The results of the experimental measurements are shown in Section III, including the direct readings of air loading, computed values of power and cross-spectral densities, axial correlation data obtained by analog circuit means, and the observed response of the cylinder structure. Detailed descriptions of the experimental techniques used in obtaining and analyzing the air-load data are presented in the Appendix sections.

An interesting by-product of these investigations was the observation that the flow traits in the supercritical Reynolds number range were extremely sensitive to surface condition. Slight surface disturbances produced significant changes in the unsteady air loads

from the standpoint of both RMS level and spectral distribution of power. In addition, asymmetrical flow disturbances resulted in the development of steady-state local lift values.

## SECTION II

## EXPERIMENTAL ARRANGEMENT

The test model was a cantilevered cylinder (8.54 inch diameter) that projected approximately 8.1 cylinder diameters vertically from the floor of the GALCIT[*] Ten-Foot Wind Tunnel test section. The operating range of tunnel air speeds corresponded to cylinder Reynolds numbers from $0.38 \times 10^6$ to $0.75 \times 10^6$. A schematic side view of the installation and a photograph of the installed model is shown on Figures 1 and 2. The model was chosen in the form of a cantilever in order to permit a future evaluation of tip effects upon local air loadings. In the group of investigations reported here, the tip was blunt ended which resulted in the model having a "smokestack" type appearance.

Sectional loads were obtained by means of an electrical summing network applied to eighteen properly oriented static pressure transducers at each of two load stations. The measurements of air load were recorded on magnetic tape for convenience of subsequent data analysis. The data did not require a response correction since the observed frequencies were below 200 cps and the overall system dynamic response was essentially flat in this range. The load instrumentation could be oriented to indicate either lateral (lift) or drag loads.

---

[*] Graduate Aeronautical Laboratories, California Institute of Technology.

The two load stations are defined as channels 1 and 2 for sake of clarity. The channel 2 (reference) load station was kept in a fixed location for all of the results presented here, and this corresponded to measuring local loads at an axial position 4.86 cylinder diameters above the floor. Relocable spacer sections made possible the positioning of the channel 1 load station in various axial positions above channel 2 ranging from adjacent ($^{X}1/_D$ = 5.17) to extreme near to the tip ($^{X}1/_D$ = 6.97). A definition of the instrumentation locations applicable to the data of subsequent sections is presented on Figure 3.

A more complete description of the model, instrumentation, and considerations leading to the choice of instrumentation may be found in Appendix A.

## SECTION III

## RESULTS AND DISCUSSION

### 3.1 Steady-State and Mean Measurements:

The steady state drag values which were measured during the course of the experiments discussed here demonstrate that the model was tested in a supercritical flow regime. The general trait observed was that as Reynolds number increased from $0.38 \times 10^6$ to $0.75 \times 10^6$, $C_D$ increased smoothly from about $0.22$ to $0.27$. A visual proof of operation in the supercritical range was provided by the smear marks left on the cylinder by kerosene and oil particles blown off a cheesecloth filter that was installed on the turning vanes in the low-speed settling section of the wind tunnel. The deposited film on the model showed that the flow separation points were aft of the $\theta = 90^\circ$ location on the cylinder, and that the locus of the flow separation points formed a reasonably straight line parallel to the axis of symmetry. The straightness of the separation line indicates that the joints between model spacer sections did not alter the flow traits.

The measurements of unsteady lift and drag in the supercritical range of $0.38 \times 10^6 < R < 0.75 \times 10^6$ are shown in Figures 4 and 5 respectively. The level of the root mean square value of the lift coefficient was approximately $0.035$ and remained relatively constant in the range of Reynolds numbers investigated. The level of the unsteady drag coefficient was slightly less with the value being approximately $0.030$. These values were all repeatable, but it was found that the unsteady lift was extremely susceptible to surface

roughness. The range of lift values shown as a (☐) represent those measured early during the test when the surface condition, although classified as polished, had not been meticuously rubbed smooth. The lift values eventually settled into a repeatable range providing that the surface condition was maintained. The point shown as a (△) is typical of an occurrence that happened suddenly several times during the course of testing; namely that the RMS level of lift data would increase to a value considerably above the normal level. Subsequent tunnel shutdown and model inspection would frequently disclose a minute indentation on the forward portion of the model instrumentation package, with the estimated average width of the dent usually being approximately 0.005 inches and the estimated height of the slight ridge above surface contour being about 0.001 inch. After a little repolishing to remove the slight ridge, the data level would return to the lower range of values, even though a slight dent remained. Further observations as to the effects of surface irregularities were made and results of these controlled disturbances are reported in Section 3.4.

The values of fluctuating load presented on Figures 4 and 5 are compared with the results obtained by Fung (10), and it can be noted that the unsteady drag terms are in accord, but the fluctuating lift values are about a third of the values that he reported. The measurements of Reference 10 were made in the GALCIT Ten-Foot Wind Tunnel using a test model of 12.6 inch diameter and 6 foot length horizontally supported between two vertical channel beams that spanned the tunnel test section. The model mid-section, 1.75

cylinder diameters in length, measured forces using a strain gage
balance. Since the axial correlation of the random loads was less
than a cylinder diameter in length (discussed in Section 3.3), it
would be expected by using logic similar to that of Keefe (9) that
the RMS level of unsteady total load would be less than the sectional
load (as presumably reported here). However, Fung's model
surface was not polished and these surface irregularities plus the
effects of load cell isolation gaps (0.020 inch wide circumferential
gaps vented to the inside of the model) could have produced inter-
ference effects in a manner to cause total loads to be above those
measured here. Additional support for this conjecture in provided
by the comment in Reference 10 that wake surveys disclosed large
changes in the local wake width due to cracks, surface disturbances,
and end effects.

The values obtained by Keefe (9) in the subcritical Reynolds
number range are included on Figures 4 and 5 for purposes of
comparison. It is felt that these measurements, although they were
made using an one diameter span strain gage load cell, and were
subject to some uncertainties with regard to model end effects, are
representative of the available sectional load data. The RMS values
of fluctuating lift in the range of $5 \times 10^3 < R < 1 \times 10^5$ varied from
0.4 to 0.5 while the unsteady component of drag was an order of
magnitude lower. Keefe noted that the irregular character of the
lift load was a random modulation of amplitude superimposed upon a
periodic signal, and the frequency corresponded to a Strouhal number
of approximately 0.20.

12

Information is not available in the high supercritical range of Reynolds numbers $(R > 1 \times 10^6)$.

### 3.2  Correlations and Spectral Densities:

Typical results are presented in this section relating to estimates of correlations and spectral densities for unsteady lift and drag loads. The estimates were obtained by digital means using techniques as described in Appendix B. The definitions of auto-correlations and power spectral densities for a stationary random process are well established, and clear presentations of these concepts may be found in many texts, e. g., Chapter 8 of Fung (15), Chapter 9 of Tsien (16), and Chapter 6 of James, Nichols, and Phillips (17). The extensions of spectral density concepts to the more general case of cross-spectra of two or more random functions is treated by Press and Tukey (18).

The random loadings on the cylinder are a function of axial position and time, and are expressed as $\ell(x, t)$. It is assumed that the mean average is zero, i. e., $\overline{\ell} = 0$. In the case of drag loading, this assumption corresponds to considering only the unsteady drag term. The cross-correlation is denoted by the term $\overline{\ell(x_1, t) \, \ell(x_2, t+\tau)}$, and is the mean time lagged product of unsteady loads considered as acting at the two axial stations, $x_1$ and $x_2$. It is convenient to distinguish between forward and rearward time lags of the cross-correlation. The restriction that the time shift variable, $\tau$, is greater than or equal to zero allows us to define:

For $\tau \gg 0$,

Forward Cross-Correlation (F.C.C.) $= \overline{\ell(x_1, t) \, \ell(x_2, t+\tau)}$

Rearward Cross-Correlation (R.C.C.) $= \overline{\ell(x_1, t) \, \ell(x_2, t-\tau)}$ $\qquad$ (3.01)

A property of the cross-correlation is that when the spatial variables $x_1$ and $x_2$ become coincident, the forward and rearward cross-correlations become identical due to the assumed stationary property of the random function and are equivalent to the auto-correlation. A Fourier transform may be applied to the cross-correlation in order to yield a cross-spectrum, which is in general complex natured. Let

$\Phi(x_1, x_2, f) \quad =$ Real part of cross-spectral density, called the co-spectral density

$\Psi(x_1, x_2, f) \quad =$ Imaginary part (quadrature term) of cross-spectral density, called quad-spectral density

$f \quad =$ Frequency, cps

$x_1 \text{ or } x_2 \quad =$ Axial location of unsteady loads

Then:

$$\Phi + i\Psi = \frac{1}{2\pi^2} \int_{-\infty}^{\infty} \overline{\ell(x_1, t) \, \ell(x_2, t+\tau)} \, e^{-i2\pi f \tau} d\tau \qquad (3.02)$$

In terms of the forward and rearward cross-correlations, the co- and quad-spectral densities can be expressed by Fourier cosine and sine transforms, respectively:

$$\phi(x_1, x_2, f) = \frac{1}{2\pi^2} \int_0^\infty \left[ R.C.C. + F.C.C. \right] \cos 2\pi f\tau \, d\tau$$

$$\Psi(x_1, x_2, f) = \frac{1}{2\pi^2} \int_0^\infty \left[ R.C.C. - F.C.C. \right] \sin 2\pi f\tau \, d\tau$$

(3.03)

An alternate formulation of the cross-spectral density is obtained when one defines the cross-correlation as:

In-phase Cross-correlation (I.P.C.C.) $= \frac{1}{2} \left[ R.C.C. + F.C.C. \right]$

Out-of-phase Cross-correlation (O.P.C.C.) $= \frac{1}{2} \left[ R.C.C. - F.C.C. \right]$

Then the cross-spectral density can be expressed as:

$$\phi(x_1, x_2, f) = \frac{1}{\pi^2} \int_0^\infty (I.P.C.C.) \cos 2\pi f\tau \, d\tau$$

$$\Psi(x_1, x_2, f) = \frac{1}{\pi^2} \int_0^\infty (O.P.C.C.) \sin 2\pi f\tau \, d\tau$$

(3.04)

The inverse relationships to define the I.P.C.C. and O.P.C.C. terms may be developed in terms of the co- and quad-spectral densities using standard formats. For the case of zero time shift, $\tau = 0$, the area under the curve of $\phi(x_1, x_2, f)$ vs. frequency is equivalent to the cross-correlation function and is given by:

$$\overline{\ell(x_1, t) \, \ell(x_2, t)} = \int_0^\infty \phi(x_1, x_2, f) df$$

(3.05)

When the spatial locations are identical, i.e., $x_1 = x_2$, the expressions become more familiar since they define the auto-correlation (A.C.) and the power spectral density $(\phi(x, f))$.

15

For $x_1 = x_2$,

$$A.C. = \frac{1}{2}\left[R.C.C. + F.C.C.\right]$$

$$\Phi(x_1, x_1, f) = \phi(x_1, f)$$

$$\Psi(x_1, x_1, f) = 0 \quad \text{since } R.C.C. = F.C.C.$$

It is pointed out by Press and Tukey (18) that the co-spectrum, $\Phi(x_1, x_2, f)$, and the quadrature spectrum, $\Psi(x_1, x_2, f)$, can be considered as representing the power of the in-phase and 90 degree out-of-phase components respectively of the two random signals (from an electrical sense). The in-phase power may be physically visualized as a result of Eq. 3.05, where it can be seen as corresponding to the cross-correlation function. The out-of-phase power appears less amenable to physical interpretation.

For convenience in data handling, the following normalizing procedures have been employed:

1. Auto-correlations were normalized with respect to A.C. at $\tau = 0$, and are denoted as the auto-correlation function, A.C.F.

2. The power spectral densities of the individual data channels and the corresponding co- and quad-spectral densities were normalized such that:

$$\int_0^{125} \phi_n df = \int_0^{125} \Phi_n df = \int_0^{125} \Psi_n df = 1.0 \tag{3.06}$$

The subscript "n" denotes normalized spectral densities.

3. Both in-phase and out-of-phase cross-correlations were normalized with respect to I. P. C. C. at $\tau = 0$, and the corresponding functions are denoted as I. P. C. C. F. and O. P. C. C. F. respectively.

Digital computer techniques as outlined in Appendix B were used to obtain finite length series approximations to the integral formulations. The estimates were obtained at intervals of time lag of 0. 004 seconds or frequency of 1 cycle per second. Because of the relatively close spacing of the estimates, the computed points are omitted on the correlation or spectral density curves. Figures 6 to 14 show the variations of the correlation or spectra curves versus time lag or frequency respectively for the case of both lift and drag at a typical tunnel operating condition (q = 40 psf) corresponding to a Reynolds number of 0. 75 x $10^6$, when the instrumentation packages were in an adjacent position (which corresponds to $X_2/_D = 4.86$ and $X_1/_D = 5.17$). The data are identified as to source by the channel nomenclature defined in Section II. Results from both data channels are shown in order to illustrate the data scatter inherent in these random signals.

The drag data show slightly more periodicity in the auto-correlation curves than does the lift data (Figures 6 and 11). The Fourier cosine transform of the auto-correlations (Figures 8 and 13) show a scattering of low frequency power peaks, but their frequencies are not well enough established in order to draw any firm conclusions regarding the drag or lift in the supercritical Reynolds number range. A feature exhibited by both the drag and lift power

distributions is that the dominant contributions to the power spectra occur at frequencies below 40 cps, which corresponds to a Strouhal number of approximately 0.15.

The cross-correlation functions of lift and drag loadings are significantly different (Figures 7 and 12). The out-of-phase cross-correlation for the lift case is quite small while in the case of drag loadings, a relatively large negative value occurs for small values of time shift ( $\tau$ less than 0.1 seconds) and thereafter are of the same magnitude with the out-of-phase term leading the in-phase term by about 0.05 seconds. The form of the cross-correlation functions as presented here is such that they give a measure of not only the average correlation function, but also of the difference between the rearward and forward cross-correlation. In the case of lift, the out-of-phase cross-correlation indicates that not much difference exists between the rearward and forward cross-correlations, which is in contrast to the drag case.

An alternate way of considering these characteristics is provided by the cross-spectral density curves (Figures 9, 10, and 14). In the lift loading case, the ratio of the out-of-phase to the in-phase power is +0.12. The in-phase power term is amenable to physical interpretation since it corresponds to the mean average cross-product of the two loading terms with zero time shift. The real and imaginary components of the cross-spectrum are shown vs. frequency by the co- and quad-spectrum curves respectively. It will be noted that since the out-of-phase power is an order of magnitude smaller than the in-phase power, the quad-spectral density curve has

both positive and negative values depending on the sign of the argument of the complex valued spectral density at a particular value of frequency. A negative value of co-spectral density corresponds to an 180 degree phase shift of the in-phase-power component relative to the predominant zero angle for in-phase power.

In the drag loading case under consideration, the out-of-phase power was found to be -1.24 times the in-phase power. The consequences of this relationship are shown on Figure 14, where it may be noted that the co- and quad-spectral density distributions are of the same order of magnitude and both terms are quite small for Strouhal numbers beyond 0.10.

Only a typical set of data are presented in this fashion. The presentation of all the data would be lengthy and questionable as to ease of interpretation. It is hoped in the future, to develop expressions for the correlations and the spectral densities in a manner such that the transform relationships between the time and frequency domains are compatible. In this manner, the statistical data would be represented by general polynomial relationships, and a family of curves would show the dependence of the various coefficients upon significant physical parameters such as spatial location and tunnel operating condition.

A typical situation suitable for evaluation by a curve fitting operation is shown on Figure 15, where the various curves apply to identical situations obtained from four different data runs. As can be noted, the power spectra curves show the most scatter for estimates made below a frequency of 10 cps. This suggests that in

19

order to get a better estimate of the low frequency end of the curves, the amount of data sampling should be increased by either increasing the time duration of a single record or by averaging over an ensemble. The limit on the sampling time for a single record is established by the size of the digital computer memory storage and the machine time required to execute a program that uses a long set of input data. It is felt that averaging among the various members of the ensemble will provide satisfactory results from the standpoint of defining the low frequency end of the spectral density curves to a reasonably high degree of probability.

Figure 16 shows the effects observed on the power spectra as the axial location of the load station was varied from 2.9 to 1.9 diameters from the tip. Although the RMS level of unsteady lift does not show any noticable changes, the power spectral density curve shows an increase in value near a frequency of 85 cps (Strouhal number, $S = 0.32$) for the load station that was 1.9 diameters from the tip. This trend was not observed for axial locations of the load instrumentation more distant from the tip. When the load station was one diameter from the tip, a trait similar to that of Figure 16 was observed. Future work is contemplated to study the inter- ference effects due to proximity to the tip for several different tip shapes.

3.3.   Axial Correlation:

A significant measure of the spatial variation of a random function is provided by a cross-correlation coefficient. This concept

is directly applicable to the results reported here since these are essentially measurements of local load and may be considered as acting at a point along the cylinder axial coordinate. The cross-correlation function generally requires the specification of two points in space and a time shift (or lag), $\tau$. When the two points coalesce into a single point, the cross-correlation function becomes the more familiar auto-correlation function. For the particular application considered in this section, the cross-correlation function will be restricted to a zero value of time shift and will be normalized with respect to the square root of the product of the corresponding variances.

If the two field measurements are denoted as:

$$\ell_1 = \ell_1(t) + \overline{\ell}_1$$

$$\ell_2 = \ell_2(t) + \overline{\ell}_2 \tag{3.07}$$

Then the cross-correlation coefficient is defined by:

$$R = \frac{\overline{\ell_1 \ell_2} + \overline{\ell}_1 \, \overline{\ell}_2}{\left[ \overline{\ell_1^2} + (\overline{\ell}_1)^2 \right]^{1/2} \left[ \overline{\ell_2^2} + (\overline{\ell}_2)^2 \right]^{1/2}} \tag{3.08}$$

where

$\overline{\ell_1 \ell_2}$ = mean average product of $\ell_1$ and $\ell_2$ with zero time shift,

$\overline{\ell}_1$ or $\overline{\ell}_2$ = mean average values of $\ell_1$ or $\ell_2$.

A further simplification for the definition of cross-correlation coefficient, R, is provided by the assumption that the mean average values of $\ell_1$ and $\ell_2$ are zero. This is in accord with both the analog and digital results to be presented subsequently. Therefore, when $\overline{\ell_1}$ and $\overline{\ell_2}$ = 0, R becomes:

$$R = \frac{\overline{\ell_1 \ell_2}}{\left[\overline{\ell_1^2} \cdot \overline{\ell_2^2}\right]^{1/2}} \tag{3.09}$$

It follows from the Schwarz inequality that the cross-correlation coefficient cannot exceed a magnitude of 1.0. Also, R is + 1.0 when the two measuring stations are identical, and both plus and minus values of R are admissible.

The load stations measured either lateral (lift) or drag forces depending upon their orientation with respect to the free stream wind vector. The two stations were denoted as either channel 1 or 2. The channel 1 station was variable in its axial location above the channel 2 station which was fixed at a position 4.86 diameters above the floor. A sketch showing the axial orientations of the load stations on the 8.07 diameter long cantilever cylinder model is presented in Section II on Figure 3. For sake of convenience, subscript notation is used when presenting cross-correlation coefficient results using the subscripts " $\ell^2$ " and "$d^2$" to indicate lift-lift or drag-drag orientation of the load stations respectively.

Figures 17 and 18 show the variation of the correlation coefficients $R_{\ell^2}$ and $R_{d^2}$ with respect to the axial spacing

22

between the two measuring stations for four values of Reynolds number in the supercritical range ($0.38 \times 10^6 < R < 0.75 \times 10^6$). The closest spacing for which data points are presented is $\frac{\Delta X}{D} = 0.316$, which corresponds to the instrumentation sections being in an adjacent position. The points shown as a ( $\odot$ ) were obtained using analog computer techniques in conjunction with tape data playback. Comparison is made with values of correlation coefficient obtained by digital means ( $\triangle$ ), and as can be noted, the two methods give results which are in reasonable accord. The data points shown by the symbols ( $\square$ ) and ( $\nabla$ ) refer to investigations made of flow interference effects, and will be discussed in Section 3.4.

In general, the cross-correlation coefficient for lift force shows a smooth decrease from 1.0 to 0 as the spacing variable, $\Delta X / D$, is increased from 0 to beyond 2.0. It will be noted that in the Reynolds number range investigated, $R_{\ell^2}$ is less than 0.20 for spacings beyond one cylinder diameter. The correlation coefficients for unsteady drag, shown on Figure 18, initially decrease in value more rapidly than noted for $R_{\ell^2}$ and cross to a negative value when $\Delta X / D$ is somewhere between 0.5 and 0.6. A peak negative value of $R_{d^2}$ is attained before $\Delta X / D$ reaches 1.0, then it asymptotically increases again to zero as $\Delta X / D$ becomes large. The asymptotic approach of the correlation coefficients to zero demonstrates that the instrumentation was not appreciably influenced by either inertia loading or bending mode effects of the cylinder model.

A measure of the spatial correlation is given by the correlation length, $\chi_{(\ )}$ which is defined as the area under the curve of cross-correlation coefficient vs. axial spacing distance. The correlation length is normalized for ease in handling with respect to the cylinder diameter, D. The governing equation is:

$$\chi_{(\ )}(X_2) = \int_0^{\infty} R_{(\ )}(X_2, \Delta X)d\left[ \frac{\Delta X}{D} \right] \tag{3.10}$$

where $\Delta X = X_1 - X_2$

$X_1$ = axial coordinate of relocable station

$X_2$ = axial coordinate of reference station.

The upper limit of integration actually used in evaluating $\chi_{\ell 2}$ and $\chi_d 2$ was 2.4 because the cross-correlation coefficients, $R_{\ell 2}$ and $R_d 2$, became quite small beyond a two diameter axial spacing from the $X_2 = 4.86$ D reference position.

The correlation lengths, obtained by integrating the curves of Figures 17 and 18, are summarized on Figure 19 as a function of Reynolds number. The correlation length for lift, $\chi_{\ell 2}$ , is approximately 0.5 cylinder diameters while the corresponding length for the unsteady drag term is heavily influenced by the negative values of $R_d 2$ and consequently is considerably less although still positive. Actually the correlation length loses its significance in the case of the unsteady drag term in a manner analogous to the situation posed by an axially traveling periodic wave. Since the unsteady lift terms are heavily influenced by the unsteady pressures in in the $\theta = 90^\circ$ region of the circular cylinder while the unsteady

drag is dominated by unsteady pressures in the wake, one could associate the $\chi_{\ell^2}$ term with the significant length scale for vortex shedding, and the $\chi_{d^2}$ term with a length scale in the wake region.

Literature with regard to correlation lengths of unsteady flow variables near to or on the cylinder surface are quite limited, and no values are known to the author with regard to the total loading terms. In Reference 19, el Baroudi presents measurements of local flow velocity just out of the boundary layer at the $\theta = 90°$ position using a pair of hot wires in the Reynolds number range of 11,000 to 45,000. He obtained correlation coefficients and lengths using a sum and difference technique with respect to the mean square of the voltage signals. The correlation lengths obtained by el Baroudi varied between 3 and 6 diameters, which is slightly higher than the measurements made by Prendergast (20), using a pair of static pressure orifices at the $\theta = 90°$ and $180°$ positions. Prendergast, though, covered a higher Reynolds number range ($2.5 \times 10^4 < R < 1.25 \times 10^5$). Prendergast's results were of noteworthy interest since they showed that the unsteady pressures at the $\theta = 180°$ position had a considerably smaller correlation length than those at the $\theta = 90°$ position, and that both correlation length measurements became less than unity as the transitional Reynolds number was approached. Humphreys (21) mentioned a significant length term of 1.56 diameters when discussing the laminar-turbulent separation cells that were observed by means of thread tufts at a Reynolds number of about $1 \times 10^5$. The results of el Baroudi, Prendergast, and Humphreys in the subcritical range are shown on Figure 19 for

purposes of making an illustrative comparison with the results
obtained from direct load measurements in the supercritical
Reynolds number range.

Roshko (22) in 1954 reported on the development of turbulent
wakes in the subcritical range for $40 < R < 10^4$. He found that in
the stable subrange $(40 < R < 150)$, the vortex street had a periodic
spanwise structure and the periodic fluctuations in the wake were
perfectly correlated at distances up to a 100 cylinder diameters apart
in the spanwise direction although the signals (as provided by the two
hot wires) were not in phase. At $R = 80$, the wave length in the wake
parallel to the cylinder was noted as being about 18 diameters. In the
irregular subrange $(300 < R < 10^4+)$ at a Reynolds number of 500,
there was a good correlation in the wake only when the two hot wires
were spaced a few cylinder diameters apart. The wake measurements
by Roshko were qualitative in nature from the standpoint of determining
a correlation length in the irregular subrange, but nevertheless, his
results do support the observations made at a later date by el Baroudi
and Prendergast in the immediate vicinity of the cylinder when the
flow corresponds to the irregular region of the subcritical Reynolds
number range.

## 3.4 Surface Effects:

A study of wind tunnel solid and wake blockage interferences
by E. Pounder and the author (23) in 1950 disclosed that the flow
about a circular cylinder in the supercritical Reynolds number range
$(R = 1 \times 10^6)$ was sensitive to surface disturbances. It was found

that fingerprints accidentally left overnight on the forward portion of a steel cylinder model produced sufficient corrosion to distort the wake total head pattern by increasing the local width downstream of the corrosion mark. Polishing of the model removed the disturbance and its effects. In order to obtain a two-dimensional wake pattern, it was necessary to establish a uniform spanwise flow separation by means of wire separation strips attached to the model.

Consistent with the observations of reference 23, the effects of flow sensitivity to surface condition were noted in both the RMS and the steady state values of lift. It was possible to induce steady state values of section lift coefficient of approximately 0.30 magnitude by properly placing* a clay particle near to the instrumentation section on the forward portion of the model. The zone of influence of a surface disturbance was examined in a cursory manner by placing a double thickness of 0.50 inch wide masking tape in a circumferential direction on the model. The result, reported by the author (24) indicated that the disturbance was not felt beyond one cylinder diameter in the axial direction.

In order to explore further the sensitivity of the flow characteristics to surface irregularities, two types of controlled disturbances were introduced as model configuration changes. These disturbances corresponded to a.), localized boundary layer tripping by means of radial air blowing through small orifices on the model surface, and

---

*  The sign of the lift term depended upon which side of the model that the clay speck was placed. Upward lift occurred when the disturbance was on the lower side of the model.

b. ), a narrow chordwise gap produced by inserting a narrow shim between the model spacer sections.

Two 0. 020 inch diameter orifices were installed in one of the spacer sections at the $\theta = \pm 30^{\circ}$ positions (angular coordinate for cylinder measured relative to forward stagnation point) and were connected in parallel to a Fischer and Porter flow meter so that the air flow could be measured for combined or individual blowing in a radial direction from the model surface. No effect was perceptible at a tunnel dynamic pressure of 10 psf (Reynolds number = 0. 38 x $10^{6}$) through the complete range of orifice flow velocity ratios[*]. At the higher test Reynolds numbers (0. 53 x $10^{6} <$ R $<$ 0. 75 x $10^{6}$), a pronounced effect was noted upon both the RMS and mean average values. A summary of the peak values due to radial blowing from the orifices is presented on Figure 20 for both lift and drag as a function of axial distance from the disturbance. It will be noted that from the standpoint of peak values, drag is not as sensitive as lift to orifice flow, the lift extrapolates at zero axial distance from the disturbance to almost a fourfold increase in the RMS value in addition to a steady state lift coefficient value of 0. 4, and the perturbed flow region is not felt beyond one diameter in the spanwise direction.

Figures 21 and 22 show the dependence of sectional load data upon the orifice velocity ratio for a tunnel dynamic pressure of 20 psf. Similar results were noted at the other two tunnel operating points of 30 and 40 psf. The effects of orifice air flow did not become noticable until the orifice velocity ratio corresponded to approximately 0. 3, and

---

[*] Orifice flow velocity ratio = $V_{orifice} / V_{free\ stream}$

once instigated, the effects occurred very rapidly, followed by a gradual subsidence as orifice flow was increased. The details differed for the other Reynolds numbers, but the general characteristics were the same.

The actual orifice velocity required for disturbing the flow was observed in still air in order to get a feel for the magnitude of the disturbance. It was found easier to detect the airflow from the orifice using ones' eyelid rather than a finger, which serves to illustrate that the disturbance was slight.

The steady state lift value could be induced in either direction depending on the individual side used for blowing, with the general feature that blowing from one side produced a lateral force acting in the opposite direction. Combined blowing from both orifices did not exhibit symmetry from the standpoint of producing no net change in steady state lift, which fact may be attributed to difficulties inherent in blowing through two orifices using a parallel piping arrangement. The peak values of incremental changes in steady state lift and drag were used to determine a resultant force due to blowing from one side only. The resultant force coefficient, which has a magnitude of approximately 0.4, can be considered as acting at the $\theta = 98^{\circ}$ position.

The normalized power spectrum curves are presented vs. frequency, f, on Figures 23, 24, and 25 for the case of the lateral force at two Reynolds numbers, and for the drag force in order to show the effects of orifice blowing upon the power distribution of unsteady load. One must remember that the curves are normalized

such that the area represents unity, even though the mean square of unsteady load differs by a large factor. With this point established, the effects of orifice blowing upon lift is to produce a significant increase in the power distribution in the range of Strouhal number (fD/V) from 0.05 to 0.18 for both Reynolds number conditions presented. The unsteady drag shows an increase in power for Strouhal numbers beyond 0.05, but leaves the low frequency end of the power spectrum relatively unaffected, and is a distributed type disturbance over the frequency range shown.

The correlation coefficients for lift, as seen on Figure 17, show a well defined rise in correlation between two load stations approximately one cylinder diameter apart, although the disturbance is near to one load measuring package. This may be explained by the fact that the change observed in the power spectrum of the load station nearest to the disturbance is also felt by the more distant load measuring station. Although not presented, a curve of the co-spectral density, the area of which is a measure of the cross-correlation of the two random signals, shows an increase in power distribution over the same frequency range as observed on the power spectrum curves.

Figures 26 and 27 show the effects of a chordwise gap upon the unsteady lift, how the disturbance dies out within a one cylinder diameter distance in a spanwise direction, and the changes produced in the lift power spectral density. In general, the effects are not as severe as those produced by orifice blowing. The power spectrum curve shows a slight rise in power content in the same Strouhal

number range as observed for the case of orifice blowing. The gap was produced using a 0.025 inch thick aluminum shim following an earlier test using a 0.010 inch thick shim without any effects. The use of a gap vented to a common large cavity that is interior to a model can intuitively be expected to produce interference effects considerably larger than those shown on these figures.

## 3.5   Structural Response:

Brief consideration has been given to the structural response of the cantilevered circular cylinder model when exposed to unsteady air loads developed by wind tunnel air flow. The reasons were to understand the structural configuration better, to relate the motion of the model to air loads, and to try to detect the existence of an aeroelastic coupling in the unsteady air loads. Accelerometers were attached internal to the model and the output signals were recorded on magnetic tape, observed on an oscilloscope, and quantitatively measured for RMS values.

The model accelerations are presented on Figures 28 and 29 for the lateral and longitudinal directions respectively as a function of tunnel dynamic pressure. Data for the lateral response were obtained with the lead shot damper package both on and off. The trends are clear in that the RMS value of tip acceleration smoothly increased with tunnel air speed and did not exhibit any form of resonant peaks. This is consistent with the fact that the model was exposed to a random type air loading and its response was primarily dictated by the structure acting as a narrow band-pass filter.

The data on Figures 28 and 29 were obtained by analog means using a 9 second time constant in a time averaging circuit during tape data playback. The values are in accord with those measured during the test on an RMS meter. The analog data playback provided a time history of the acceleration response. It was noted that occasional bursts of increased acceleration would appear and these are indicated on Figures 28 and 29 by the dashed fairing. These sudden bursts produced approximately a 10 per cent increase in the RMS values.

The effects of the lead shot damper section at the top of the model were evident by both a slight lowering of the model's fundamental response frequencies and by approximately a 50 per cent decrease in the RMS value of acceleration response.

It is interesting to note that the lateral and longitudinal accelerations are only slightly different. One frequently thinks that the response of a cylindrical structure to fluctuating air loads should be greater in a lateral than a longitudinal direction, but of course this distinction applies only if the corresponding forcing functions also exhibit significant differences. An example of a flow region where the accelerations might occur in different levels of magnitude would be when the Reynolds number (based on cylinder diameter) is subcritical, for in this case the unsteady loads, e. g. , Keefe (9), are an order of magnitude apart.

Oscilloscope observations show the acceleration response as a randomly modulated wave with a well defined frequency. Estimates of power spectral density substantiate this visual

observation. Normalized power spectral density curves are presented on Figures 30 and 31 for the lateral accelerations with and without the tip damper package present at two values of tunnel dynamic pressure. The basic model responds laterally with approximately a 12.5 cps fundamental frequency. A few of the higher vibration frequencies occur at 21, 25, and 32 cps. Although the spectral densities were estimated by digital means to 100 cps in 1 cps steps, no significant energies appeared at the higher frequencies. The lead shot damper package on the tip lowered the fundamental frequency to 11.5 cps which effect can be attributed to the influence of a concentrated mass. When the dynamic pressures were at and below 30 psf, the only significant power concentration was at the fundamental as evident on both the tip and lower accelerometers. At a dynamic pressure of 40 psf, the tip accelerometer showed a slight response at 24, 31.5, and 43.5 cps. The lower accelerometer appears to have been close to a nodal point for the 24 and 31.5 cps frequency terms; however, such is not the case for the 43.5 cps value since a distinct term shows in addition to another contribution at approximately 49 cps.

An estimate of the structural damping for the model structure in the fundamental vibration mode was made for the model with and without the damping package by observing the decay of a suddenly induced vibration. The data were recorded on magnetic tape and playback was made onto an Offner Type P recording oscillograph. An average value of damping ratio (fraction of critical) of 0.014 was obtained and the presence of the damping package was not notable other than the influence on frequency. The fundamental response

frequency for the basic model's lateral acceleration was in accord
with the power spectral density result (12. 5 cps), but when the
damping package was present, the fundamental frequency was 10. 4
cps as compared to the power spectrum result of 11. 5 cps. A clue
relating to the latter discrepancy is provided by the fact that the
lead shot did not alter the model damping ratio during vibration decay
measurements, and hence the lowering of the fundamental frequency
was due to the total mass of the lead shot. Apparently when the lead
shot contributes to model damping, only a fraction of the mass of the
lead shot can be considered as acting to change the vibration
frequencies.

Other measurements of the model frequency response (with
damper installed) using a prototype shaker model on the tip disclosed
an approximate value of damping ratio in the lateral direction of
0. 04 (based on 1/2, 1/4, and 1/9 power point observations for the
displacement response curve near the fundamental vibration mode)
when the tip lateral acceleration had an RMS value of approximately
0. 21 "g's", a value about 3 times greater than those observed on the
model when operating at a dynamic pressure of 40 psf. The 0. 04
value for damping ratio must be considered as an equivalent value
since the lead shot would provide localized rather than distributed
damping. It is suspected that during the decaying oscillation meas-
urements, the excitation of the structure was not sufficient to
produce damping by the movement of the lead shot. Therefore, the
action of the lead shot should be considered as a type of non-linear
localized damping.

## SECTION IV

## CONCLUDING REMARKS

The flow of air about a circular cylinder results in both steady and unsteady air loads. The investigations reported here relate to local load measurements obtained in the GALCIT Ten-Foot Wind Tunnel in a Reynolds number range (based upon cylinder diameter) of $0.38$ x $10^6 < R < 0.75$ x $10^6$, which is classified as being in the super-critical flow region.

It was found that the unsteady lift depends to a large extent on surface conditions. The RMS values of unsteady lift and drag force coefficients were observed to be of the same order of magnitude and to have a value of about $0.04$ in the flow region under investigation using polished aluminum models. This new value of unsteady lift coefficient is lower than that obtained by Fung (10), presumably because his model differed in details of model configuration and sur-face condition (refer to Section 3.1 for discussion). The values of unsteady lift presented by Keefe (9) in the subcritical Reynolds number range, are an order of magnitude higher and show a random modulation of amplitude at a frequency corresponding to a Strouhal number, $S = 0.20$. The lack of a dominant frequency in the results reported here in addition to the differences in RMS level of unsteady load may be attributed to differences in the details of vortex layer shedding between the subcritical and supercritical flow regions.

The spanwise correlation lengths for unsteady lift were found to be approximately a half a cylinder diameter which is in contrast to

limited information in the subcritical range. Similar type data in the subcritical range by el Baroudi (19) and Prendergast (20) indicate that it would be 3 to 4 diameters in extent. The measurements of the latter author do show a decrease in correlation length as the transitional Reynolds number is approached.

Controlled localized surface disturbances were generated by radial blowing of air through small orifices in the forward portion of the model. By this technique it was possible to produce over a three fold increase in the RMS level of unsteady lift. Asymmetric blowing resulted in the development of steady lift. The power spectrum of the load measuring station adjacent to the blowing orifice showed that when the tripping phenomena was taking place, a large portion of the power increase occurred in a range of Strouhal numbers from 0.05 to 0.18 in addition to the development of marked peaks. The axial correlation between a load station adjacent to the blowing orifice and one about 0.8 diameters distant disclosed that the tripping phenomena resulted in a significant increase in the degree of cross-correlation.

If one assumes that the tripping action due to a surface disturbance corresponds to an effective increase in Reynolds number, then the results tend to support the conjecture that in a higher Reynolds number region (say for $R > 3 \times 10^6$), the unsteady lift loads would increase in value, signs of periodicity would appear in the power spectral density curves, and the axial correlation lengths would increase.

The studies of surface disturbances also may be interpreted as supporting the inference by Roshko (7) regarding the existence of

separation bubbles ahead of the normally accepted location of the flow separation point in the supercritical Reynolds number range. A trait of the subcritical range is that a fairly well defined laminar separation point appears forward of the maximum thickness in conjunction with the occurrence of boundary layer transition in the free shear layer. In contrast, the high supercritical range (denoted as transcritical by Roshko when $R > 3.5 \times 10^6$) is characterized by the turbulent separation point being aft of the maximum thickness and the boundary layer transition occurring on the model, presumably well forward of the maximum thickness ($\theta = 90^\circ$). If the boundary layer transition point is sufficiently forward on the model, the separation point becomes fairly well defined, but when the transition takes place near to the $\theta = 90^\circ$ point on the cylinder, conjecture is that a general instability occurs in the flow with a subsequent random development of separation bubbles and a poorly defined flow separation point. Although a physical model is desired to explain the phenomena of a decrease in both the RMS value and the cross-correlation of the unsteady lift load in a particular Reynolds number range, the available evidence is not sufficient at this time to make a well substantiated proposal.

The accelerometer measurements on the model confirmed the narrow band-pass filter action of the structure to random excitation. Unfortunately, the results were not suitable to confirm the effects of damping on response magnitude since supplemental damping was introduced in a concentrated rather than a distributed manner, although the changes in system damping could be estimated on an equivalent basis.

The power spectrum results for section loading were not sufficiently consistent in order to show the existence of an aeroelastic feedback term in the generation of unsteady loads in the range of Reynolds numbers tested. The two levels of model vibration, made possible by changes in model damping, did not show any changes in RMS level of unsteady lift loads. Because of the characteristics of the flow separation in the supercritical flow region, one is not justified in drawing conclusions applicable with regard to high Reynolds number regions (for $R > 1 \times 10^6$) concerning the subject of aeroelastic coupling.

Measuring techniques that indicate local aerodynamic properties make possible many test programs to study cylinder flow characteristics. These studies are necessary before a physical model can be proposed to explain the many factors influencing the three dimensional flow separation problem. Typical studies which might be considered are:

1. Investigate the effects of tip shape or end conditions upon local loadings and spanwise correlations. A program is currently in progress by H. S. Blackiston, Jr. using the same equipment as described in Section II and Appendix A to evaluate these influences and results should be available in the near future.

2. Revise the instrumentation to record single pressure readings at two stations in order to better define the random nature of the pressure field. One could use an existing end-plate model (presently available in the

38

laboratory) in order to coordinate the measurements with hot-wire readings. The effects of controlled surface disturbances could be studied in detail using these techniques.

3. Extend the methods used in the supercritical range to other areas of interest, in particular for the case of Reynolds numbers greater than $3.5 \times 10^6$. This would require access to a different test facility, but the results would be applicable in an engineering sense to current problems of interest on large cylindrical structures. If a variable density wind tunnel facility were available, changes in the thickness of the pressure transducer membrane would allow the use of a single test model for a Reynolds number starting at the sub-critical, through transition into the "early" super-critical $(0.3 \times 10^6 < R < 3 \times 10^6)$ and finally into the high supercritical (transcritical) range.

It is possible that a systematic and well coordinated group of tests could do much to increase the understanding of a fundamental problem in basic fluid mechanics, namely the generation of unsteady loads on a circular cylinder.

39

REFERENCES

1. Strouhal, V., "Uber eine besondere Art der Tonerregung", Wied. Ann. Physik u. Chem., Neue Folge, Band V, pp. 216-251 (1878).

2. Strutt, J. W., Lord Rayleigh, "Theory of Sound", Vol. II, Dover Publications, pp. 412-414 (1945).

3. von Karman, Th., and Rubach, H., "Uber den Mechanismus des Flussigkeits-und Luftwiderstandes", Physikalische Zeitschrift, Band 13, Heft 2, pp. 49-59 (January 1912).

4. Goldstein, S., "Modern Developments in Fluid Mechanics", Oxford University Press (1938).

5. Rosenhead, L., "Vortex Systems in Wakes", Advances in Applied Mechanics, Academic Press, Vol. 3, pp. 185-195 (1953).

6. Humphreys, J. S., "On a Circular Cylinder in a Steady Wind", Ph.D. Thesis, Harvard University (1959).

7. Roshko, A., "Experiments on the Flow Past a Circular Cylinder at Very High Reynolds Number", Journal of Fluid Mechanics, Vol. 10, Part 3, pp. 345-356 (1961).

8. Macovsky, M. S., "Vortex Induced Vibration Studies", David Taylor Model Basin Report 1190 (1958).

9. Keefe, R. T., "An Investigation of the Fluctuating Forces Acting on a Stationary Circular Cylinder in a Subsonic Stream and of the Associated Sound Field", University of Toronto, UTIA Report 76 (1961).

10. Fung, Y. C., "Fluctuating Lift and Drag Acting on a Cylinder in a Flow at Supercritical Reynolds Numbers", Technical Report EM 8-5, Space Technology Laboratories, Inc. (May 1958), Also published in the Journal of the Aerospace Sciences, Vol. 27, No. 11, pp. 801-814 (1960).

11. Ozker, N. S. and Smith, J. O., "Factors Influencing the Dynamic Behavior of Tall Stacks Under the Action of Wind", Trans. A.S.M.E., Vol. 78, pp. 1381-1391 (1956).

12. Fujino, T., Takahei, T., Nakagawa, K., and Arita, Y., "The Dynamic Behavior of Tall Stacks and the Action of Wind", Proceedings of the 7th Japan National Congress for Applied Mechanics, pp. 387-392 (1957).

13. Ezra, A. A. and Birnbaum, S., "Design Criteria for Space Vehicles to Resist Wind Induced Oscillations", American Rocket Society Paper No. 1081-60 (April 1960).

14. Fung, Y. C., "The Analysis of Wind-Induced Oscillations of Large and Tall Cylindrical Structures", Technical Report EM 10-3, Space Technology Laboratories, Inc. (June 1960).

15. Fung, Y. C., "The Theory of Aeroelasticity", John Wiley and Sons, Inc. (1955).

16. Tsien, H. S., "Engineering Cybernetics", McGraw Hill Book Co., Inc. (1954).

17. James, H. M., Nichols, N. B., Phillips, R. S., "Theory of Servomechanisms", McGraw Hill Book Co., Inc. (1947).

18. Press, H. and Tukey, J. W., "Power Spectral Methods of Analysis and Their Application to Problems in Airplane Dynamics", AGARD Flight Test Manual, Vol. IV, Part IV-C (1957).

19. el Baroudi, M. Y., "Measurement of Two-Point Correlations of Velocity near a Circular Cylinder Shedding a Karman Vortex Street", University of Toronto, UTIA TN 31 (1960).

20. Prendergast, V., "Measurement of Two-Point Correlations of the Surface Pressure on a Circular Cylinder", University of Toronto, UTIA TN 23 (1958).

21. Humphreys, J. S., "On a Circular Cylinder in a Steady Wind at Transition Reynolds Numbers", Journal of Fluid Mechanics, Vol. 9, pp. 603-613 (1958).

22. Roshko, A., "On the Development of Turbulent Wakes from Vortex Streets", NACA TR 1191 (1954).

23. Pounder, E. and Schmidt, L. V., "Investigation of Blockage Effects from Flow about Circular Cylinders in a Two-Dimensional Wind Tunnel", Engineering Degree Thesis, California Institute of Technology (1950).

24. Schmidt, L. V., "Oscillating Air Loads on Circular Cylinders", Minta Martin Student Award Paper, Institute of the Aerospace Sciences, pp. 229-239 (1962).

25. McCracken, D. D., "A Guide to FORTRAN Programming", John Wiley and Sons, Inc. (1962).

## APPENDIX A

## EQUIPMENT

A. 1  Model Description:

A cantilevered cylinder model was designed for installation in the GALCIT Ten-Foot Wind Tunnel. A schematic side view of the installation is shown on Figure 1. The model was isolated from the tunnel test section structure and was supported by a large steel tank structure that was 4 feet in diameter, 7 feet in length, and fabricated from 3/16 inch thick steel boiler plate. The bottom of the tank was enclosed by 1/4 inch thick plate while the top of the tank was provided with a standard 48 inch x 3/16 inch dished head which in a side view appears to be elliptical with a 12 inch depth. A 2 inch thick x 9 inch diameter steel cap was welded into the dished head in order to provide a base for attaching the model sting support.

The steel tank, which was below the test section, was bolted onto a 10 inch steel channel framework which was in turn bolted to building structure. This method of installation was necessary since the tunnel structure did not have sufficient stiffness to adequately support a cantilevered cylinder model, especially since fluctuating loads were expected which could induce unwanted model vibrations.

The model, as shown in the photograph of Figure 2, was constructed of 8. 5 inch diameter aluminum pipe and was a little over 5 feet in exposed length. The use of finely machined spacer sections made possible the location of the instrumentation sections in almost any spanwise position on the model since they were made up in increments of length of 0. 1 cylinder diameter. A cap section at the

top of the model acted as a terminal for a 3/4 inch diameter steel tie rod which kept the complete assembly locked to the steel model sting support which in turn was seated on a shoulder on top of the steel tank.

The two instrumentation packages were 0.316 cylinder diameters in length, hence establishing the closest spacing of the orifices for cross-correlation measurements. The receptacles for the pressure transducers were provided inside the basic instrumentation sleeve by a pattern casting technique using an epoxy base aluminum petty (DEVCON Type F-2). After the casting operation, the 0.025 inch diameter orifices were drilled, and 1/8 inch thick plexiglas spacer sections glued into the recesses. An aluminum shielding case enclosed each group of nine pressure transducers. The analog summing circuit board, the trimming capacitor, and the common pressure manifold were in the interior of each shielded compartment. A cross-section of the transducer installation is shown on Figure A.1.

The flat floor, which can be seen in Figure 2, was constructed of plywood and had as a purpose the establishment of smooth flow at the cylinder-wall intersection. A boundary layer survey disclosed a displacement thickness of approximately 0.3 inches at the model installation station. The slight gap at the wall cutout, through which the cylinder model extended, was sealed with tape in order to preclude spanwise airflow at the cylinder wall intersection.

The four pressure manifolds which were connected to each group of nine pressure pickups, provided a way for calibrating the

transducers during the course of testing. Each section was calibrated with regard to both the sensitivity of the individual sectors and the matching of the sectors so that a proper load summation occurred. During the testing, the back of the diaphragms were vented to a suction pressure corresponding to a pressure coefficient of approximately $C_p$ = -0.8. This was attained by connecting the pressure manifolds to a static pressure source in the tunnel. It was necessary to vent to a constant pressure coefficient source in order to assure that the pressure transducers did not exceed their design operating pressure limit. The static pressure reference was provided by a suitably oriented static pressure orifice on a 2 inch diameter by 7.6 inch long brass circular cylinder projecting from the North tunnel wall at the ninety degree tee-slot position approximately 32 inches ahead of the atmospheric vent.

Before the cylinder model was installed, a flow inclination check was made in the wind tunnel after the flat floor had been installed. The flat floor introduced some tunnel air-flow curvature, but by installing a ceiling deflector vane, the air flow was observed to be inclined less than a degree from the horizontal for the full span of the model. The flow inclination mentioned above corresponds to a spanwise flow component along the vertically mounted cylinder.

The physical character of the wind tunnel precludes a complete elimination of foreign particles in the air stream. It became apparent, that even though care was used to maintain cleanliness, the model surface was becoming eroded and contaminated by dirt impingement. A filter was introduced into the tunnel circuit for

the purpose of reducing the dirt problem. The filter consisted of a

6 foot wide patch of cheesecloth backed with one inch mesh chicken

wire fastened to the settling section turning vanes from the floor to

ceiling. An oil film was applied to the cheesecloth using kerosene.

The filter performed quite adequately and almost eliminated the

problem of dirt particles striking the model. After the cheesecloth

filter was installed, the operating range of tunnel dynamic pressure

did not exceed 40 psf in order to avoid failure of the cloth due to

fraying.

Standard flow velocity calibrations were performed using a

Prandtl type pitot-static tube and subsequently the tunnel was

operated with the model present using a simple estimate (two per

cent correction) of the solid blocking corrections. An estimate of

the true air speed and flow Reynolds number as a function of tunnel

dynamic pressure is shown on Figure A. 2.

During the initial model testing, two Statham accelerometers

were installed inside the model near to the tip and were oriented to

react to longitudinal (parallel to tunnel centerline) and lateral

accelerations. A limited amount of accelerometer output data was

monitored on an Offner Type P two channel recording oscillograph.

The traces were observed to contain a dominant frequency component

with the amplitude being modulated in a random manner. The varia-

tion of acceleration amplitudes (one half of peak to peak) are shown

on Figure A. 3 as a function of tunnel dynamic pressure. From the

standpoint of peak values, the lateral accelerations were observed

in all cases to be greater than the corresponding longitudinal accelera-

tions, and reached a maximum amplitude of 50 ft/sec$^2$ at a dynamic

pressure of 68 psf. Provisions were made to include the acceler-
ometer data onto the tape recorder, which fact allowed a greater
degree of flexibility in data handling. These results are discussed in
the main body of this report (Section 3. 5) where the measurements
can be interpreted in a quantitative manner.

Since the effects of model motion upon the pressure distribu-
tions were not known, a damper package was fabricated and installed
at the tip of the model. The damper package consisted of 5 compart-
ments which contained a total of 27. 5 pounds of lead shot and 25 cubic
inches of fine white sand, with the damping material occupying
approximately eighty per cent of the compartmented volume thereby
allowing internal particle movement. The effect of the damper
package is evident on Figure A. 3, where it can be seen that the peak
values of acceleration were reduced to a level about one-third of that
observed on the basic model. Attempts to further reduce the vibra-
tion levels were not undertaken. In addition to lowering the vibration
level, the damper package also lowered the fundamental frequency
due to the influence of the concentrated mass.

A calculation using simple beam theory showed that a cylinder
model (of similar physical properties) cantilevered from a rigid
foundation would have a fundamental frequency of 98 cps. The
observed fundamental frequency of approximately 11 cps was consid-
erably lower than that of an idealized physical model, and this
difference may be attributed to the elastic nature of the support tank
structure and the channel beam attachment to building structure.
The support structure was stiffer in the longitudinal than the lateral

direction and hence a slight difference occurred between the observed frequencies of the fundamental lateral and longitudinal vibration modes.

A. 2    Pressure Transducers

A description is presented in this section of the pressure transducer equipment that was developed and built in the GALCIT laboratory. The transducer consisted of a small coil placed behind a conducting, non-magnetic membrane (silver plated brass foil). Motion of the membrane due to the acting pressure differential was sensed by the adjacent coil as an effective change in the coil inductance value. The eddy currents developed in the membrane from the presence of the coil's magnetic field may be considered as acting to short out turns of the coil. A 100 KC carrier system, an outgrowth of a previously developed system at the GALCIT laboratory, was adapted to the transducer system. Sensitivities on the order of a 1000 volts/inch were obtained when the air gap between the coil and metallic surface was varied $\pm$ 0. 002 inches about the 0. 006 inch air gap position. When the coil was used in conjunction with the chosen membrane, sensitivities in excess of 1. 50 volts/psi were consistently obtained for the $\pm$ 0. 75 psi range.

The universal wound coil was fabricated using a George Stevens, Model 225 coil winder. The geometry was as follows: 130 turns of nylon wrapped No. 38 (A. S. W. G.)[*] copper wire with a coil width of 0. 062 inches and wound on an 0. 105 inch diameter mandrel. The coil, which was self supporting, was placed into a small ferrite cup core in

[*] American Standard Wire Gage.

order to confine the coil's magnetic field to a localized region for purposes of developing high sensitivity to air-gap change. A General Ceramics Model CF-201(T-1) cup core was used for this purpose.

The cup core and coil were in turn mounted on the tip of a brass rod which was inserted into the brass membrane holder and clamped by a split sleeve and clamp ring technique. Brass was used throughout in order to minimize thermal effects due to differential expansion. The membrane was made from 0.004 inch thick brass foil that was annealed and subsequently dimpled with a 0.02" radius by 0.03" deep by 0.70" diameter ridge in essentially a hydro-press operation using a machined die and rubber pillow block. This technique made it possible to produce uniformly prestressed diaphragms. The membrane resonant frequency was approximately 2000 cps, a value well above the operating range.

A sketch of the pressure transducer is shown in Figure A.1, including the 0-ring seals used to isolate the front and back faces of the diaphragm, and the attachment nut which was tightened with a spanner wrench due to space problems inside the instrumentation section.

The 100 KC carrier system was designed to drive two instrumentation sections simultaneously using four fifty foot long Microdot twin lead shielded cables, thereby permitting the instrumentation to be remote from the model. Each of the four cables was connected to a network inside the model which performed an analog summation of the pressure changes at the nine pressure pickups. The summing

network, as shown on Figure A. 4, consisted of three parallel circuits, each having three pressure pickups hooked in series. Because of the manner in which inductances combine electrically, the carrier system couldn't distinguish the number of pressure transducers since the total impedance would be almost the same for a high Q coil network in the case of either one or nine coils. The choice of using nine pickups was a consequence of the summing network being made up of $N^2$ elements where N is an integer.

A trimming capacitor, whose size was experimentally determined, was located at the load end of the transmission line in order to tune the circuit. By selective assembly, each group of nine pressure transducers had the same sensitivity within $\pm$ 3 per cent.

The pressure orifices were arranged in the instrumentation package in the manner as shown on Figure A. 5. Two complete sections were constructed in this manner. There were eighteen pressure orifices for each section, nine upper and nine lower respectively, located on the cylinder at the midpoints of nine uniformly spaced divisions as defined on a projection to a diameter. This arrangement made possible direct summation, avoided the need for weighting factors, and allowed the full measuring potential of each transducer to be used for summation. Since the upper and lower summing circuits were supplied as input to a differential amplifier, the amplifier output was proportional to total load according to the relation:

49

$$\ell(t) = \sum_{n=1}^{9} (P_\ell - P_u)_n \qquad\qquad (A.01)$$

where

$P_\ell$ = Static pressure at circumferential station,

n (lower surface)

$P_u$ = Corresponding value at upper surface.

The instrumentation sectors were oriented to read fluctuating lift loads, but rotation of a sector by ninety (90) degrees permitted measurement of drag.

The carrier system, which was unique for this series of testing, is shown in block diagram form on Figure A. 6. The highlights of the design were as follows:

a. A single 100 KC crystal controlled oscillator

provided R. F. (radio frequency) excitation to all

networks in order to avoid the possibility of

"beating" between channels.

b. The upper and lower sectors of an instrumentation

package (shown as $Z_1$ and $Z_2$ for a typical channel)

were each connected by 50 feet of Microdot shielded

twin lead cable to an unbalanced bridge circuit. The

unbalanced bridge circuit made it possible to

compensate for differences in overall sensitivity

between $Z_1$ and $Z_2$ in addition to making it possible

to sense the difference between the pressure summa-

tions of each sector.

c.  The feedback stabilized differential amplifier had
a high rejection ratio and subsequently acted to
keep the noise level to a low value.  The output
noise level of the complete carrier system was
less than 0. 5 milli-volts and was mainly composed
of R. F. signal.

d.  The zero adjustment or reference voltage was
introduced into the system between the amplifier
and the final filter and compensated for the zero
offset in the unbalanced bridge network.  Its loca-
tion in the system was such that it maintained its
adjustment automatically during changes in the
R. F. excitation signal.

e.  The final filter before the output terminals consisted
of two "half filters" set for 100 and 200 KC plus a
$\pi$(pi) filter in the center to act as a low pass filter.
The output signal could vary in the range of D.C. to
7500 cps.

A brief investigation was made of the dynamic response
characteristics of static pressure orifices by means of a parametric
study.  The experimental results confirmed the well known dynamic
analogy between the pressure orifice and a single degree of freedom
damped spring-mass system.

The experimental setup used to evaluate the frequency response
traits of the static pressure orifices is sketched in Figure A. 7.  As
can be noted, a Jensen (Model D-40) drive unit symmetrically excited

a cylindrical cavity, at either end of which was installed a pressure transducer. The two pressure transducers operated through separate 100 KC carrier systems (earlier model of carrier system described on preceding pages) and monitored on a dual beam oscilloscope, output levels measured on a Ballantine true RMS voltmeter, and phase differences observed on an AD-YU phase meter (after being amplified by two Epsco D. C. amplifiers). A system schematic is shown on Figure A. 8.

An off-center orifice (relative to the membrane face) was considered since the space requirements inside the instrumentation package precluded a simple chordwise spacing of both orifice holes and transducer centerlines. The staggering of orifices and transducers was established by means of a mockup. Since seven out of each group of nine orifices required that the orifice be 0. 20 inches offset from the diaphragm centerline, the calibrations shown on Figure A. 9 correspond to this situation. The effect of off-setting the orifice was experimentally verified as being small, though discernible.

Orifice gain as presented on Figure A. 9 is defined as the ratio of reference pressure pickup output with and without the simulated static pressure orifice. Physically it represents the attenuation of oscillating pressure signal during transmission through the pressure orifice into the cavity volume, and does not include the effects upon signal gain due to the actual pressure transducer dynamic characteristics. The orifice phase angle shift (lag) corresponds to the effect of the orifice in the same manner as mentioned above for cavity gain.

The three sets of data on Figure A. 9 correspond to three different levels of speaker excitation, namely approximately 0. 08, 0. 12, and 0. 16 psi (RMS) for the curves shown by the symbols $\odot$, $\triangle$, and $\square$ respectively. The resonance frequency (880 cps) was determined by noting the frequency for ninety degrees phase shift, since the response curves showed heavy damping and could not be used to establish resonance.

The response curves of Figure A. 9 were considered from the standpoint of an idealized model. Both the values of maximum gain and the frequencies at which they occurred were in good agreement with the idealized model when the damping ratios were assumed as $\gamma$ = 0. 64, 0. 68, and 0. 71 for the 0. 08, 0. 12, and 0. 16 psi (RMS) excitation curves respectively. It may be concluded that the orifices behaved as if they had approximately 65 per cent of critical damping, although the damping varied slightly with excitation showing some system non-linearity. The dashed fairing curves on Figure A. 9 correspond to the idealized model with a damping ratio of $\gamma$ = 0. 64 and a resonant frequency of 880 cps, and are shown for purposes of comparison.

Since the experimental results did not show any energy contributions from frequencies above 200 cps, no corrections were made for either orifice or pressure transducer dynamic response characteristics during the data analysis.

A. 3    Pertinent Considerations:

Tests were undertaken in the GALCIT Ten-Foot Wind Tunnel upon a cylinder model with end plates in order to qualify the load measuring instrumentation concept which was used on the subsequent cantilevered cylinder model. Hot-wire techniques were employed to sense flow velocities and fluctuations in a region just out of the boundary layer, but near to the flow separation point on the cylinder. Hot-wire probes were mounted on a traverse frame in such a manner that their presence produced a negligible flow interference on the model.

The model, as shown in Figure A. 10, consisted of an aluminum cylinder, 48. 25 inches in span and 6. 50 inches in diameter, supported between two 36. 0 inch diameter endplates which were in turn supported on the conventional wind tunnel strut system. The rear view of the model, Figure A. 10, disclosed the traversing system located parallel to the cylinder axis from which the hot wires were supported. A streamlined fairing shielded the traverse mechanism from direct exposure to the airflow in order to reduce hot wire motion. Although the fairing produced a flow perturbation on the cylinder surface, it was assumed that the perturbation was both slight and steady and that it did not modify any influences due to simulated instrumentation. A remotely controlled lead screw allowed one of the two upper hot-wire supports to be moved while the tunnel was in operation, thereby permitting the determination of cylinder flow characteristics in a spanwise direction and also correlation measurements with a second hot wire located on a fixed support. The hot wires were made from

0.0002 inch diameter tungsten wire that was spot welded to the tips

of two needles spaced 0.08 inches apart.

Two aluminum cylinder models were constructed. The first

was a single cylinder without any abrupt surface discontinuities other

than slight machining marks not removed during the hand polishing

operation. The second cylinder, similarly finished, consisted of two

23 inch long sections plus a two inch spacer section at the center.

The spacer section simulated a removable instrumentation package

as might be used on any subsequent tests.

The results of hot-wire measurements and observations

disclosed that:

1. The effects of a chordwise gap 0.010 inch wide by 0.15

inch deep disturbed the locus of the flow separation points in the

supercritical Reynolds number range (when the separation point is

aft of the maximum thickness point) and the disturbances were evident

at distances in excess of a cylinder diameter away from the crack.

The effects of the crack were not noticable in the subcritical Reynolds

number region when the separation point on the cylinder was in the

forward position. --- The use of a strain gage type load measuring

device was ruled out by these results since the desired load

measurements were to be in the supercritical Reynolds number range.

2. The effect of a joint as produced by the spacer cylinder

did not appear measurable. --- This made acceptable the use of

removable instrumentation sections on a circular cylinder, providing

that good control was maintained on surface tolerances during final

machining operations.

3. The effects of 24 uniformly spaced static pressure orifices (0.020 inch diameter) plus the simulated pressure reservoirs as might be encountered in a pressure pickup did not appear measurable. --- This result justified the use of remote indicating pressure pickups.

4. Since the data were qualitative in nature, a few remarks can be made regarding the power spectrum of velocity fluctuations and the correlation coefficient between two fluctuating velocity components. The power spectrum checks indicated no appreciable energy terms in the frequency range above 200 cps for a typical hot wire measurement behind the separation point on the cylinder when operating in the supercritical Reynolds number range. The correlation coefficient for fluctuating velocities was observed to approach zero with hot wire spacings in excess of one cylinder diameter in both the sub and supercritical Reynolds number ranges used in the test ($3.5 \times 10^5 < R < 5.7 \times 10^5$).

In addition to considering the aerodynamic influence of the instrumentation upon the mechanism of flow separation, calibrations were performed to determine the inertia loading effects upon the pressure transducers. The former effects were evaluated on the cylinder model with end plates while the latter effects were investigated on the cantilevered cylinder model using the prototype of a dynamic model shaker at a zero airspeed tunnel condition.

Dynamic shaker tests disclosed that the structural interactions from cylinder bending stresses and inertia loadings from cylinder accelerations had small influences upon the pressure transducer output. A typical observation near a model resonance condition of 10 cps,

where the RMS value of acceleration at the instrumentation package

was 0.20 "g's", showed that the carrier amplifier channel output

increased from 0.40 mv. (noise level) to approximately 0.90 mv.

(noise plus dynamic effects). Since the acceleration response varies

with tunnel dynamic pressure in a manner similar to the variation of

unsteady load, an approximate estimate of power content disclosed

that the signal noise plus model dynamic interference effects contri-

buted less than 1/400 of the total signal power level at a tunnel

dynamic pressure of 40 psf. At a lower level of tunnel dynamic

pressure (10 psf), inertia effects became less important relative to

signal noise, and an estimate at this condition showed that the noise

power represents approximately 1 per cent of the signal power.

## APPENDIX B

## DATA HANDLING

B. 1    Recording:

The recorded data consisted of the output of two carrier amplifier channels which provided a measure of sectional air loads, and the output of two strain gage type accelerometers mounted on the model.

A seven channel Ampex FR-100 tape recorder was used to record data on one inch magnetic tape at a tape speed of 7. 5 inches per second.  Tape recorder channels 1 and 2 were used to record the two air load data measurements, while accelerometer data were recorded on channels 3 and 4.  The data recording amplifiers were FM (frequency modulated) and were capable of recording data in the frequency range from D. C. to 1250 cps.  Voice identification was recorded at the start and end of each record using a direct reproduce amplifier on channel 7.  The two remaining channels were unused, but a 1 KC pulse train was recorded for 10 seconds on a selected group of records at a later date using a direct reproduce amplifier on channel 6.

A calibration panel provided a convenient method for recording calibration voltages onto magnetic tape.  Consequently, zeros and known voltage levels in the range of $\pm$ 1. 4 volts (D. C. ) were recorded frequently during actual data taking in order to assure that the tape recorder amplifier circuits were in proper adjustment and to provide reference levels for subsequent tape data playback.

A central switch panel was employed for data monitoring before and after signal amplification through amplifiers, before recording on magnetic tape, and after playback from magnetic tape. All voltage adjustments and measurements were made prior to recording data, and the recorder input and output signals were continually monitored while recording on tape using the D. C. response side of a Dumont Model 411 dual beam oscilloscope in order to assure that random peaks or unforeseen changes in D. C. level of the input signal did not "drive" any tape recorder channel beyond the nominal linear range.

When the record and reproduce amplifiers of the tape recorder are in average condition, and when care is used in performing calibrations and data monitoring, the recording of data on magnetic tape will result in accuracies of signal voltages to approximately 1 per cent of full range, i. e., $\pm$ 0. 015 volts, on the assumption that the recorder is operating in a linear manner.

A schematic of the data recording circuitry is shown on Figure B. 1. Of special note is the use of a "bucking" voltage on the differential input of the Epsco D. C. amplifiers prior to data recording on magnetic tape. In this way, the input signal from the carrier amplifiers could be biased to approximately a zero volt D. C. level, and subsequently permit the tape recorder to be used predominantly for recording a fluctuating signal. Although a D. C. voltage would be expected for the instrumentation sections when in the drag mode of operation, it was also noted many times that a D. C. voltage would develop in an unpredictable manner for the lift mode operation.

The two accelerometer channels used a bridge voltage of 6.4 volts (D.C.) and the two output signals of the Wheatstone bridge circuit were supplied as inputs to both input grids of the Epsco differential amplifiers. A bridge zero adjust was provided in a conventional manner such that the output of the Epsco amplifiers could be set at zero for a zero "g" condition.

The unsteady voltage signals were monitored and measured during the test using a Ballantine Model 320 True RMS meter. The unsteady lift and drag coefficients presented in the main body of this report are based upon these measurements, although the tape data could also have been used to determine the coefficients. The D.C. voltage measurements were made on a Brown D.C. voltmeter.

B.2   Analog Reduction:

The tape data were analyzed by analog means in order to obtain an estimate of the cross correlation coefficient and correlation length as defined in Section III. A time history of the analog representation of both mean squares and cross-products were used to estimate the degree of signal cross-correlation and to indicate regions of tape data suitable for subsequent digital analysis. It was necessary to use an averaging circuit with a low output impedance since the time histories were graphically recorded by an instrument with a relatively low value of input impedance. The averaging circuit, which satisfied the impedance requirements, consisted of an analog computer type D.C. amplifier with a resistance and capacitance connected in parallel in the negative feedback loop. The system

schematic is shown on Figure B. 2. The circuit constants selected in the analog computer corresponded to a static voltage gain of approximately -7. 5 and a time constant of 9 seconds, i.e. input resistance $(R_i)$ = 1. 2 x $10^6$ ohms, feedback resistance $(R_f)$ = 9 x $10^6$ ohms, and feedback capacitance $(C_f)$ = 1 x $10^{-6}$ farads. A nine second time constant can be interpreted in two ways as follows:

1. If a step type voltage were applied as an input signal to the analog computer at time $t_o$, the output voltage would be 63 per cent of the steady state value at time equals $t_o$ + 9 seconds. This check was frequently made in order to confirm circuit operation.

2. If a one cps voltage signal were used as input, the magnitude of the output would be 1. 7 per cent of the input value. Higher frequencies would be more heavily attenuated.

The nine second time constant was chosen on the basis of providing a moderate amount of "smoothing" to the plotted data. A longer time constant would have been undesirable since it would then have been difficult to select regions of the tape data suitable for subsequent digital analysis.

The first curves plotted in a group of five were $\overline{e_1(t)}$ and $\overline{e_2(t)}$ in order to make circuit adjustments. The symbols $\overline{e_1(t)}$ and $\overline{e_2(t)}$ refer to primary and secondary records of voltage respectively. Since the tape recorder signals were amplified using Epsco D. C. amplifiers prior to introducing the signal to the averaging circuit, it

was possible to bias the D. C. level of the amplified voltage signal by means of a "bucking" voltage applied to one of the two input grids of the Epsco amplifier. As a consequence, both $\overline{e_1(t)}$ and $\overline{e_2(t)}$ could be set at approximately zero over a common period of time.

The $\overline{e_1(t)}$ and $\overline{e_2(t)}$ terms represent a D. C. (or low frequency) term from the tape recorder output and can arise either from a shift or mismatch of the center frequency in a tape recorder FM amplifier (either record or playback), or by the occurrence of a shift in the static value of aerodynamic loading. The former problem can be handled by taking frequent calibration records of zero voltage input, which is a problem only in technique. The latter situation was quite commonplace as observed during data recording, and cannot be avoided in an analog type data reduction procedure where low frequency response is of interest. The remaining group of three curves, namely $\overline{e_1^2} + (\overline{e_1})^2$, $\overline{e_2^2} + (\overline{e_2})^2$, and $\overline{e_1 e_2} + (\overline{e_1})(\overline{e_2})$ were obtained using a Philbrick K5M multiplier between the Epsco amplifiers and the analog computer. The Philbrick K5M multiplier was used in a "Mode 3" operation.

The criteria used for selecting tape recorded data for digital analysis were somewhat arbitrary. The plots of mean average and mean squares did not appear stationary in a strict sense, i. e., invariant with respect to changes of time origin, probably because the time constant of the averaging circuit was not large enough. An arbitrary condition for a portion of tape data to be selected for digitizing was that both the mean average and mean squares should appear relatively invariant over at least a common 20 second period

of time for the primary and secondary records simultaneously. This method of tape record selection avoids the influence of unknown effects such as might be induced either by the occurrence of slight variations in tunnel air speed during a 5 minute data recording period, or by random impacting of dirt particles on the model near to an otherwise physically clean instrumentation package.

As has been mentioned, selected portions of the tape data were converted to digital form using equipment made available by the Engineering Facilities Division of the J. P. L. (Jet Propulsion Laboratory, C. I. T.). The maximum digitizing rate of the machine was 3000 numbers per second, which was more than adequate to handle the chosen sampling rate of 1000 numbers per second.

Since only one channel of digitizing equipment was available, it was necessary to digitize the primary and secondary data records separately. Therefore a clock was "dubbed" onto channel 6 of the magnetic tape in order to assure time synchronization of both data records. This was done as follows: A crystal controlled Berkeley Universal Counter and Timer, Model 550I, generated a 10 second train of 10,000 pulses upon manual command. The pulses were used to trigger square wave pulses in a Rutherford Pulse Generator, Model B7B, of 400 $\mu$ second width and going from 0 to 15 volts peak. The square wave pulses were then used as input to a direct record amplifier on channel 6 of the tape recorder. Because of the frequency response limitations of the tape recorder amplifier, the square wave pulse was modified considerably. In spite of this limitation, the tape recorder pulse train was estimated on playback as being able to trip

a gate circuit within $\pm$ 5 $\mu$ seconds for a pulse that repeated every

millisecond. In practice, the clock channel on the magnetic tape

proved adequate for controlling the gate circuit in the digitizing

equipment.


B. 3  <u>Digital Reduction:</u>

The digital analysis of the tape recorder voltage analog of

unsteady loads has been made using fundamental computing tech-

niques as outlined by Press and Tukey (18). The digital procedure

first estimates the auto- and cross-correlations for two records at

the same equally spaced intervals of time. Then the appropriate

Fourier cosine or sine transformations are made to provide esti-

mates of the power spectral and cross-spectral densities. The

input tape data records contain digital values in a form suitable as

input to a FORTRAN coded program on the I. B. M. 7090 computer

(25).

The procedure for obtaining the spectra of the input records

assumes that $x_1$, $x_2$,..., $x_n$ and $y_1$, $y_2$,..., $y_n$ represent two

series of data at times $t_1$, $t_2$,..., $t_n$ where the time intervals are

equi-spaced. The first step in the program is to adjust the input

data such that the mean average of each complete record is zero,

i. e.,

$$\sum_{i=1}^{n} x_i = \sum_{i=1}^{n} y_i = 0 \qquad\qquad (B.01)$$

The correlations are estimated for values of the index L from

0, 1, ..., M. The auto-correlations for the two records are

expressed by:

1.      Primary record auto-correlation:

$$A(L) = \frac{1}{(n-L)} \sum_{i=L+1}^{n} x_{i-L} x_i - \frac{1}{(n-L)^2} \sum_{i=L+1}^{n} x_{i-L} \sum_{i=L+1}^{n} x_i$$

(B. 02)

2.      Secondary record auto-correlation, B(L), corresponds to

the equation for A(L) with "y" substituted for "x". The cross-

correlations are developed in the form of a forward and rearward

cross-correlation separately.

3.      Forward cross-correlation:

$$C(L) = \frac{1}{(n-L)} \sum_{i=L+1}^{n} x_{i-L} y_i - \frac{1}{(n-L)^2} \sum_{i=L+1}^{n} x_{i-L} \sum_{i=L+1}^{n} y_i$$

(B. 03)

4.      The rearward cross-correlation, D(L), is obtained by a

relation similar to that for C(L) except that the roles of "x" and

"y" are interchanged.

For convenience in developing the cross-spectral densities,

the forward and rearward cross-correlations are combined to form

the following relations:

5.      The in-phase cross-correlation between the two records is:

$$E(L) = 0.5 \left[ D(L) + C(L) \right]$$

(B. 04)

6.　　The out-of-phase cross-correlation is:

$$F(L) = 0.5 \left[ D(L) - C(L) \right] \qquad \text{(B.05)}$$

These expressions for the correlation functions are then combined to form a series approximation of a Fourier cosine or sine transform for values of the index K from 0, 1, ..., M which provides an estimate of the spectral density. The power spectral densities are defined by:

7.　　Power spectrum of primary record:

$$X(K) = \frac{\delta K}{M} \left[ A(0) + \sum_{L=1}^{M-1} e(L) \cos \frac{KL\pi}{M} A(L) \right] \qquad \text{(B.06)}$$

8.　　The power spectrum of the secondary record, Y(K), is obtained by substitution of secondary record auto-correlation functions "B" for "A" in equation for X(K).

9.　　The real part of the cross-spectrum between the two records provides a measure of the in-phase power and is called the co-spectrum. The series approximation is given by:

$$Z(K) = \frac{\delta K}{M} \left[ E(0) + \sum_{L=1}^{M-1} e(L) \cos \frac{KL\pi}{M} E(L) \right] \qquad \text{(B.07)}$$

10.　　The imaginary part of the cross-spectrum, called the quad-spectrum, provides a measure of the $90^{\circ}$ out-of-phase power (quadrature power) and is approximated by:

$$W(K) = \frac{\delta_K}{M} \sum_{L=1}^{M-1} e(L) \sin \frac{KL\pi}{M} F(L) \qquad (B.08)$$

In the preceding spectral density relations, the terms $\delta_K$ and $e(L)$ are defined as:

$$\delta_K = \begin{cases} 0.5 \text{ for } K = 0 \text{ or } M, \\ 1 \text{ for all other values of } K \end{cases}$$

$e(L)$ = Hanning factor (Reference 18) = $1 + \cos \frac{L\pi}{M}$

The selection of 10,000 digitized values of the primary and secondary data record was established by storage capacity limitations of the I.B.M. 7090 computer. In order to perform rapid machine computations of correlations and spectral densities, it was necessary to have the data, program routines, and computed numbers stored concurrently in machine memory. The I.B.M. 7090 computer, when used with a FORTRAN type program has available storage for 32,561 numbers or commands, which establishes an upper bound on the amount of input data stored at one time. A sampling rate of 1000 numbers per second was selected on the criteria of being at least twice the value of the highest frequency which might be encountered in the record, a procedure suggested by reference 18 in order to avoid "aliasing" difficulties[*]. In addition, the counter unit conveniently generated pulses at the 1 KC rate. The total length of the pulse train was dictated by a desire to be able to sample a low frequency term (say) 1 cps for ten times.

---

[*] In equally spaced data, two frequencies are aliases of one another if sinusoids of the corresponding frequencies cannot be distinguished by their equally spaced values.

Although the digital program receives as input 10,000
numbers for both data records at a time spacing of 0.001 seconds,
it is a program option to "thin" the data during the actual computa-
tion. If we define (M + 1) as the number of estimates desired, and
the time interval between each correlation function estimate as
$\Delta \tau$ (seconds), then:

1. $f_{max.}$  = maximum frequency (cps) = $1/(2\Delta\tau)$

2. $\tau_{max.}$  = maximum time shift for a correlation function

      = $M \Delta \tau$

3. $\Delta f$   = frequency interval between spectral density

      estimates, = $f_{max.}/M$

The maximum number of estimates of spectral density and
correlation function (501), although established primarily by
computer storage limitations, does reflect an approximate 1:20
relationship to the number of individual data points. If 501 esti-
mates were desired using a time spacing of 0.001 seconds on input
data consisting of a total of 20,000 numbers, approximately 45
minutes of I.B.M. 7090 computer time would be required. In prac-
tice, a more reasonable value was used which did not require in
excess of 4 minutes of computer time per case. It was noted that
approximately 99 per cent of the random power was contained in the
frequency spectrum below frequency values of 100 to 125 cps. Also
a one cps spacing of frequency estimates corresponds approximately
to a two cps band-width filter (electrical notation). Therefore either
101 or 126 estimates were computed with a time interval of 0.005 or
0.004 seconds respectively.

68
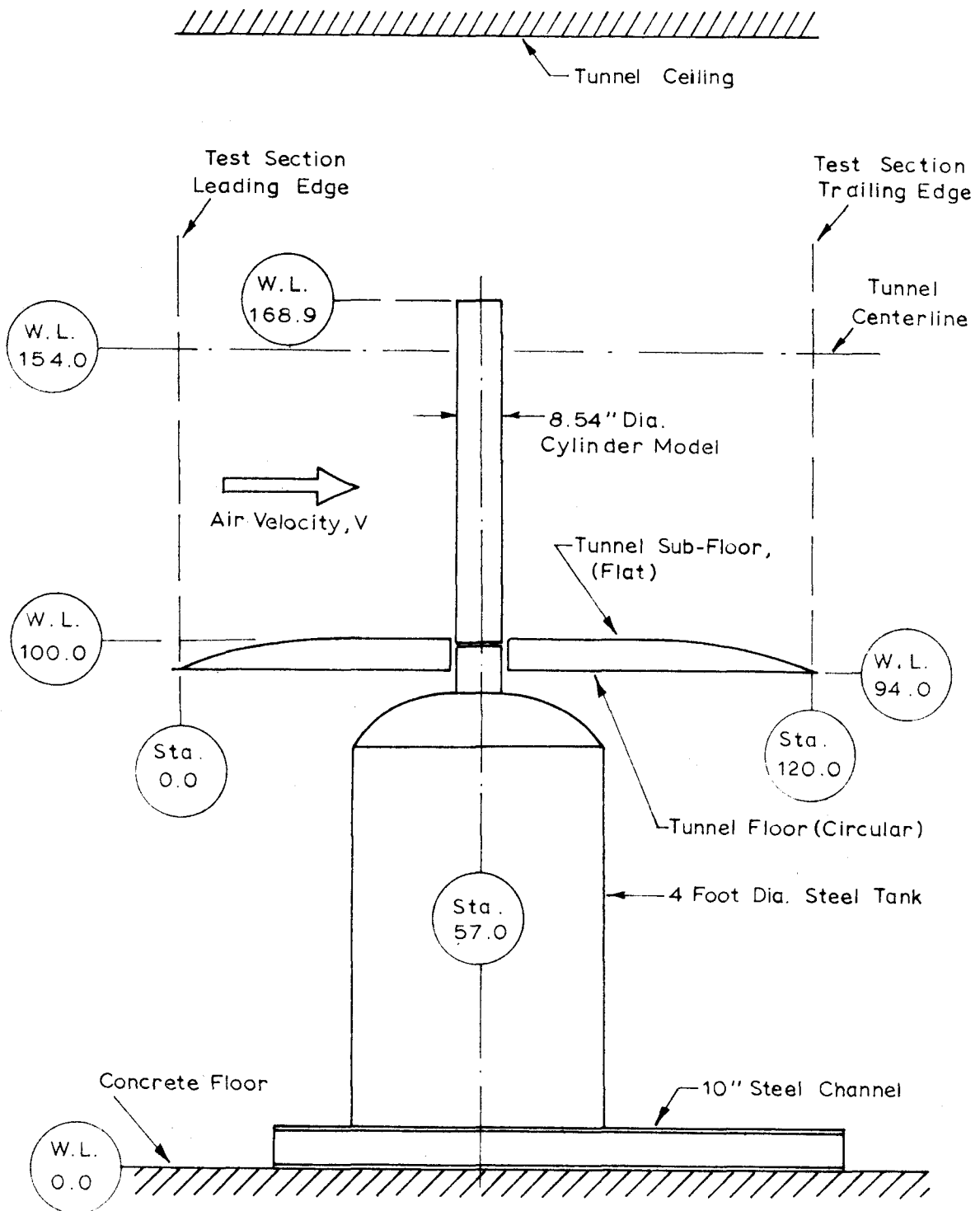


Figure 1    Model Installation in GALCIT
Ten-Foot Wind Tunnel

69
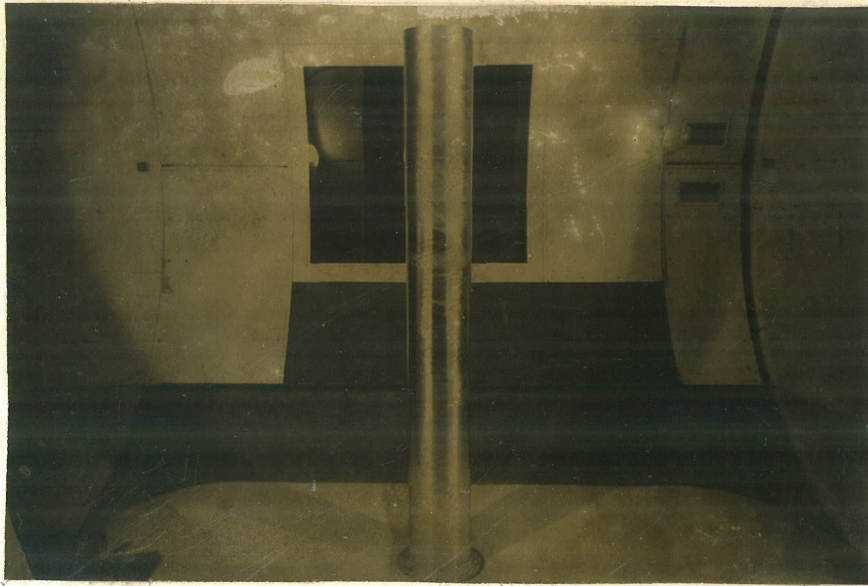


a. Side View
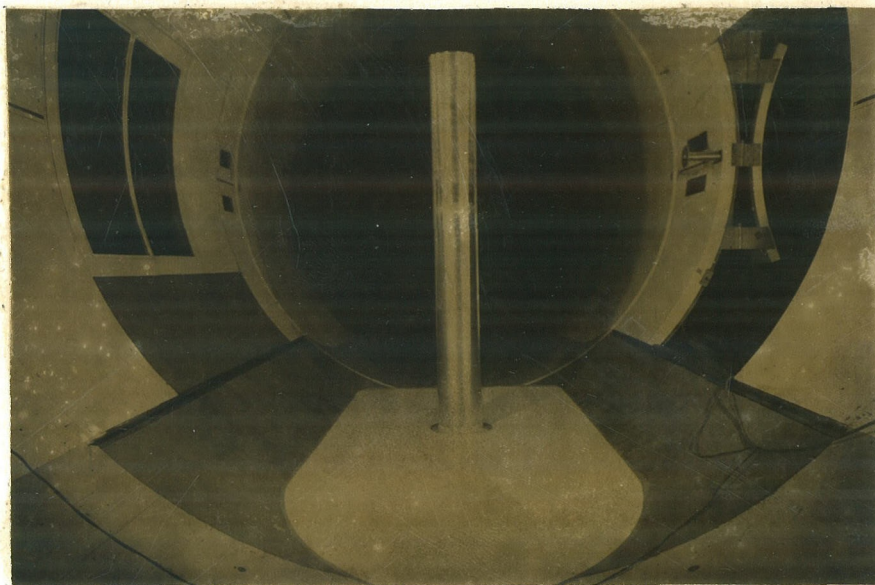


b. Front View

Figure 2     Cantilevered Cylinder Model
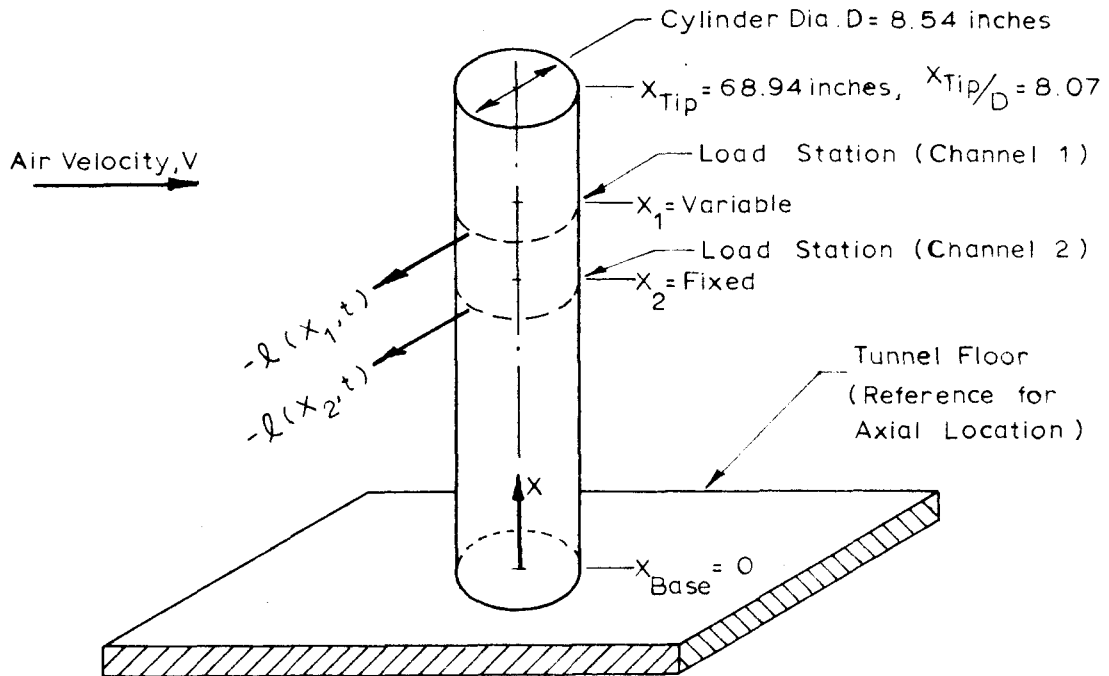
Note: Force Components Shown for Typical Case with Load Section
Oriented to Measure Local Lateral Forces.

Channel 2 Load Instrumentation:

$$X_2 = 41.49 \text{ inches}$$
$$X_2/D = 4.86$$
$$(X_{Tip} - X_2)/D = 3.21$$

Channel 1 Load Instrumentation:
Define $\Delta X = X_1 - X_2$

| $\Delta X/D$ | $X_1/D$ | $(X_{Tip} - X_1)/D$ |
|---|---|---|
| 0.316* | 5.17 | 2.90 |
| 0.516 | 5.37 | 2.70 |
| 0.716 | 5.57 | 2.50 |
| 0.916 | 5.77 | 2.30 |
| 1.016 | 5.87 | 2.20 |
| 1.116 | 5.97 | 2.10 |
| 1.316 | 6.17 | 1.90 |
| 2.116 | 6.97 | 1.10 |

*Adjacent Position

Figure 3    Axial Locations of Force Instrumentation

71
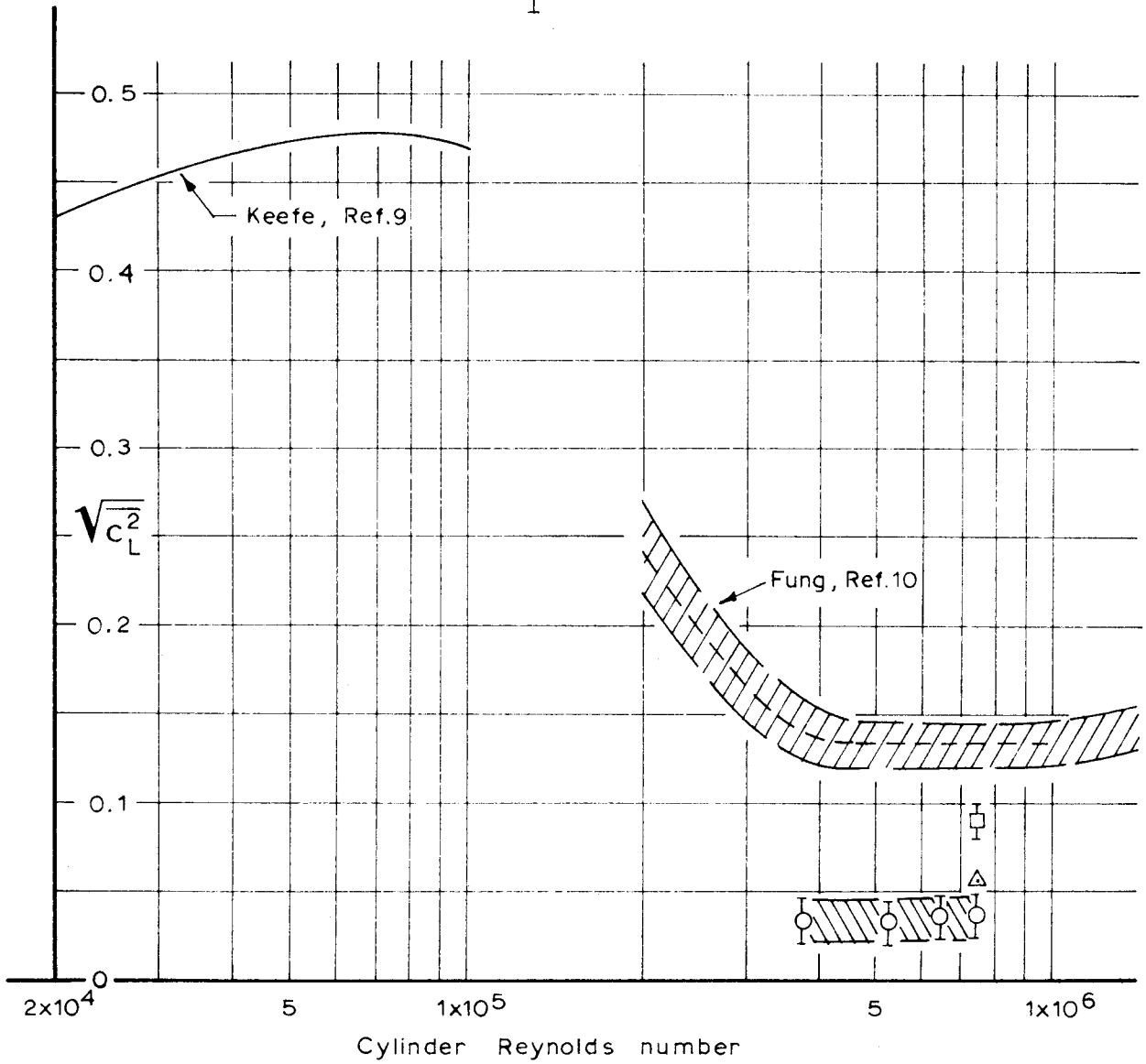


Figure 4     Summary of Unsteady Lift Results
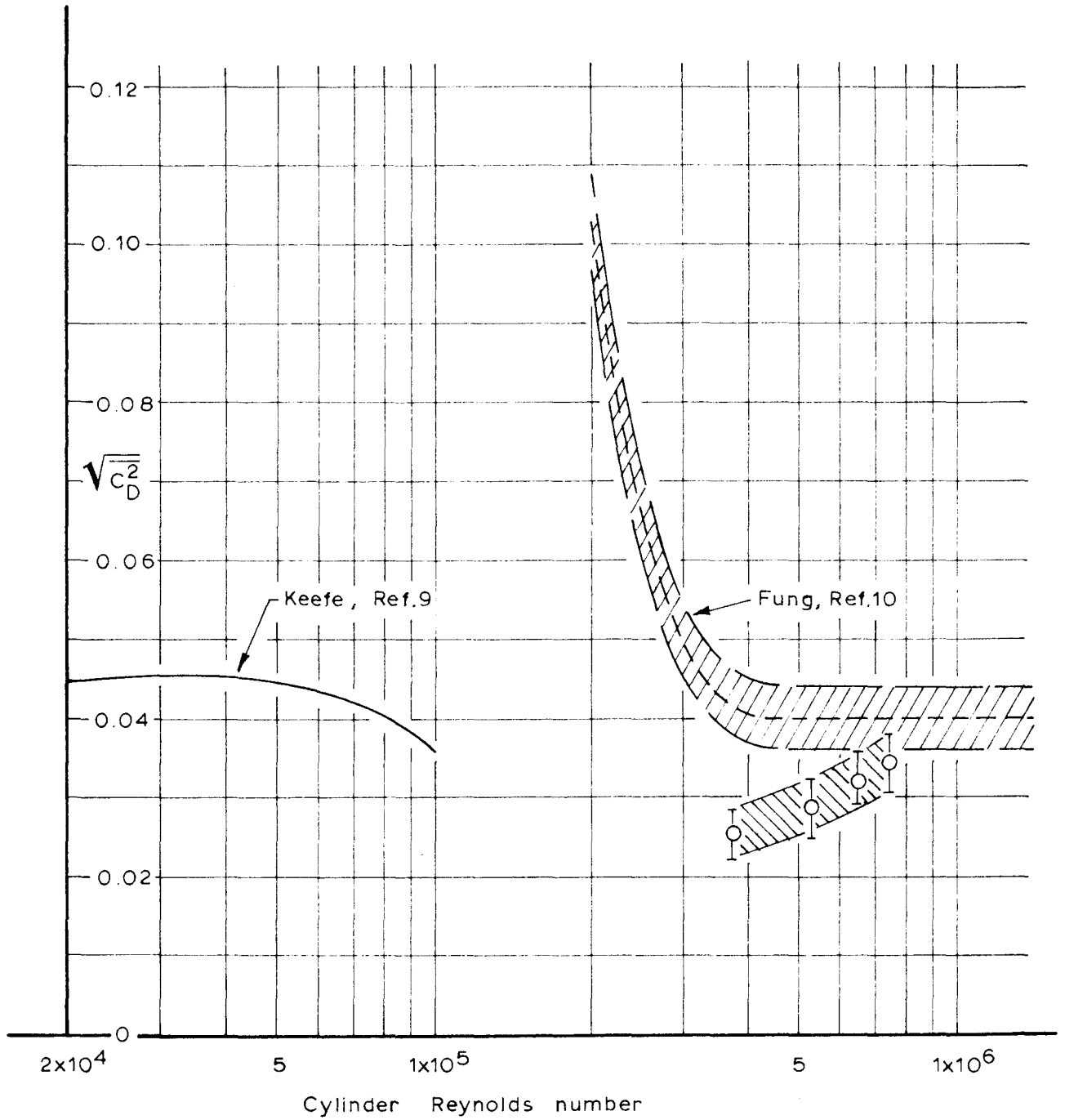
Figure 5     Summary of Unsteady  Drag  Results

Notes:
  1. Reynolds No. = $0.75 \times 10^6$, q = 40 psf
  2. Spacing between Load Stations,
     $\triangle X/_D$ = 0.316
  3. Data from Run 53/40-1
     with Same Time Base,
     a. ——— Channel 1, $X/_D$ = 5.17
     b. — — — Channel 2, " = 4.86
  4. Normalizing Factors Satisfy
     A.C.F. = 1.0 at $\tau$ = 0
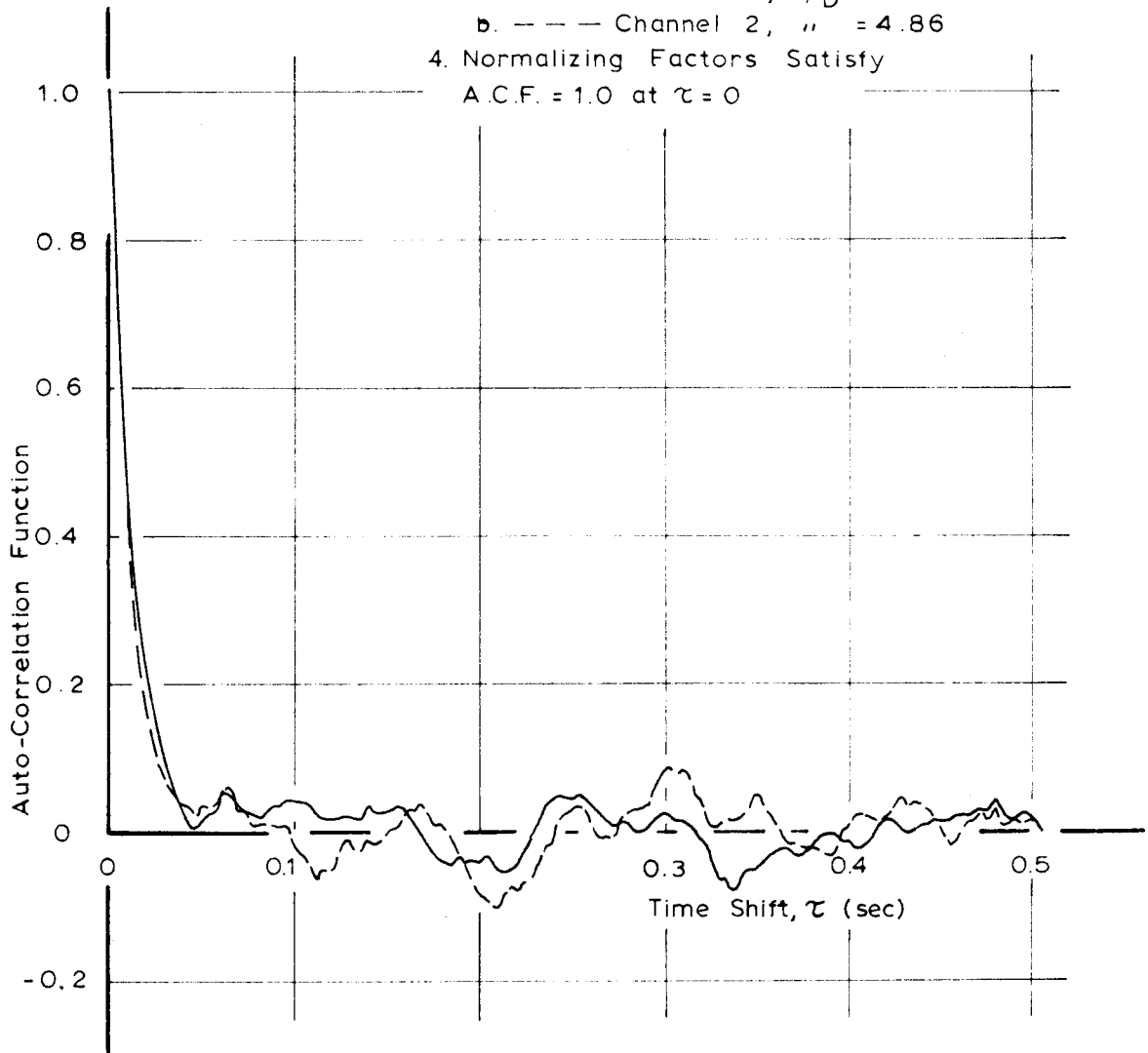


Figure 6    Auto-Correlation Function for Lift    Force

Notes:

1. Reynolds No. $= 0.75 \times 10^{6}$, q = 40 psf
2. Spacing between Load Stations,
   $\triangle X/_D$ = 0.316
3. Data from Run 53/40-1
4. Normalizing Factor to Set I.P.C.C.F. = 1.0
   at $\tau$ = 0 Applied to both I.P.C.C.F. and O.P.C.C.F.
5. Cross-Correlation Coefficient,
   $R_{\ell^2}$ = 0.555 (at $\tau$=0)

In-Phase (I.P.C.C.F.)

Out-of-Phase (O.P.C.C.F.)

Cross-Correlation Function

Time Shift, $\tau$ (sec)
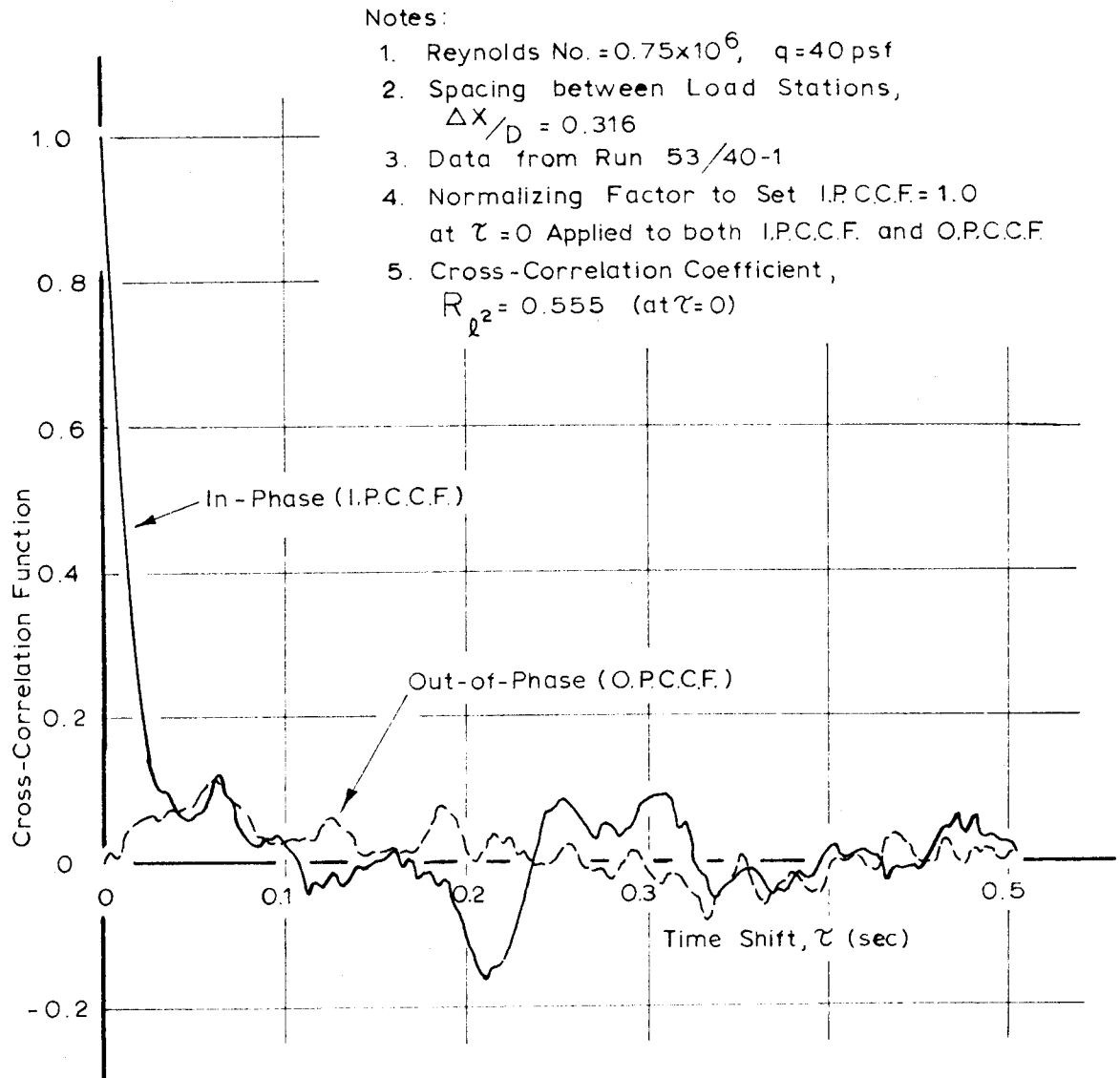
Figure 7    Cross-Correlation Function for Lift    Force
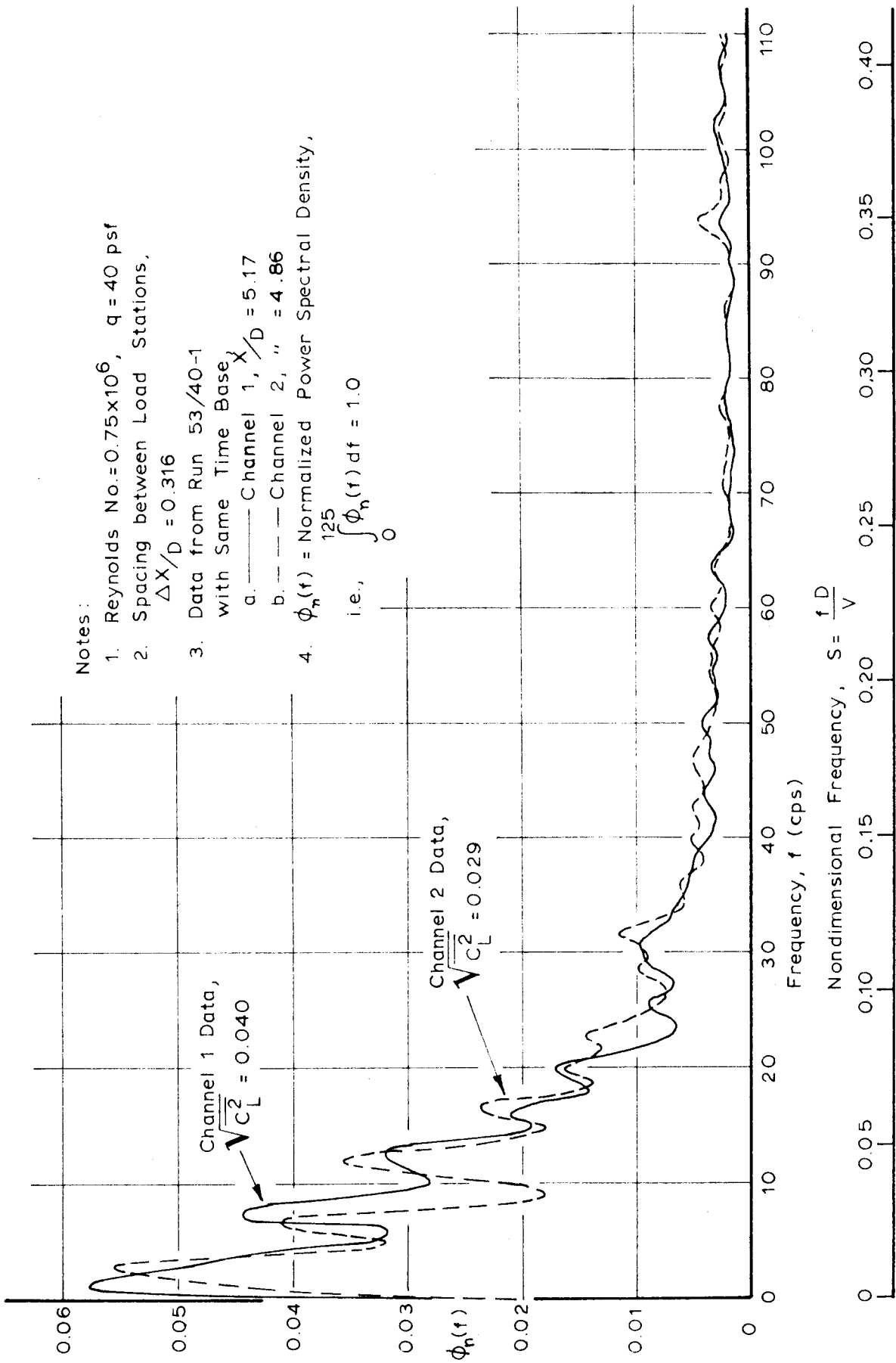
Figure 8   Power   Spectrum   for   Lift   Force
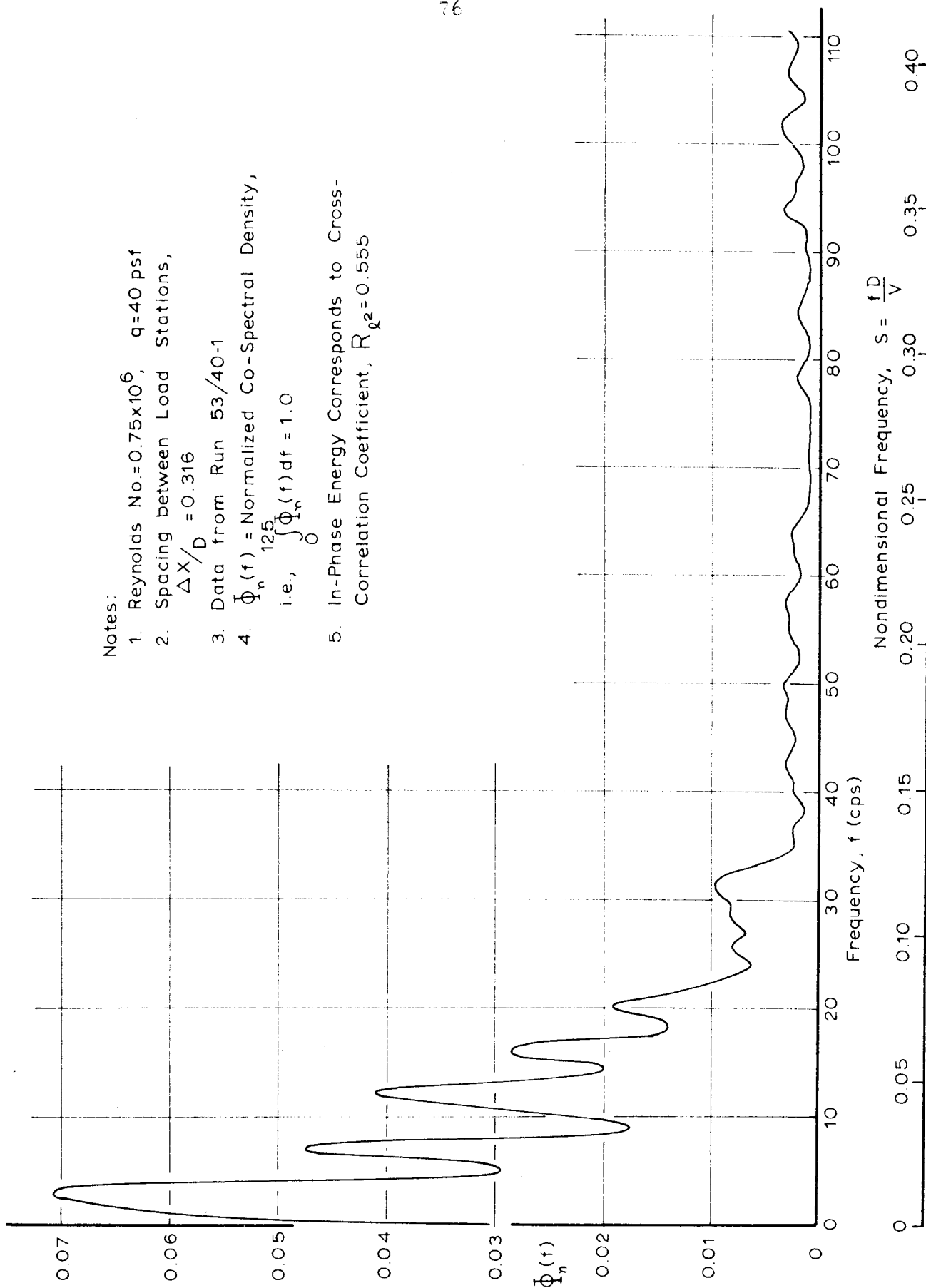
Notes:

1. Reynolds No.=$0.75 \times 10^6$, q=40 psf
2. Spacing between Load Stations,
   $\Delta x/D = 0.316$
3. Data from Run 53/40-1
4. $\phi_n(f)$ = Normalized Co-Spectral Density,
   i.e., $\int_0^{125} \phi_n(f)\,df = 1.0$
5. In-Phase Energy Corresponds to Cross-
   Correlation Coefficient, $R_{\rho^2} = 0.555$

$\phi_n(f)$

Frequency, f (cps)

Nondimensional Frequency, $S = \dfrac{fD}{V}$

Figure 9    Co-Spectrum for Lift Force
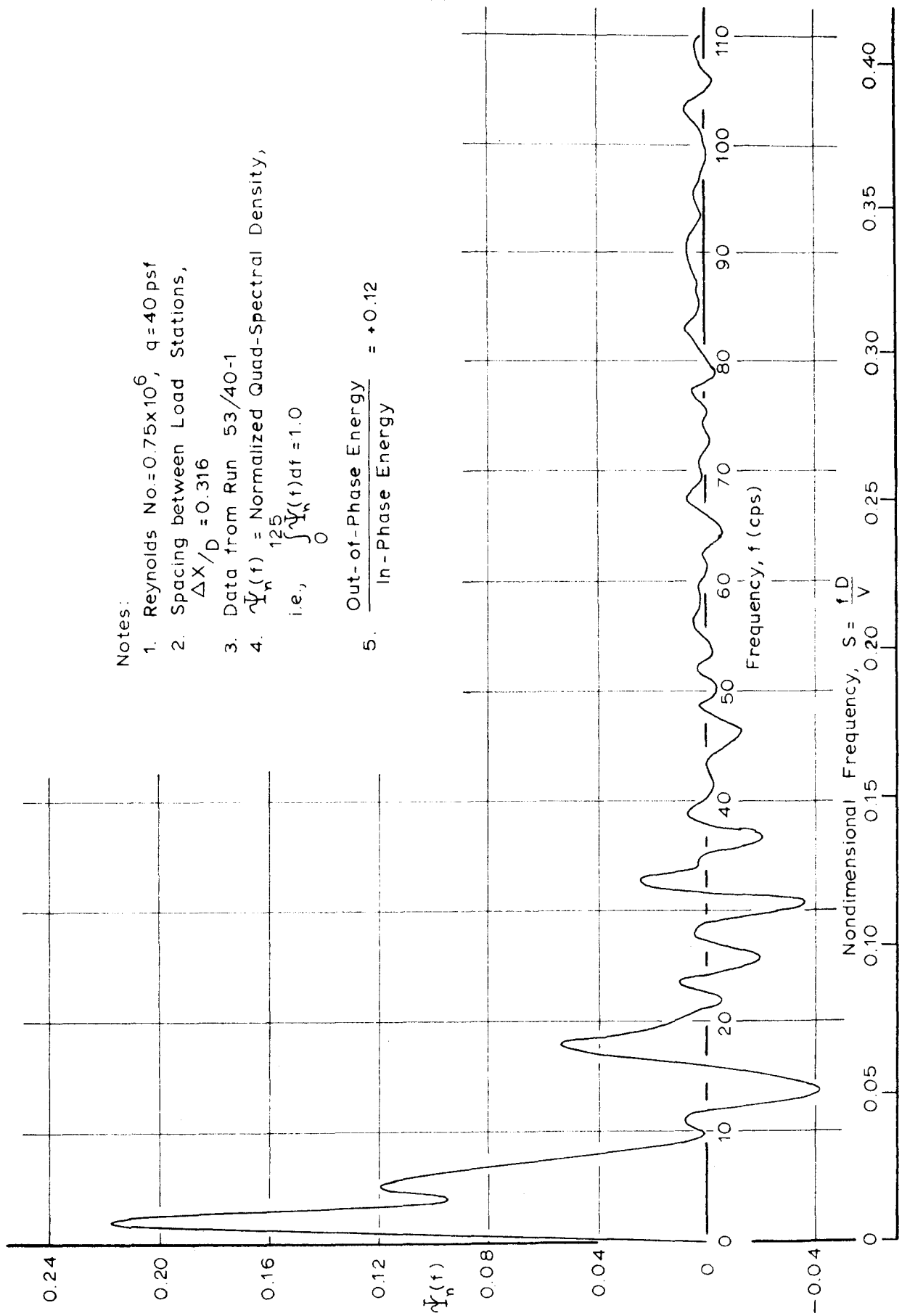
Notes:
1. Reynolds No.=0.75×10$^6$, q=40 psf
2. Spacing between Load Stations, $\Delta X/D = 0.316$
3. Data from Run 53/40-1
4. $\Psi_n(f)$ = Normalized Quad-Spectral Density, i.e., $\int_0^{125} \Psi_n(f)df = 1.0$
5. $\dfrac{\text{Out-of-Phase Energy}}{\text{In-Phase Energy}} = +0.12$

Frequency, f (cps)

Nondimensional Frequency, $S = \dfrac{fD}{V}$

Figure 10    Quad-Spectrum for Lift Force

Notes:
1. Reynolds No. = 0.75x10$^6$,  q = 40 psf
2. Spacing between Load Stations,
   $\Delta X/_D$ = 0.316
3. Data from Run 54/40
   with Same Time Base,
   a. ——— Channel 1, $X/_D$ = 5.17
   b. — — — Channel 2,  ,,  = 4.86
4. Normalizing Factors Satisfy
   A.C.F. = 1.0 at $\tau$ = 0
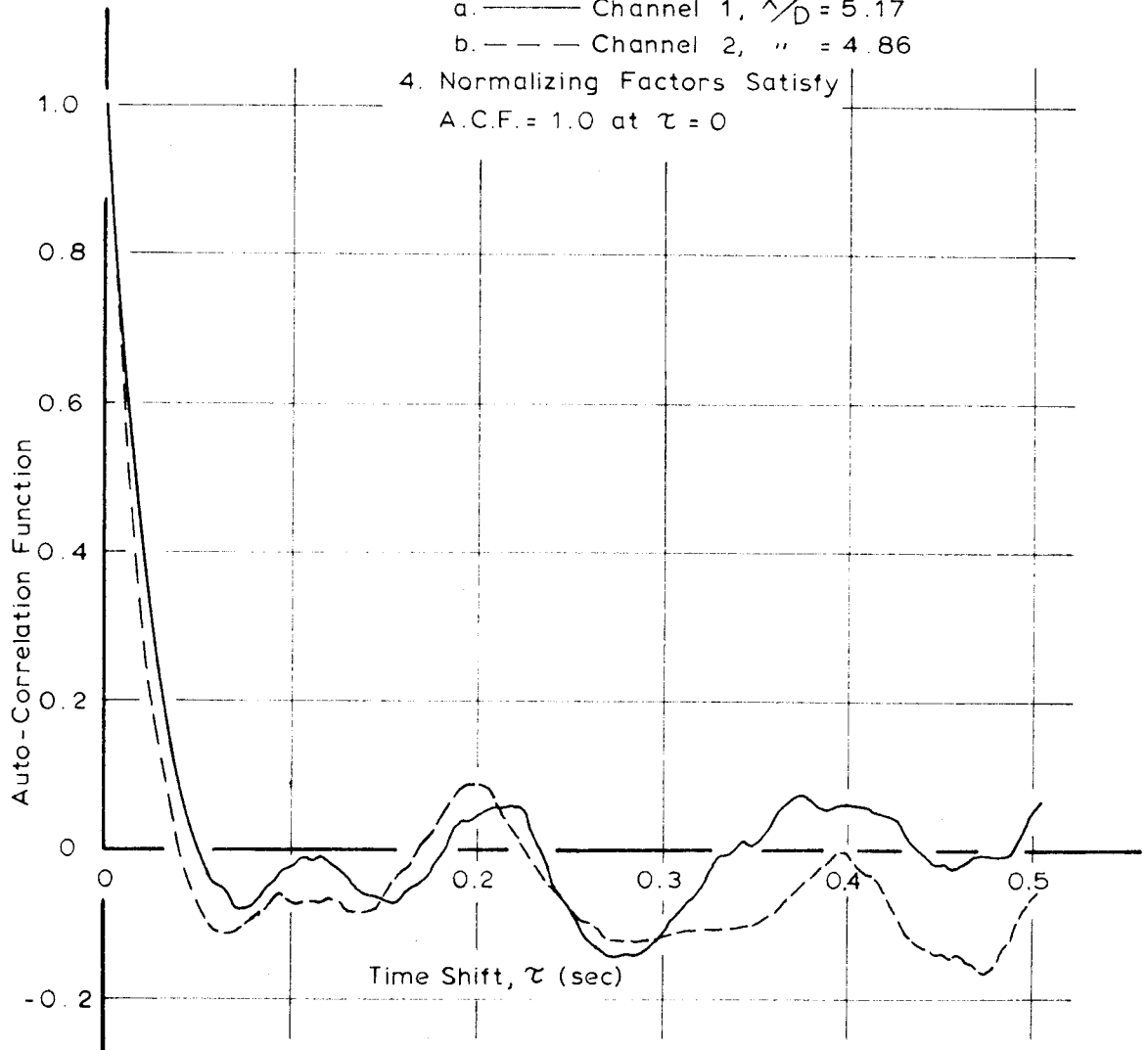
Figure 11    Auto-Correlation Function for Drag Force

79



Figure 12    Cross-Correlation Function  for Drag  Force
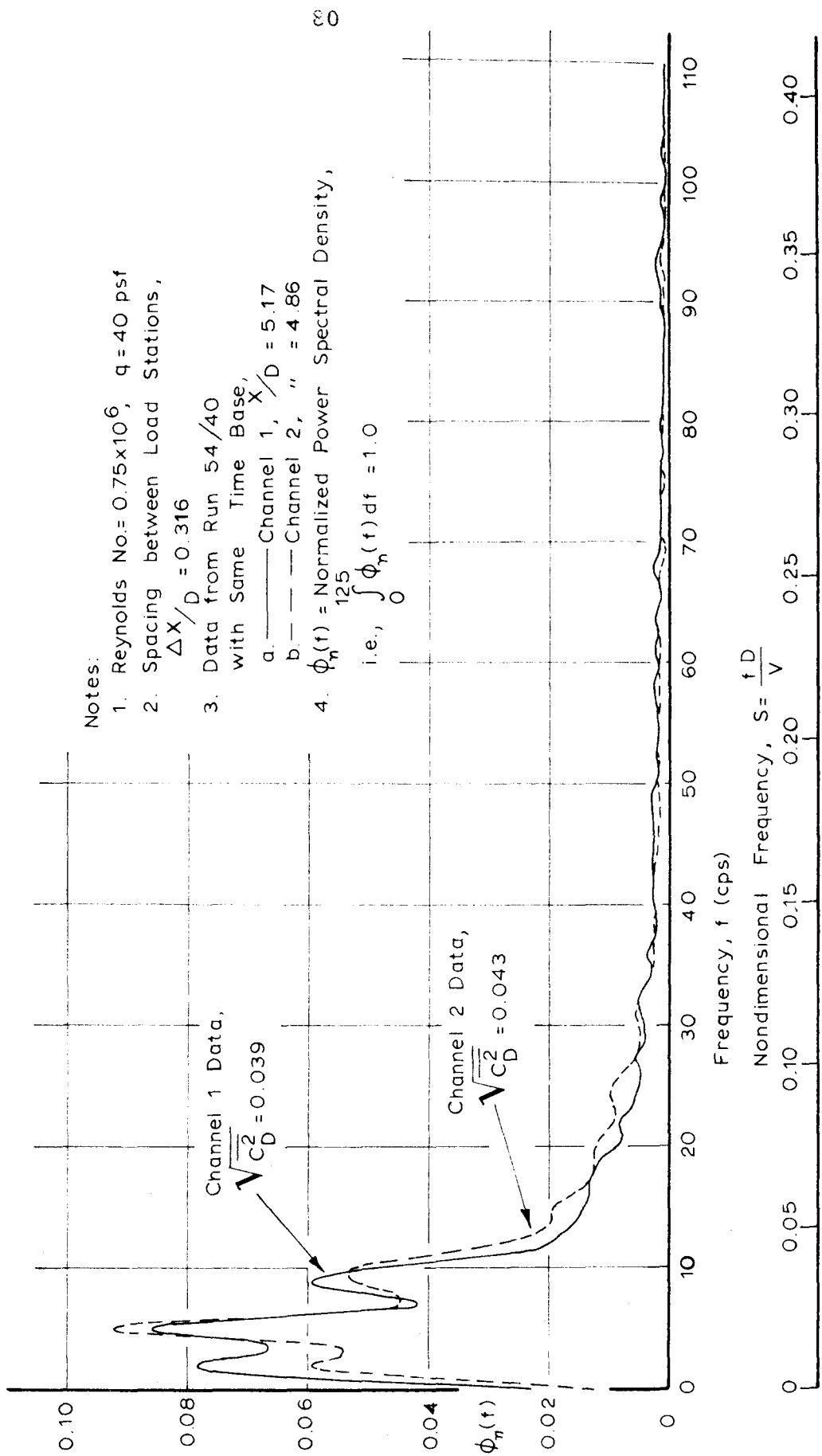
Figure 13   Power Spectrum for Drag Force

Notes:
1. Reynolds No.= 0.75x10^6,  q = 40 psf
2. Spacing between Load Stations,
   ΔX/D = 0.316
3. Data from Run 54/40
   with Same Time Base,
   a.——— Channel 1, X/D = 5.17
   b.— —— Channel 2, "  = 4.86
4. $\phi_n(f)$ = Normalized Power Spectral Density,
   i.e., $\int_0^{125} \phi_n(f)\,df = 1.0$

Channel 1 Data,
$\sqrt{\overline{C_D^2}} = 0.039$

Channel 2 Data,
$\sqrt{\overline{C_D^2}} = 0.043$

Frequency, f (cps)
Nondimensional Frequency, $S = \dfrac{fD}{V}$

$\phi_n(f)$

Notes:
1. Reynolds No.=$0.75 \times 10^6$, q=40 psf
2. Spacing between Load Stations, $\Delta X/D = 0.316$
3. Data from Run 54/40
4. Cross-Spectral Densities are Normalized, i.e., $\int_0^{125} \Phi_n(f)\,df = \int_0^{125} \Psi_n(f)\,df = 1.0$
5. In-Phase Energy Corresponds to Cross-Correlation Coefficient, $R_d^2 = 0.368$
6. $\dfrac{\text{Out-of-Phase Energy}}{\text{In-Phase Energy}} = -1.24$

Quad-Spectral Density, $\Psi_n(f)$

Co-Spectral Density, $\Phi_n(f)$

Nondimensional Frequency, $S = \dfrac{fD}{V}$

Frequency, f (cps)

Figure 14   Co-and Quad-Spectra   for Drag Force

Notes:

1. Reynolds No.=$0.75 \times 10^6$, q=40 psf

2. Data refer to Channel 2, Axial Location, $X_2/D = 4.86$

3. $\phi_n(X,f)$ = Normalized Power Spectral Density, i.e., $\int_0^{125} \phi_n(X,f)\,df = 1.0$

4. Legend

| | Fairing | Run | $\sqrt{\overline{C_L^2}}$ |
|---|---|---|---|
| a. | ——— | 53/40-1 | 0.029 |
| b. | — — — | 60/40 | 0.036 |
| c. | —·—· | 61/40 | 0.036 |
| d. | — — — | 64/40 | 0.039 |

Frequency, f (cps)

Nondimensional Frequency, $S = \dfrac{fD}{V}$

$\phi_n(f)$
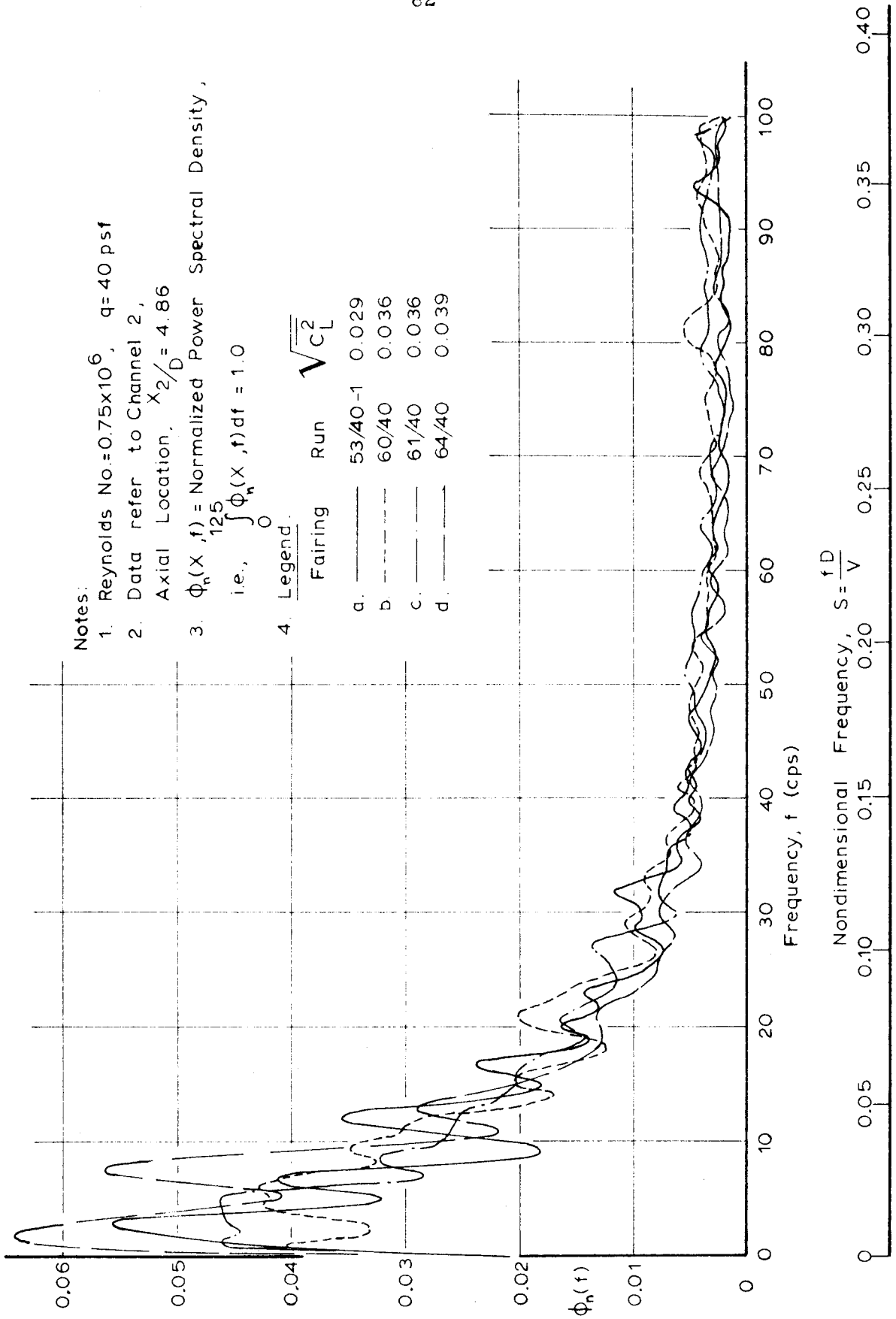
Figure 15    Ensemble of Power Spectrum for Lift Force
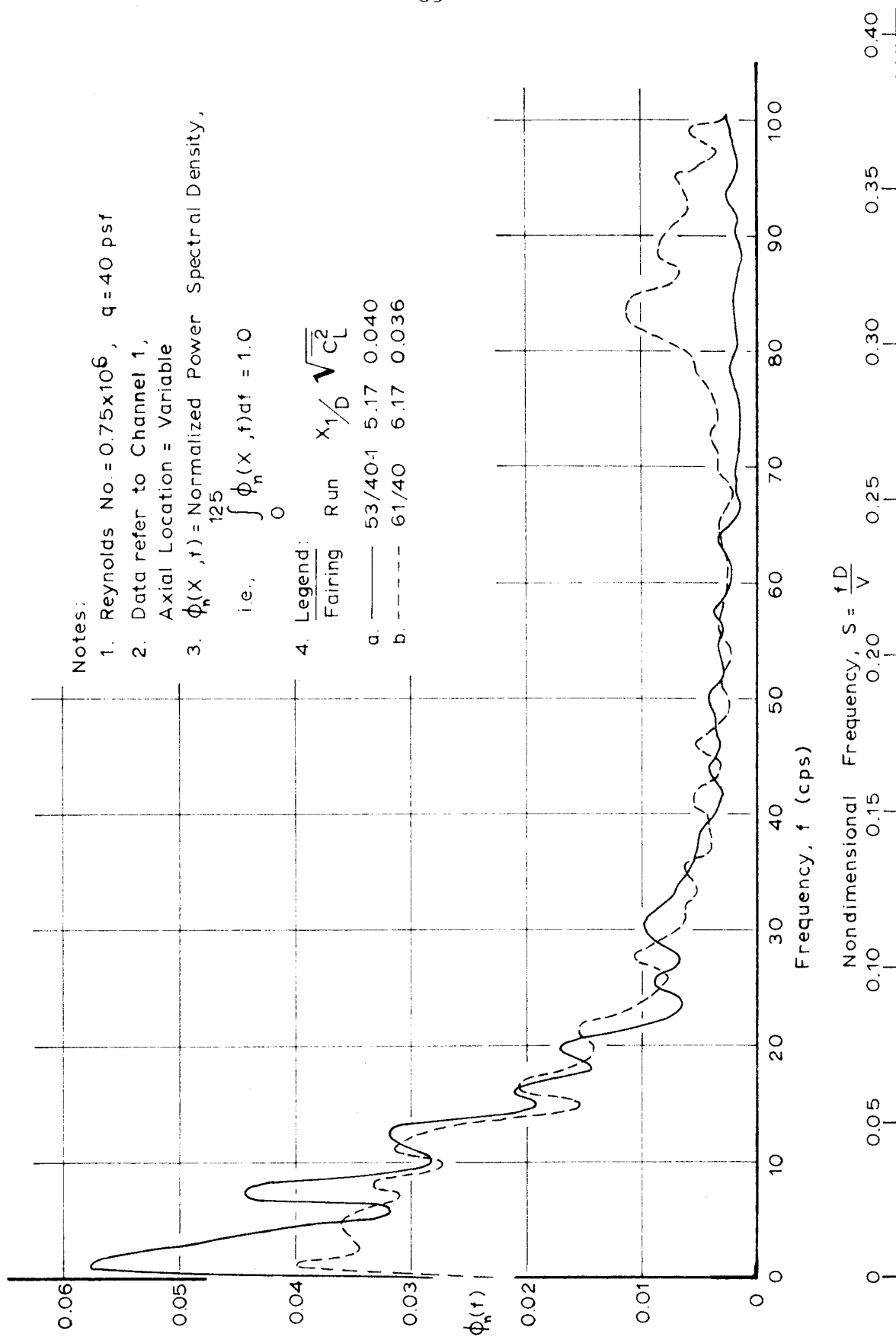
Figure 16    Effects of Axial Location upon Power
Spectrum of Lift Force
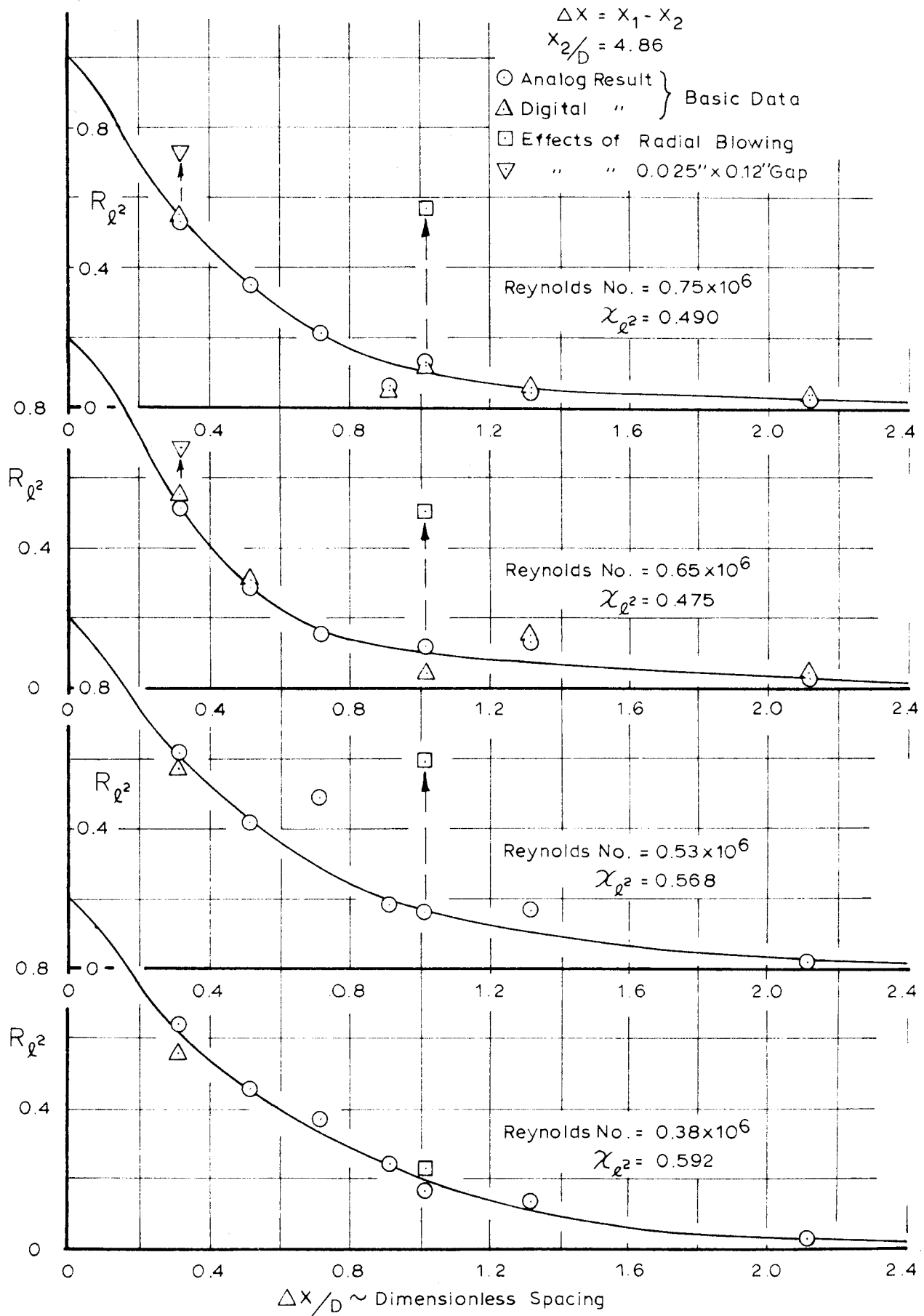
Figure 17    Correlation Coefficient for Lift Force
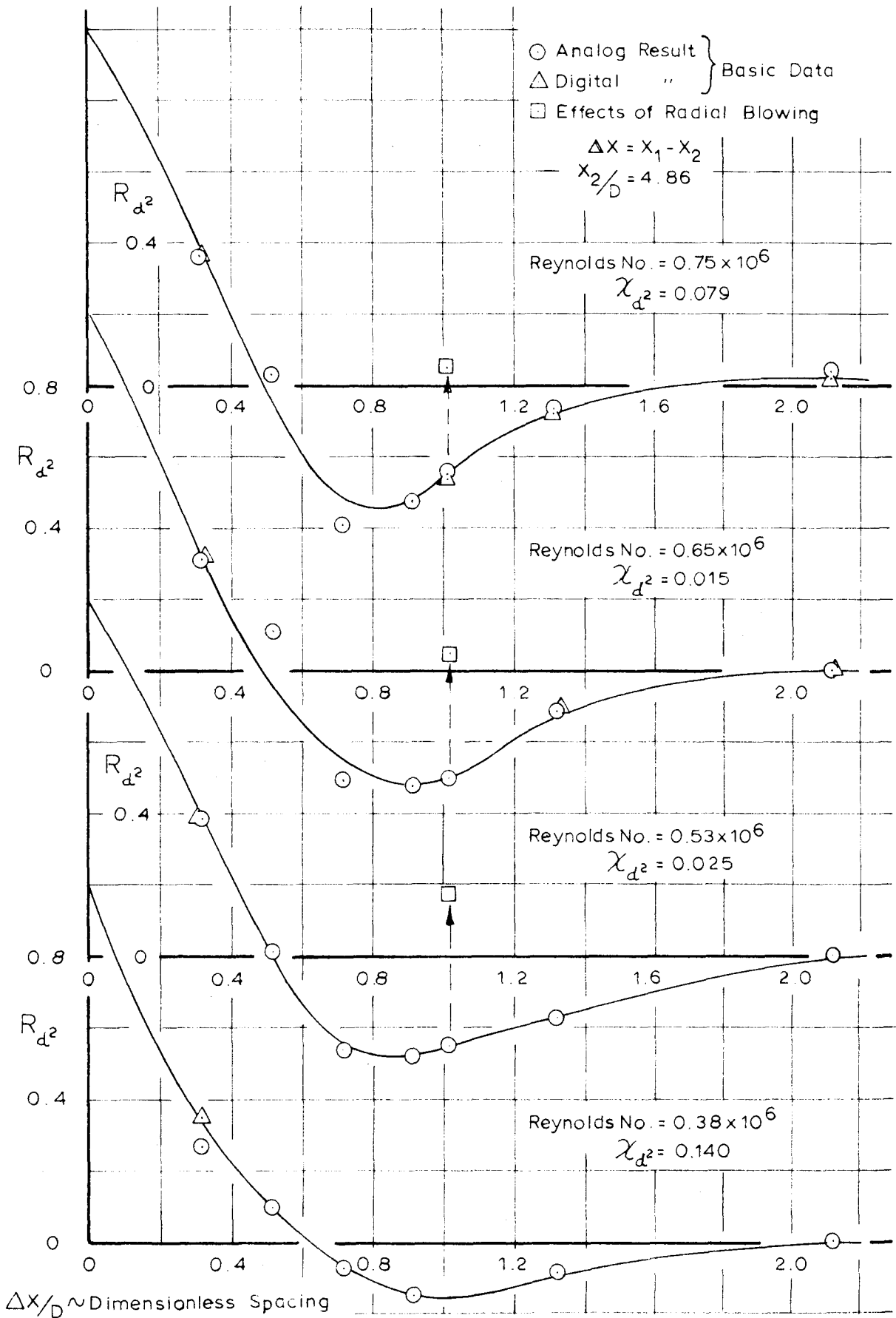
Figure 18   Correlation Coefficient for Drag Force
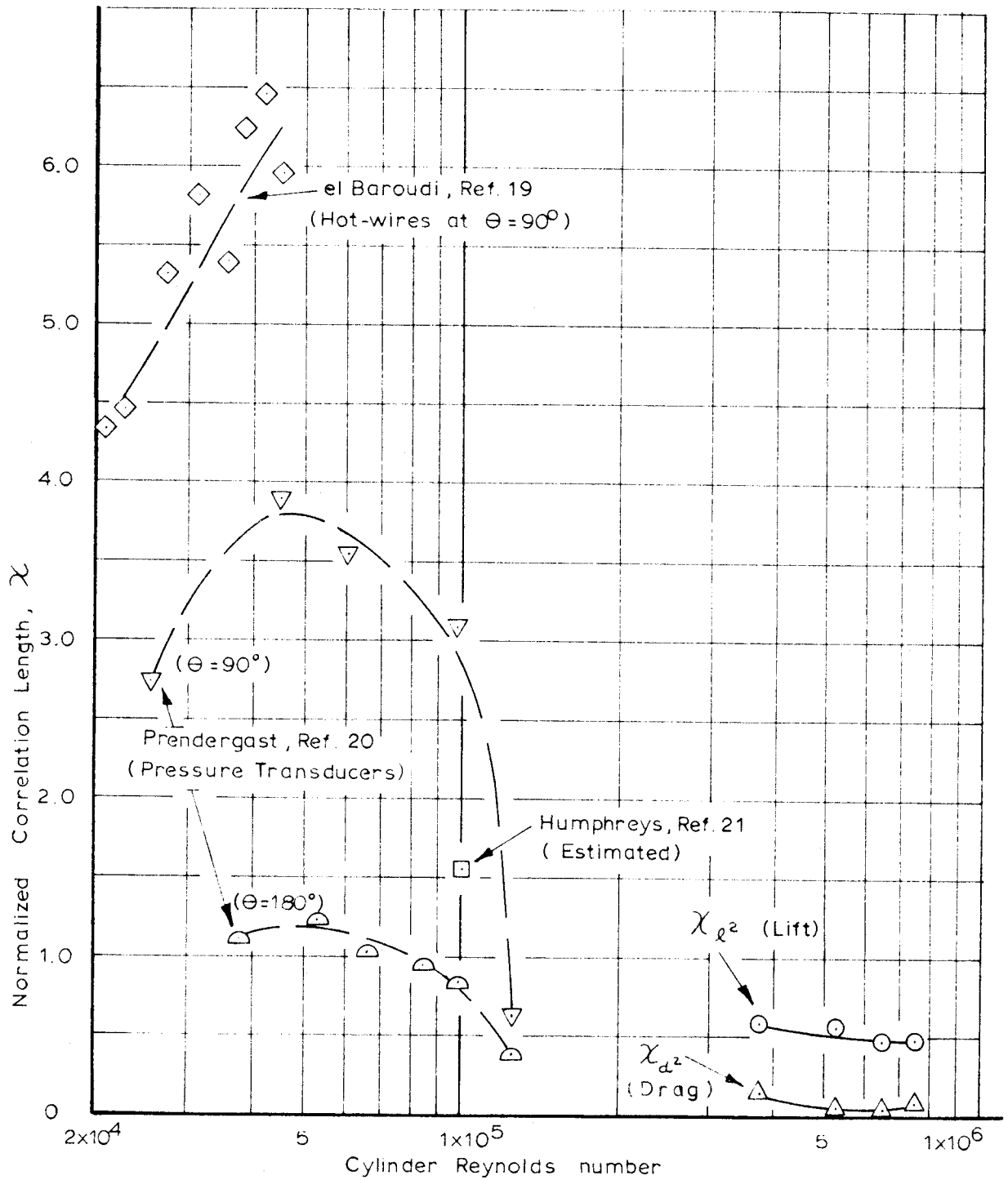
Note: Correlation Length Normalized with respect
to Cylinder Diameter.

Figure 19      Correlation  Length  Summary
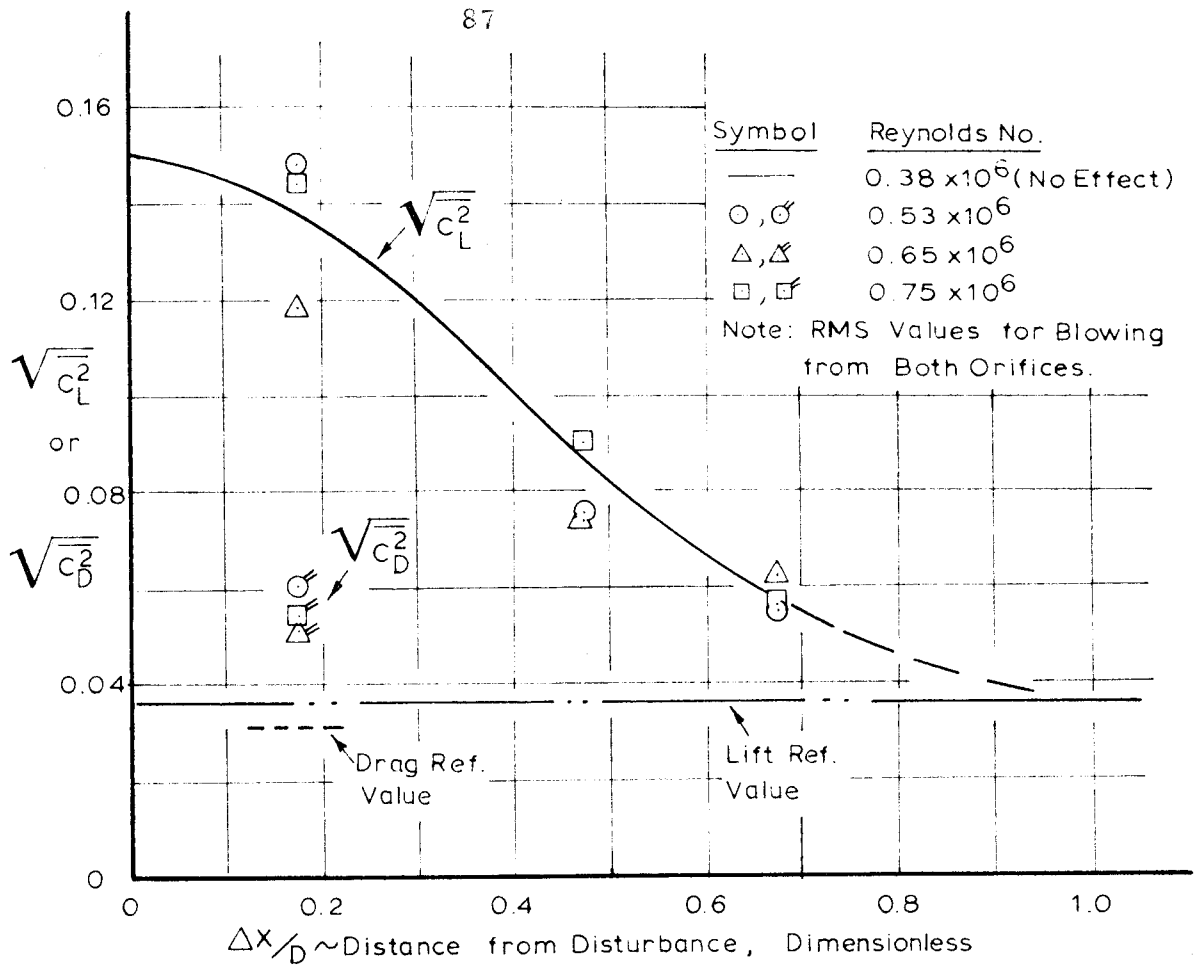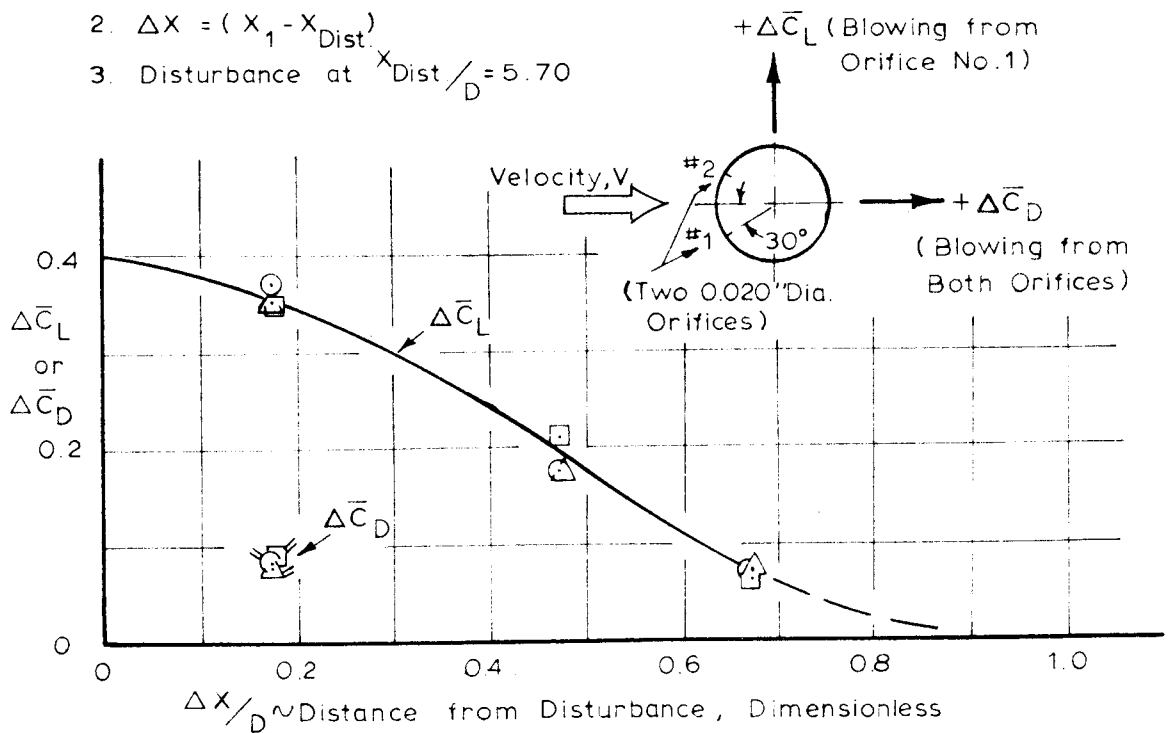
Figure 20    Summary of Orifice Blowing Effects
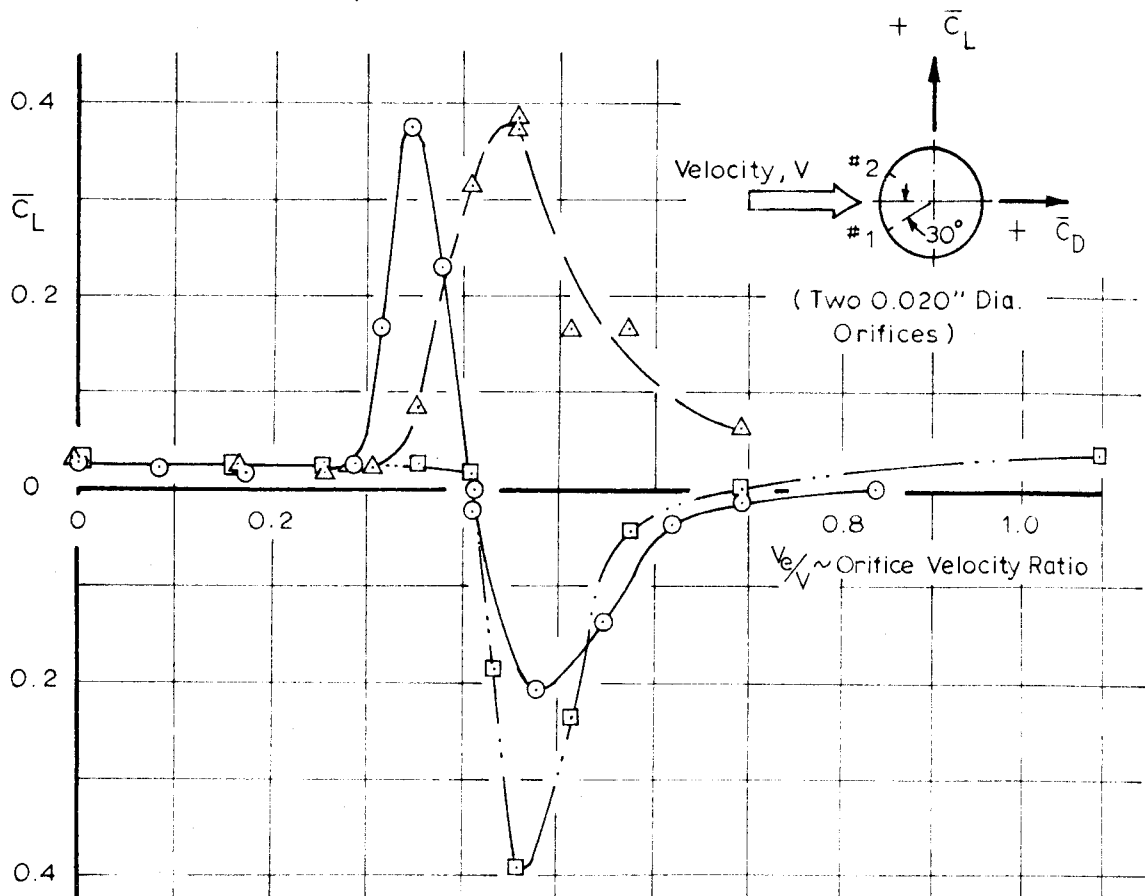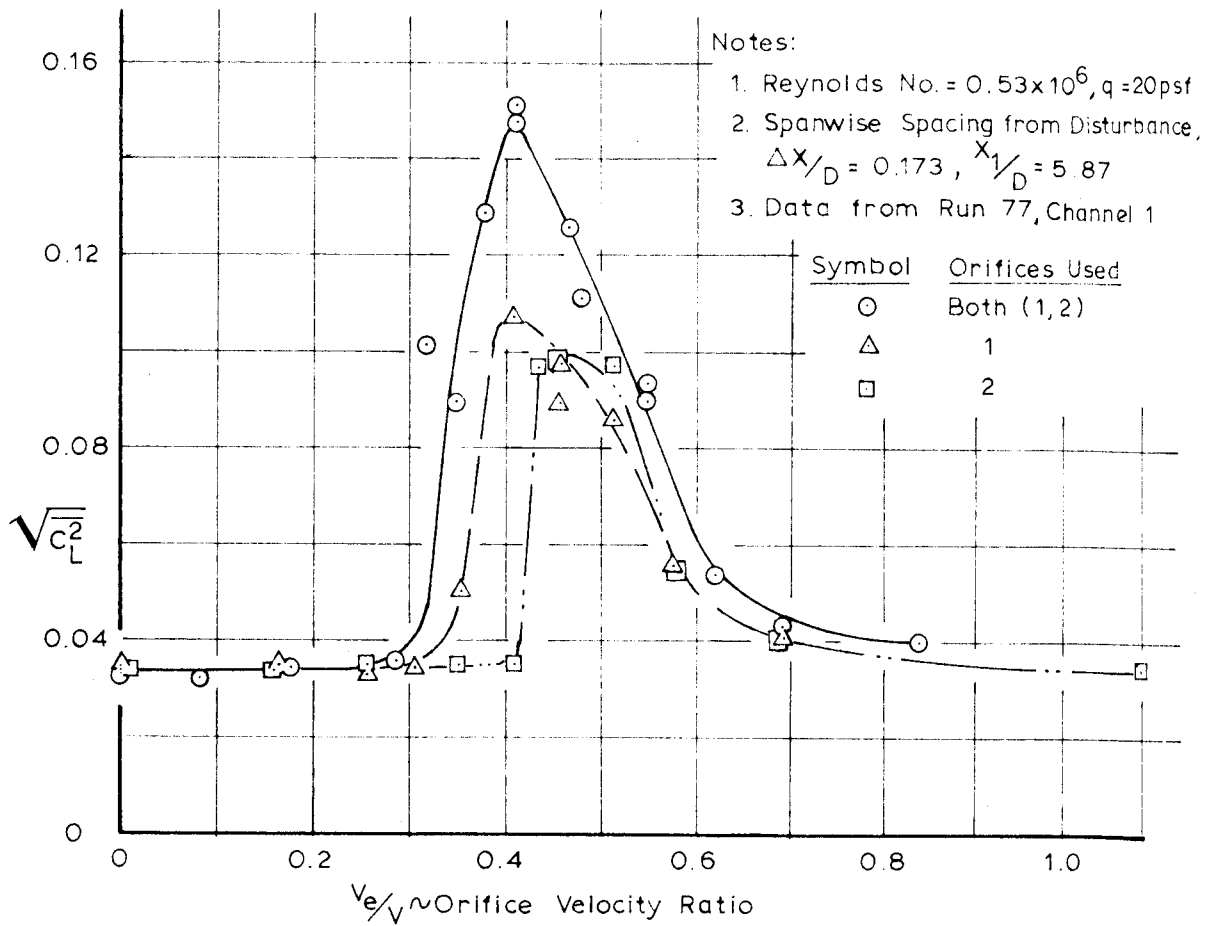
Figure 21    Effects of Orifice Blowing upon Lift    Force

89
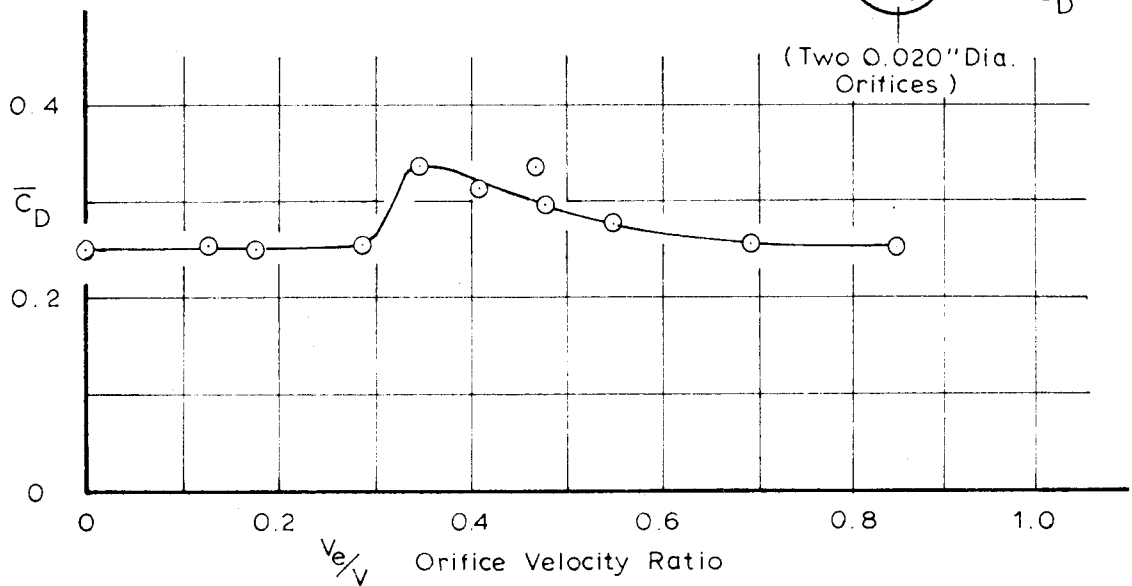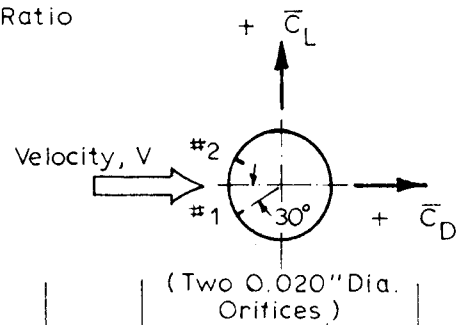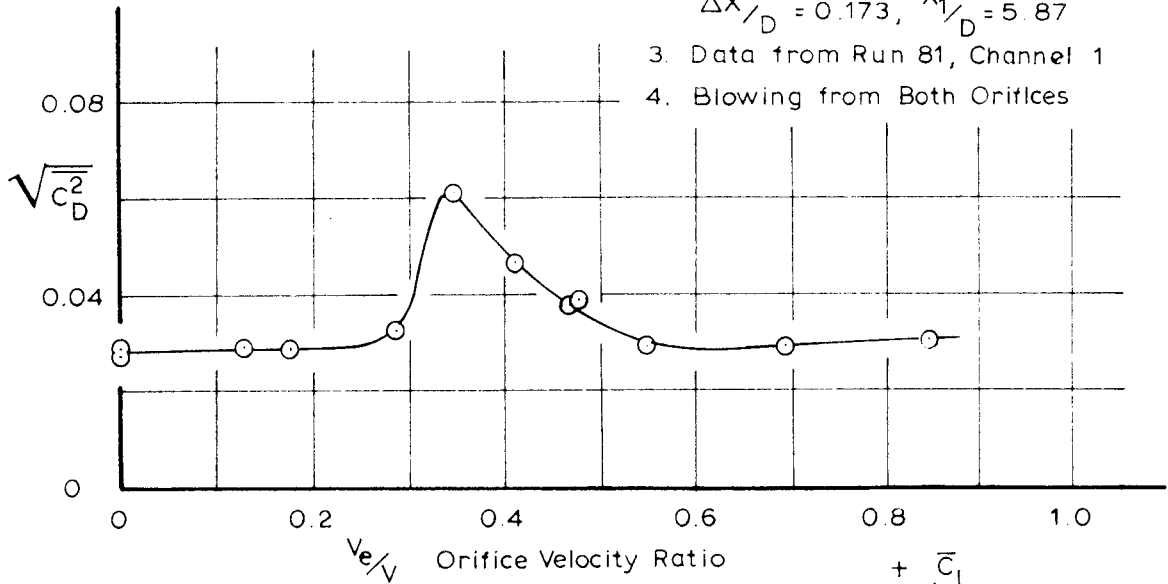


Figure 22   Effects of Orifice Blowing upon Drag Force
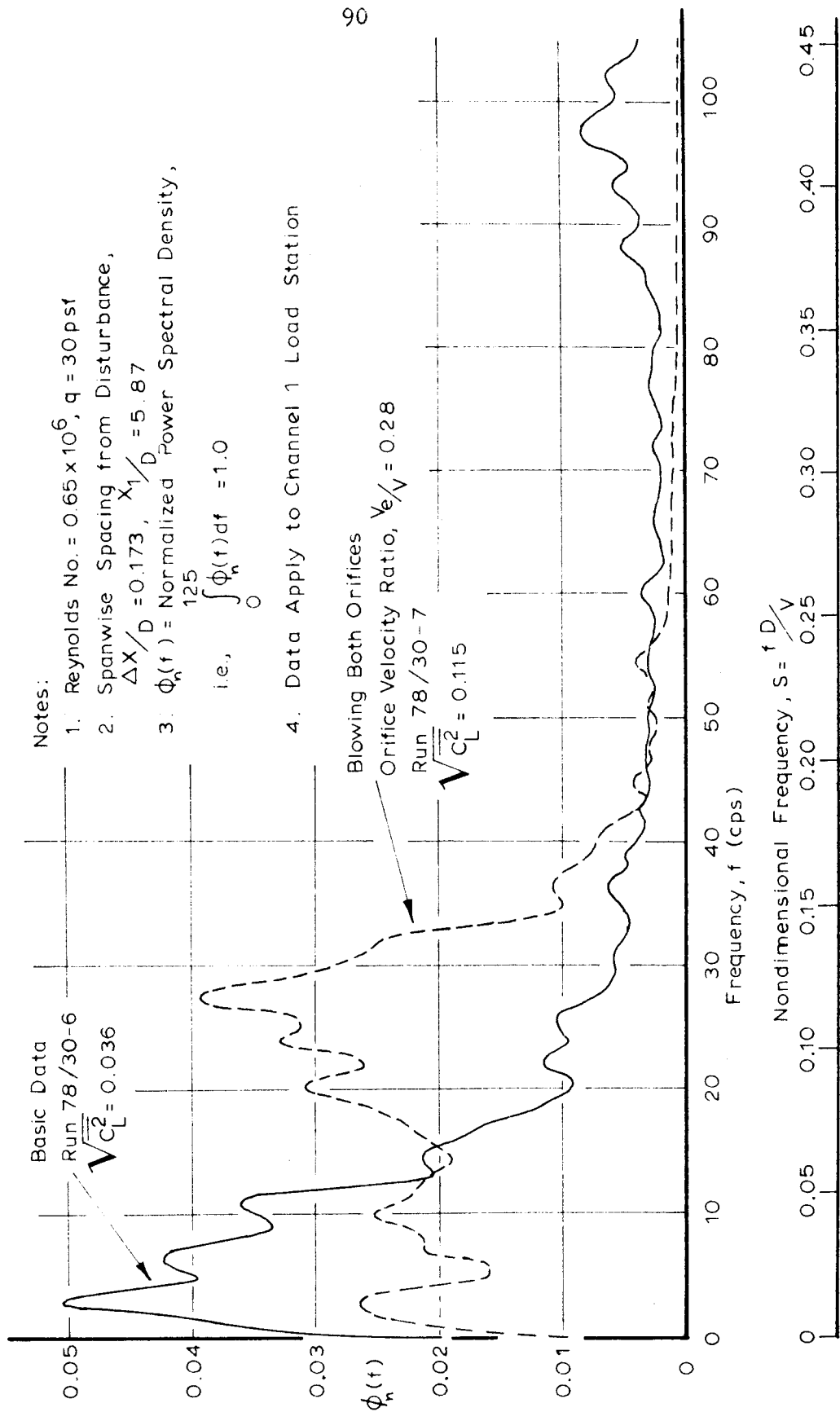
Figure 23    Effects of Orifice Blowing upon Power Spectrum
of Lift  Force ,        Reynolds No.= $0.65\times10^6$

91
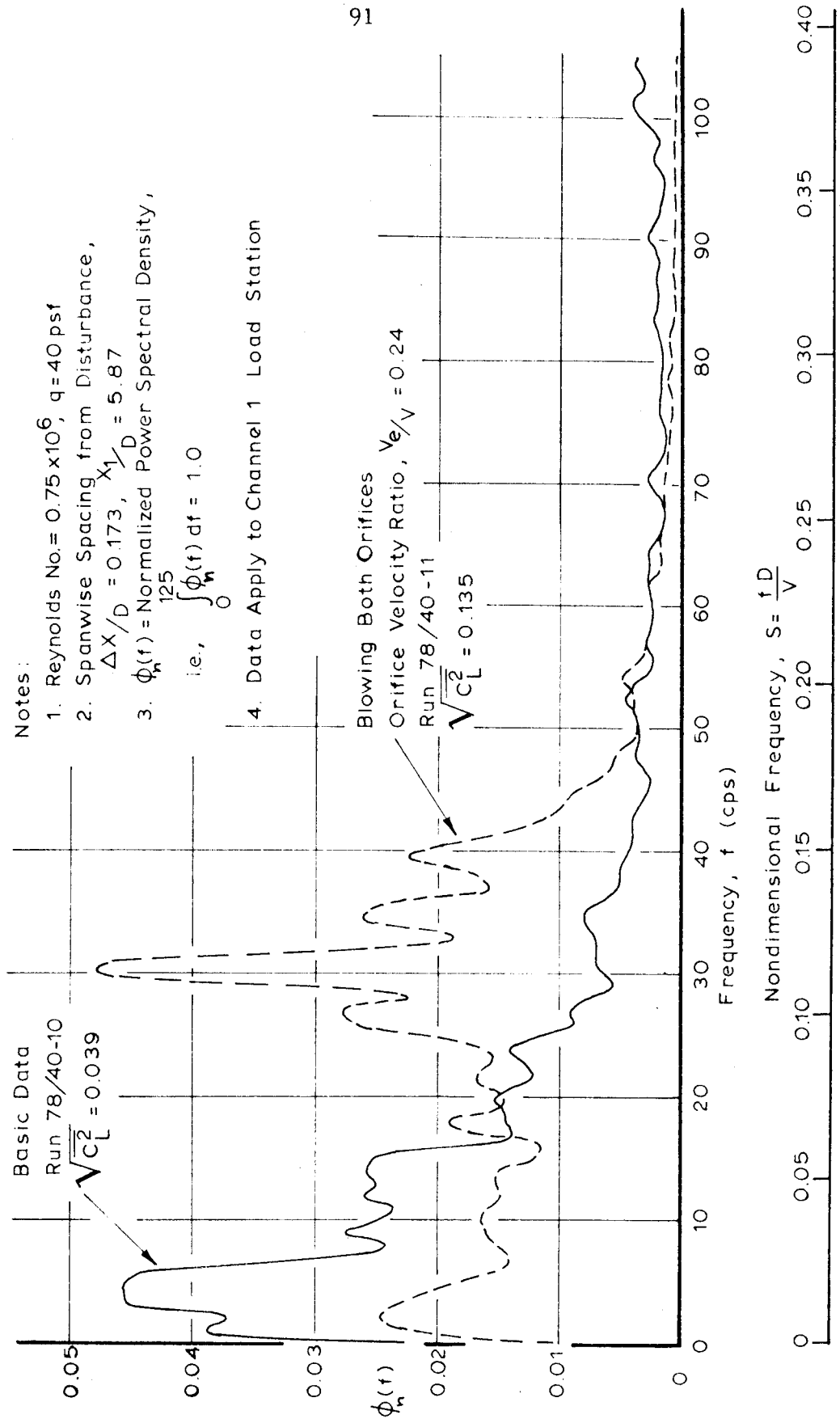


Figure 24    Effects of Orifice Blowing upon Power Spectrum
of Lift Force, Reynolds No. = 0.75 × 10⁶
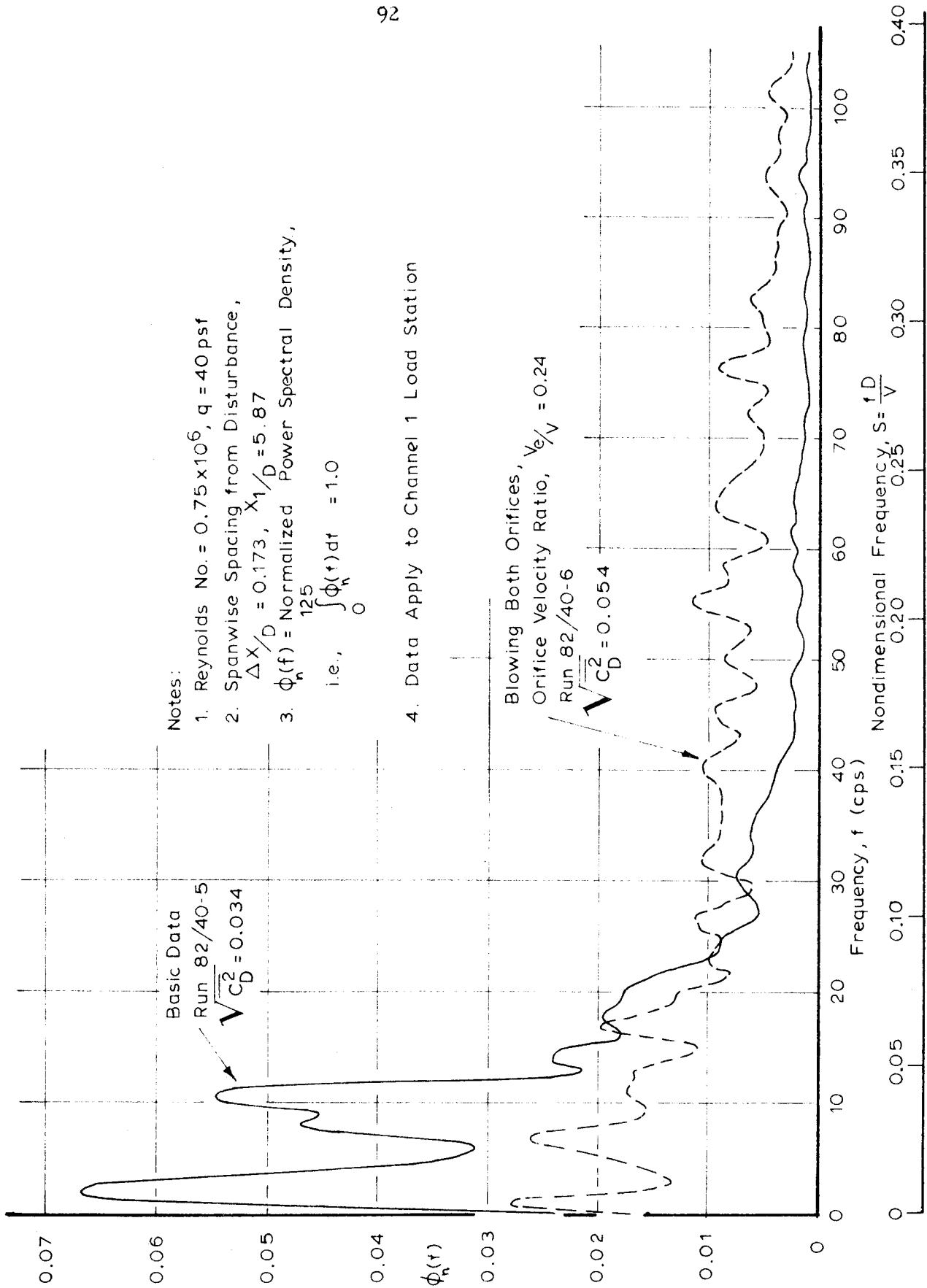
Figure 25    Effects of Orifice Blowing upon Power Spectrum of Drag Force,    Reynolds No. = $0.75 \times 10^6$
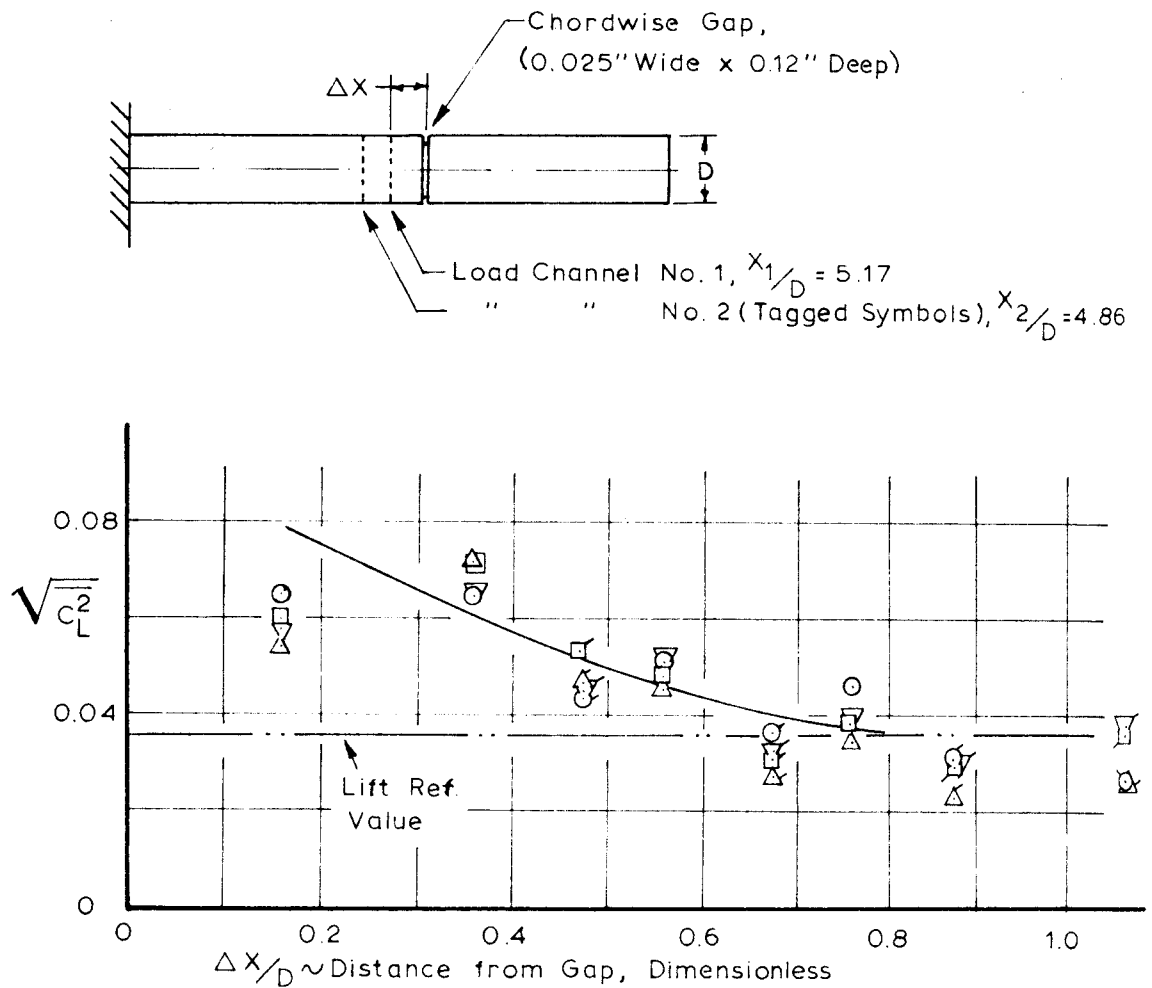
Figure 26    Effects of Chordwise Gap upon Lift    Force
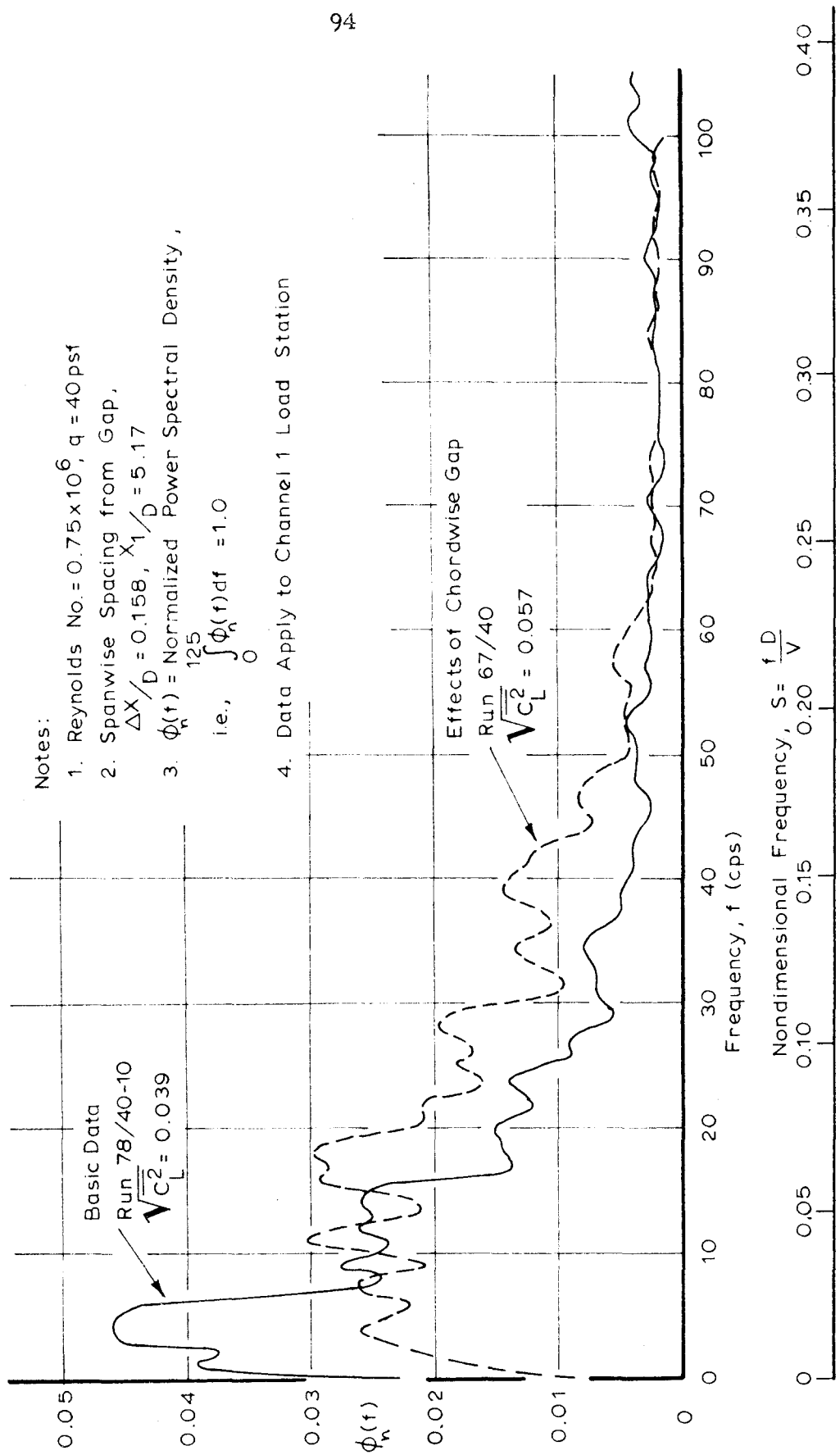
Figure 27 Effects of Chordwise Gap upon Power Spectrum
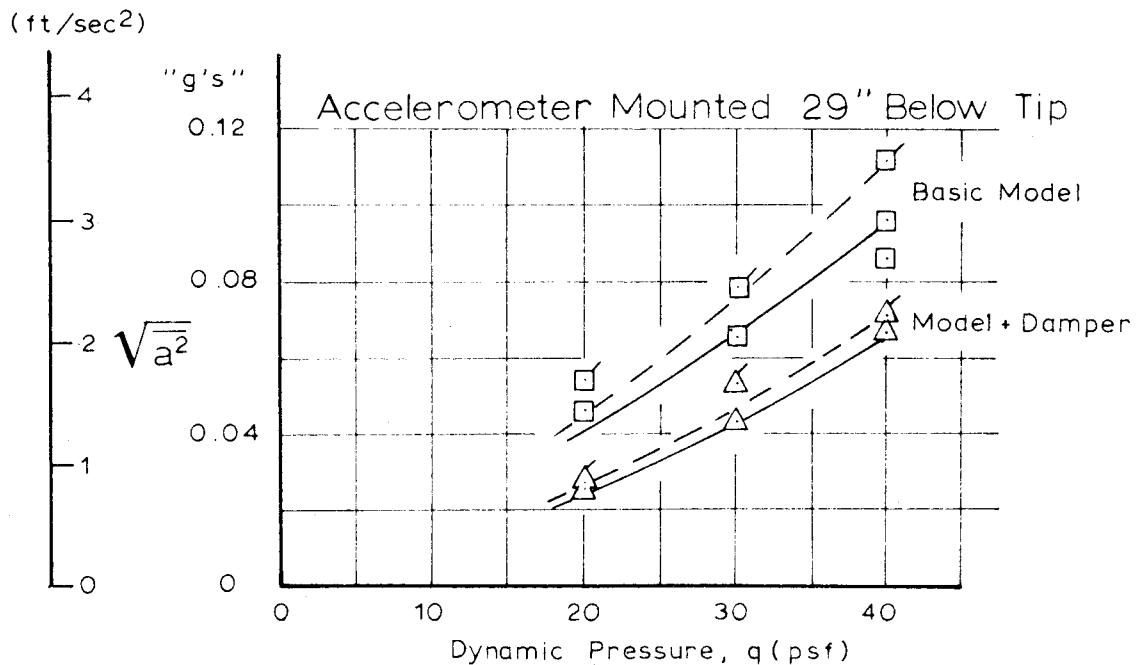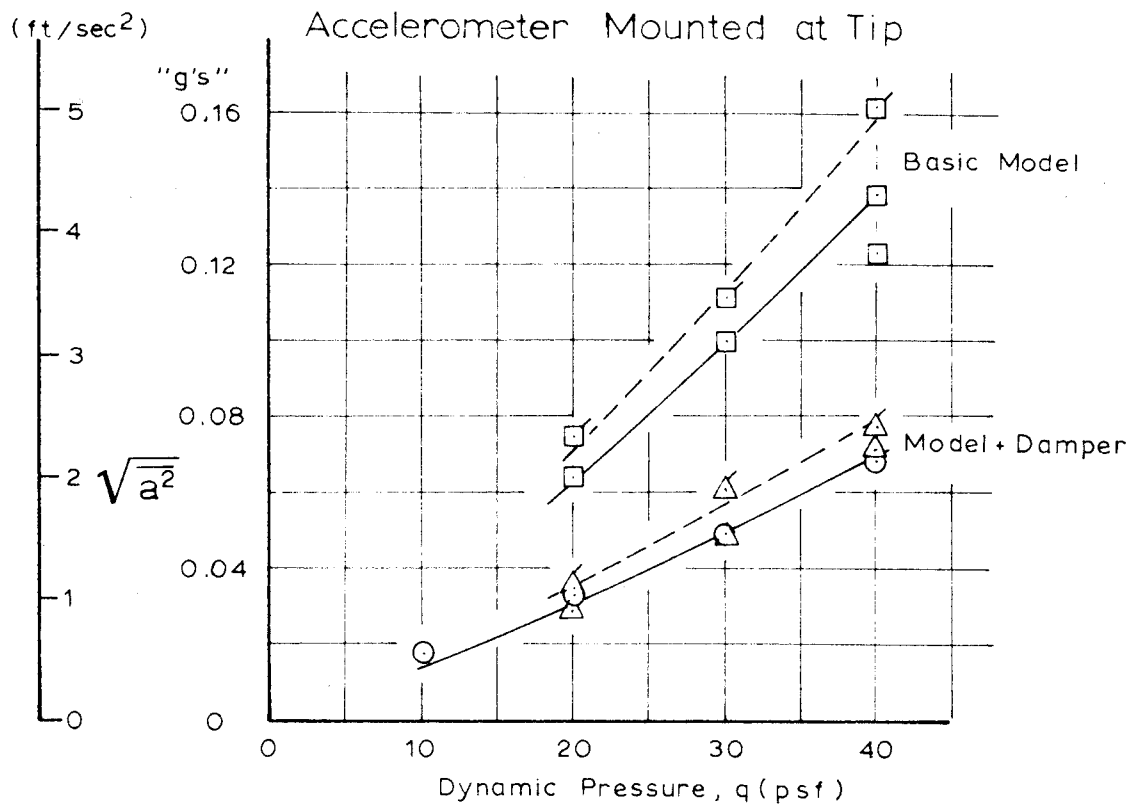
Figure 28    Model Acceleration, Lateral Direction
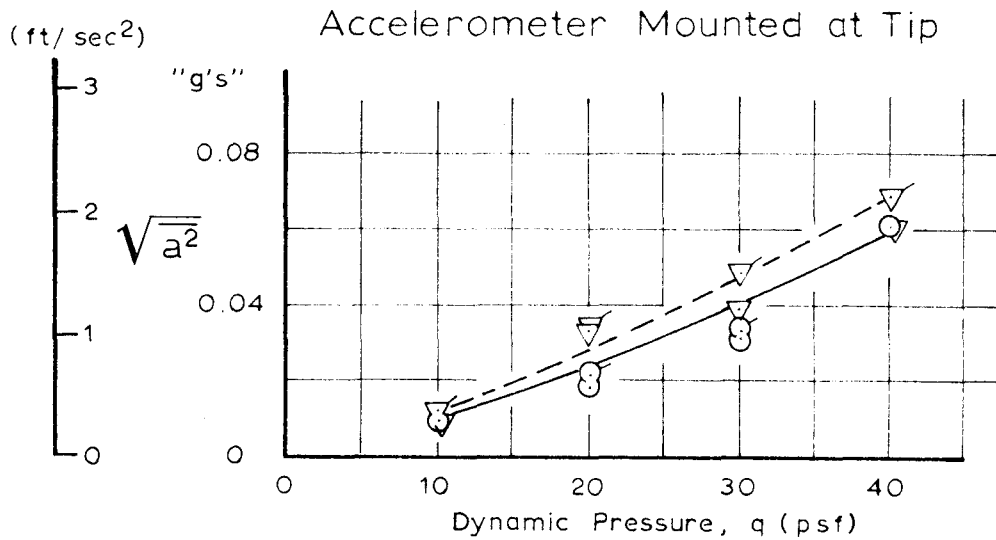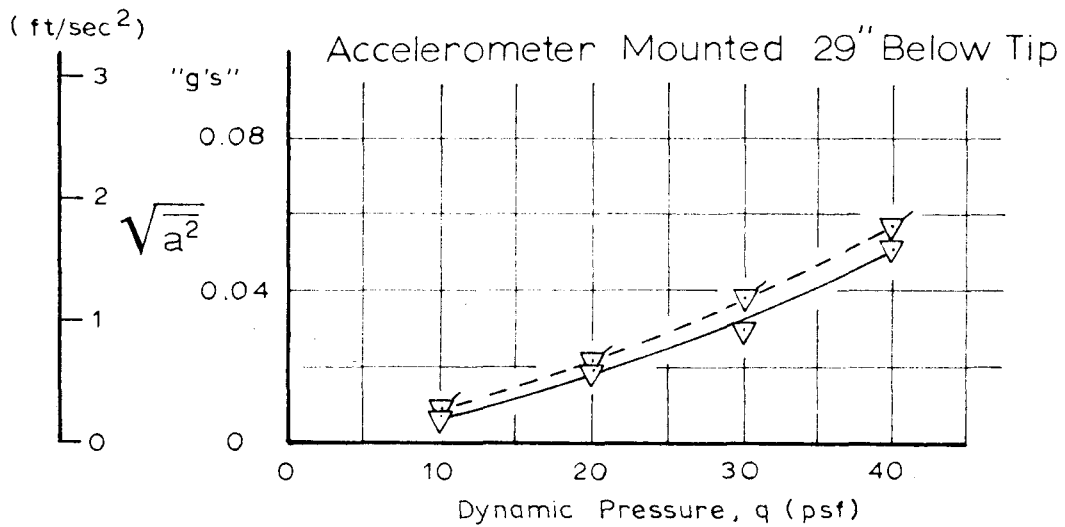
Figure 29    Model Acceleration, Longitudinal Direction
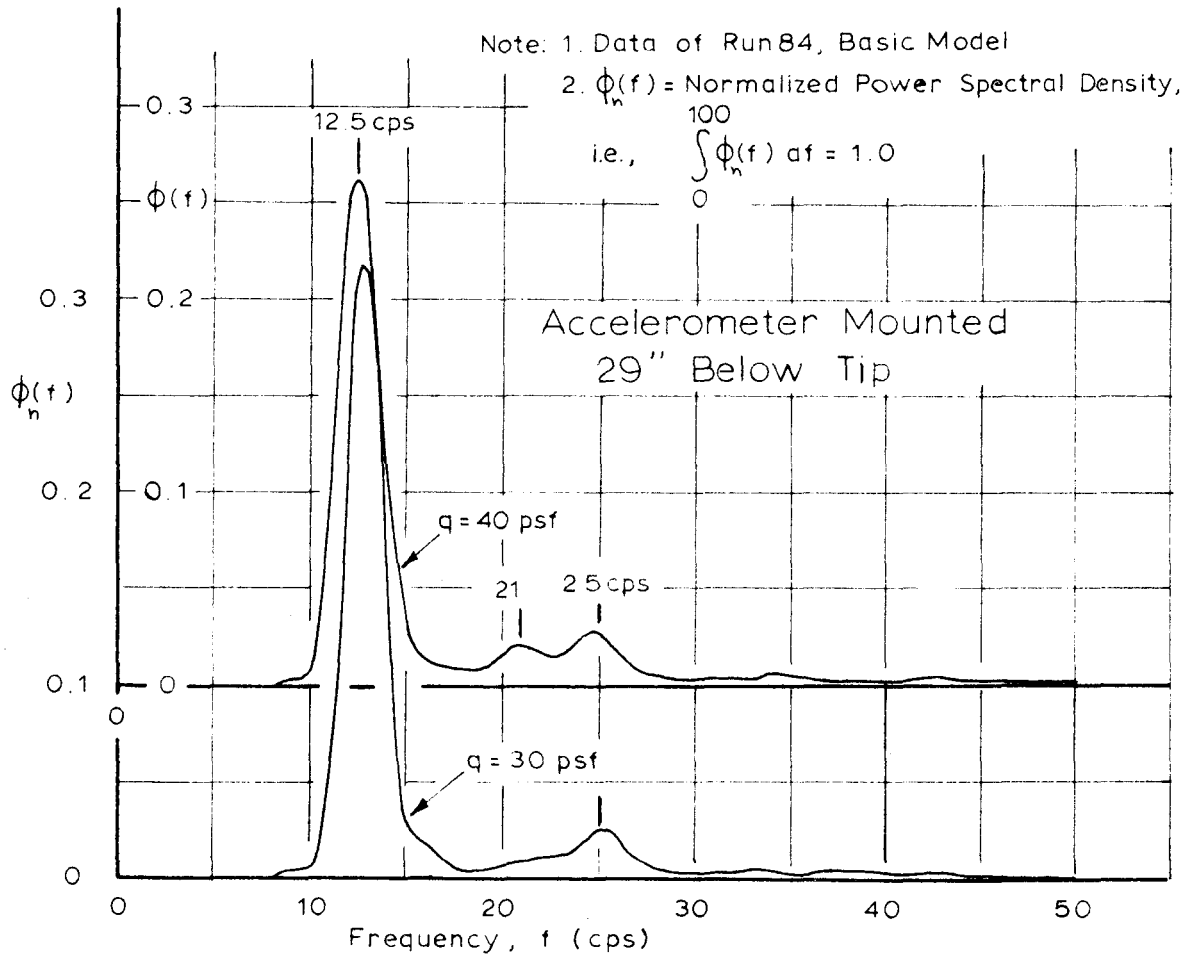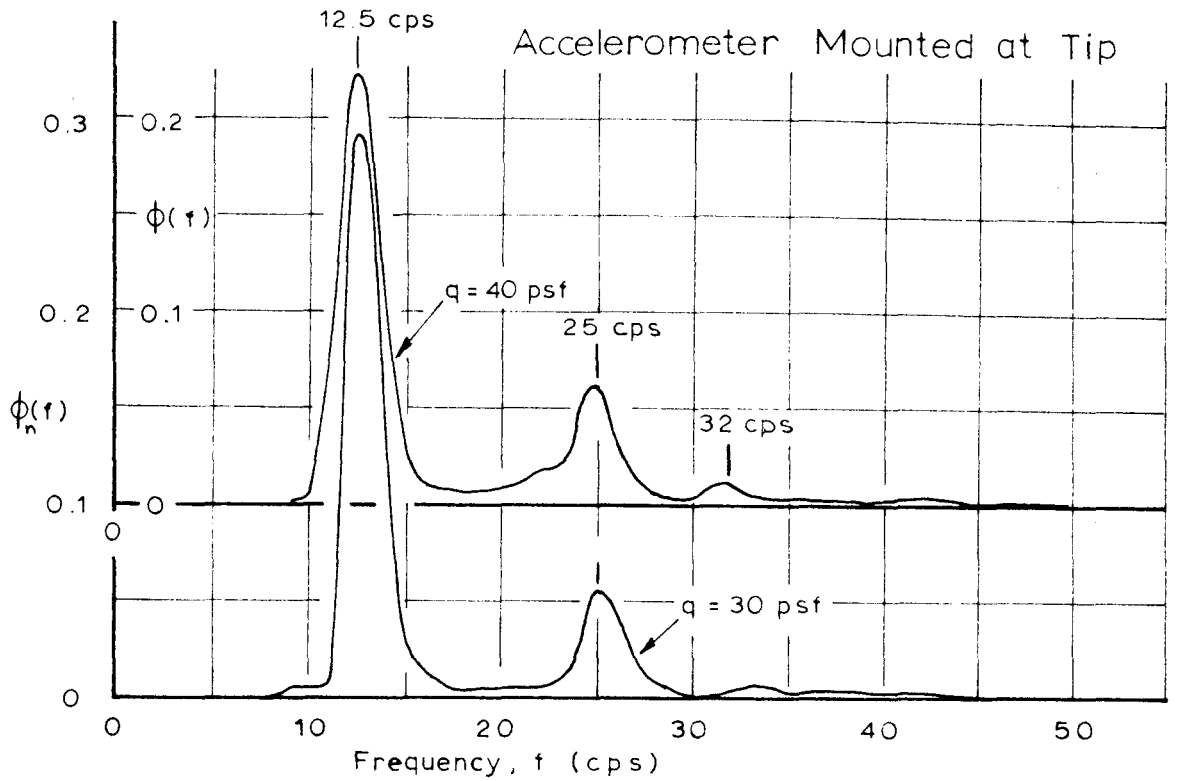
Figure 30    Power Spectrum of Lateral Acceleration
            Basic Model
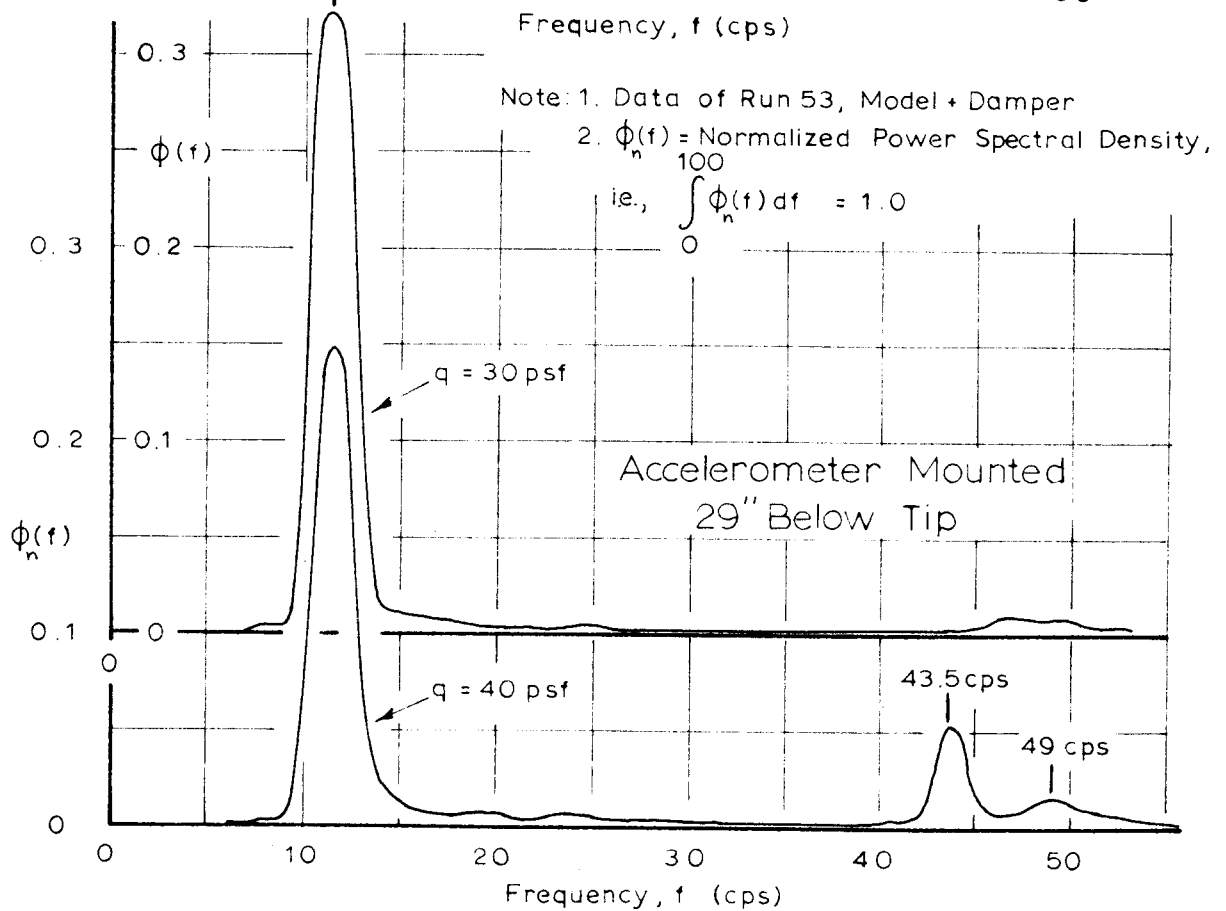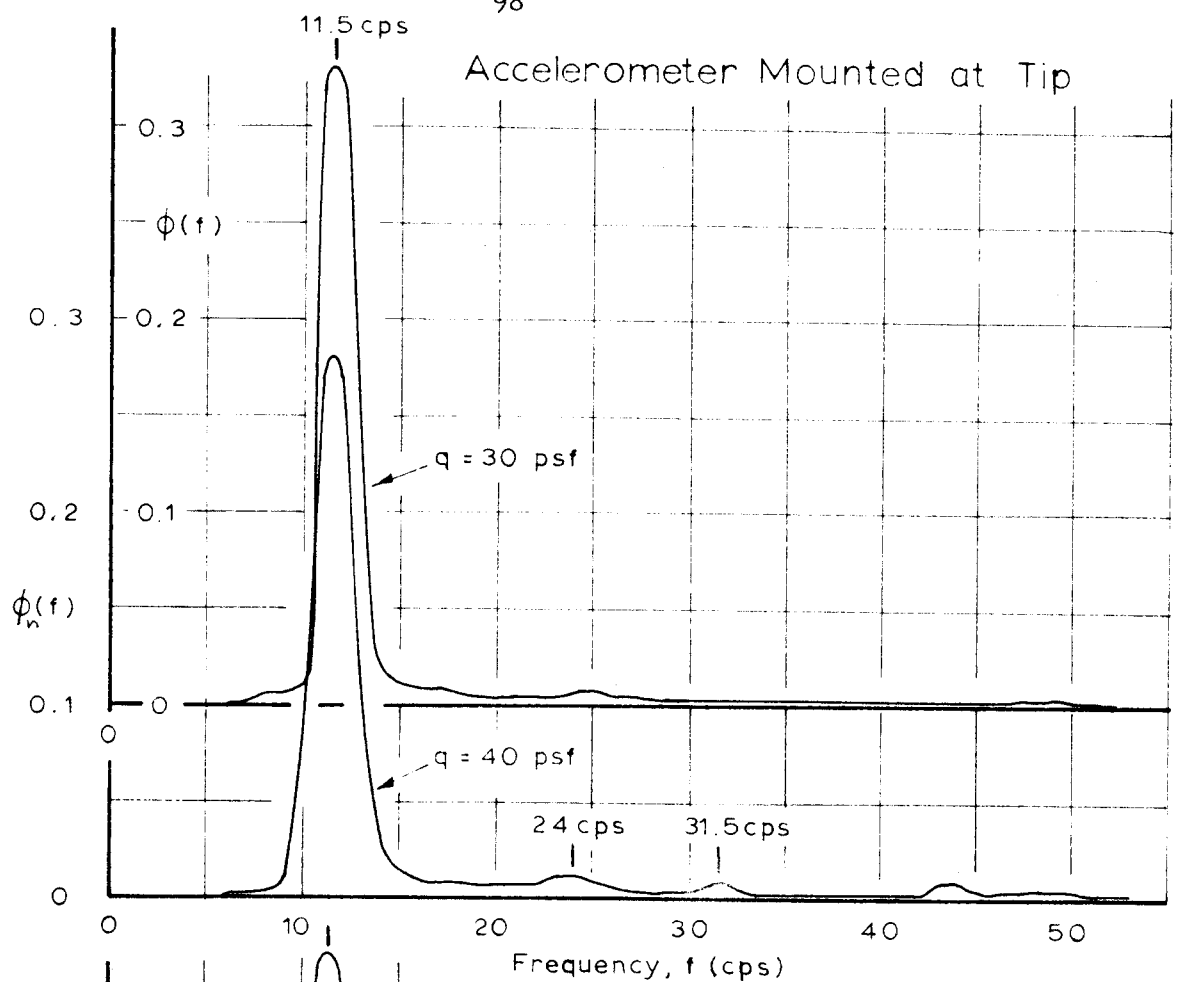
Figure 31    Power Spectrum of Lateral Acceleration ,
Model + Damper

Orifice : 0.025"x 0.25"

1/8" Plexiglas Spacer, Hole = 3/32" Dia.

Cavity Spacer Washer,
0.005"x 0.75" I.D.

Outer Seal, O-Ring

0.020" Thick Washer

Cast Devcon Sleeve,
(80% Aluminum, 20% Epoxy Resin)

Gland Nut — Tighten with
Spanner Wrench.

Clamp Ring — Locks Coil Holder with
respect to the Membrane.

Membrane Holder — 0.004" Thick Membrane
Sweat Soldered on Inner End.

Section View of
Pressure Orifice
and Transducer

Coil and Ferrite Cup Core

Coil Leads

Micarta Terminal Board

Inner Seal, O-Ring

Epoxy Resin Seal

Pressure Tubing — Vents to Back Side
of the Membrane.

Coil Leads

Quarter Section
of Coil Holder

Note: Coil is Positioned near Membrane using Electrical Measurements
to Adjust Nominal 0.006" Air Gap.

Figure A.1    Sketch of  Pressure Orifice &  Transducer
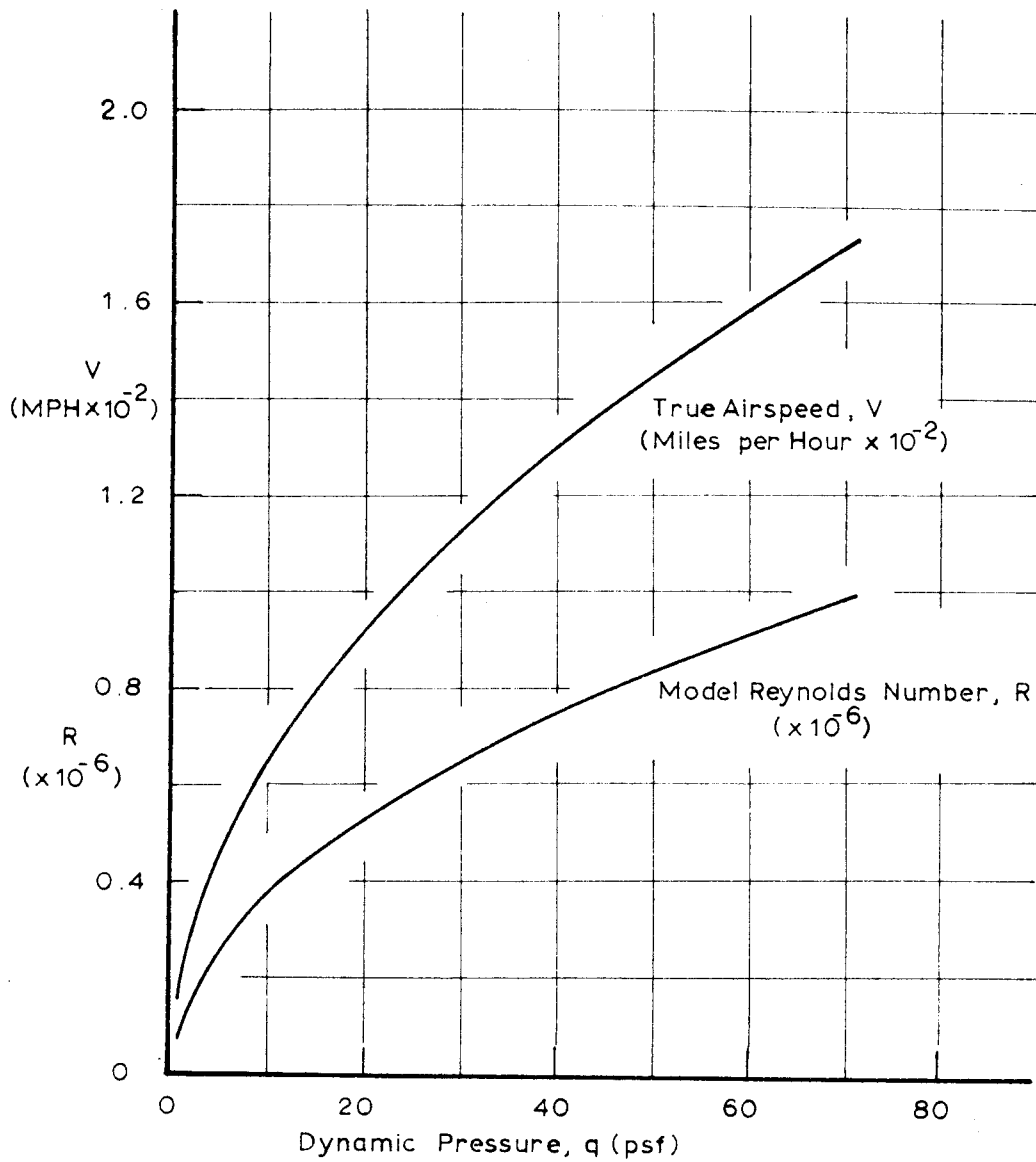
Figure A.2   Average Tunnel Operating Characteristics
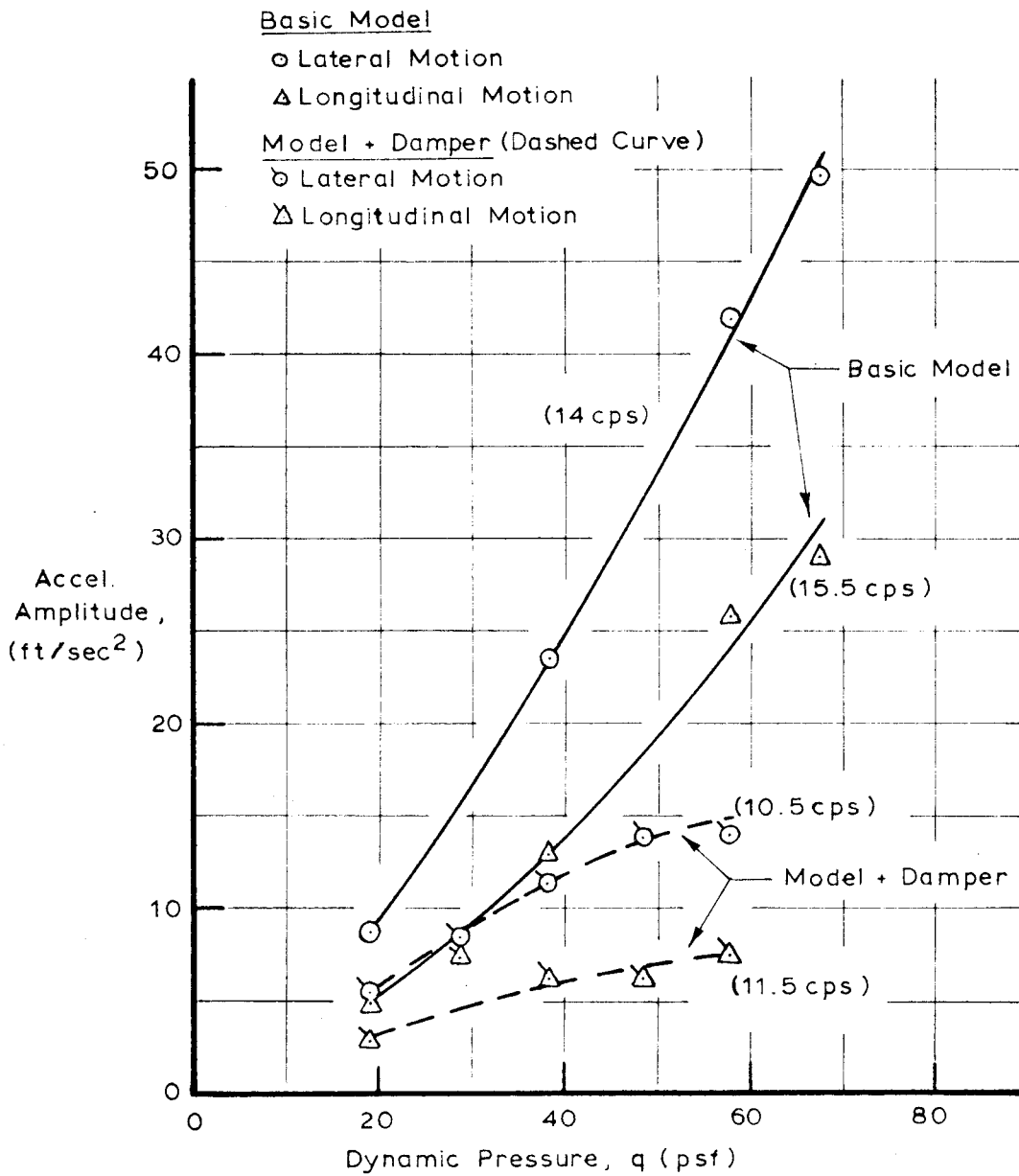
Figure A.3    Model Accelerations at Tip
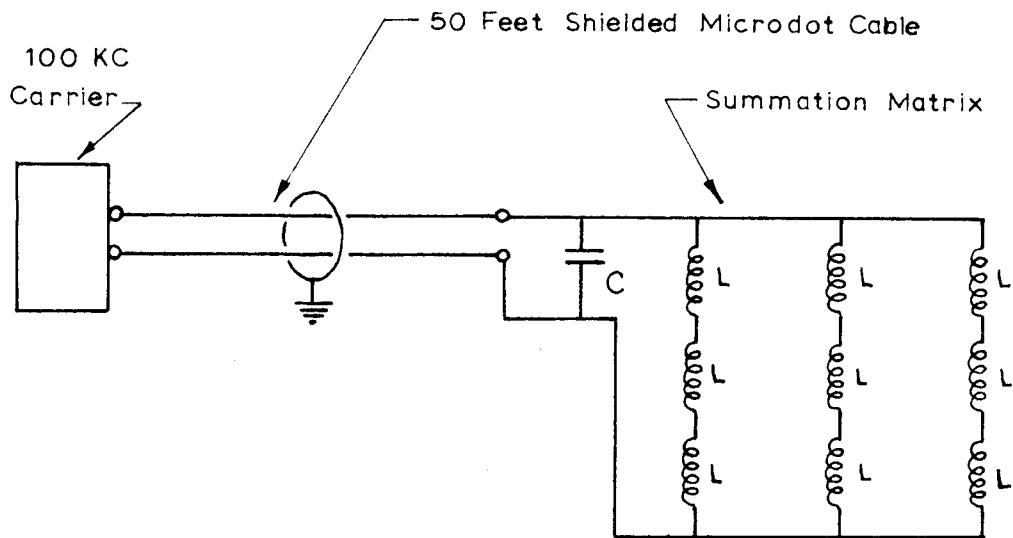
L = Coil inside Ferrite Cup-core, Inductance Value
    when Coil is near to Pressure Transducer
    Diaphragm $\cong 150 \times 10^{-6}$ Henries

C = Trimming Capacitor,
    Capacitance Value $\cong 1.0 \times 10^{-8}$ Farads

Note: Each Coil Represents a Single Pressure Transducer

Figure A.4    Pressure Transducer Summation Matrix

Figure A.5    Pressure  Orifice  Orientation
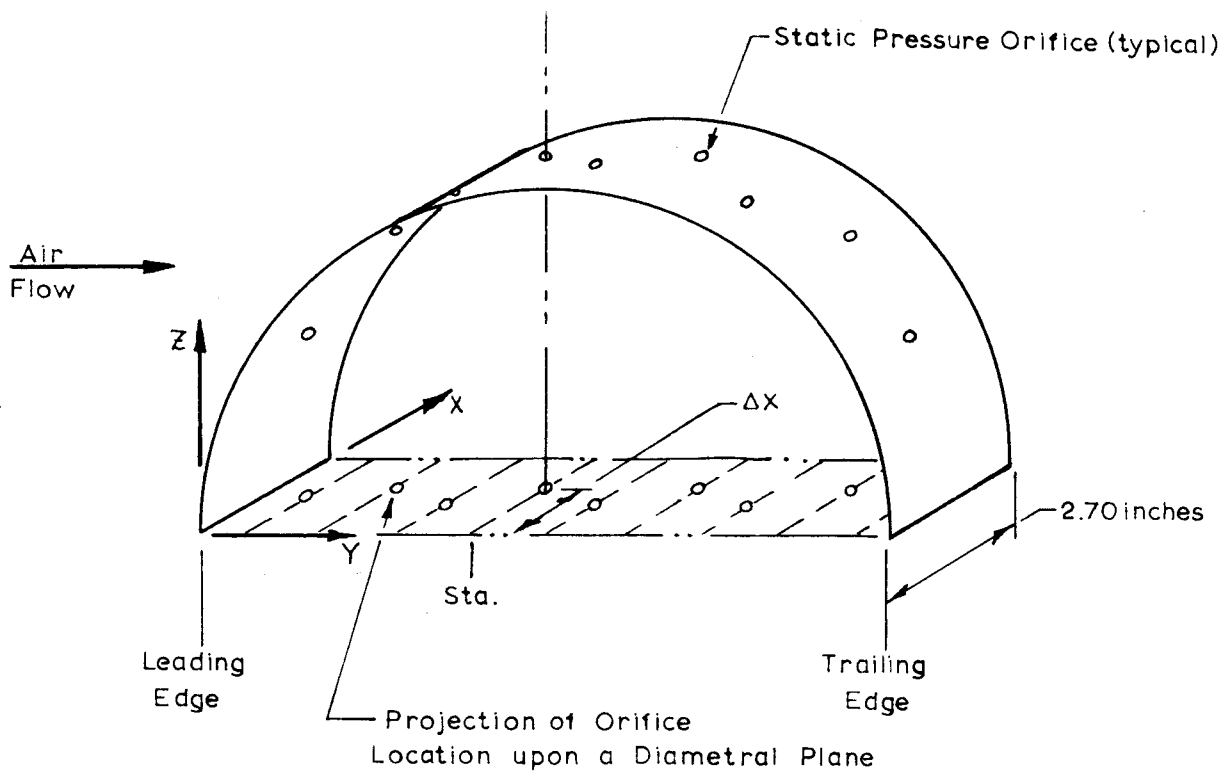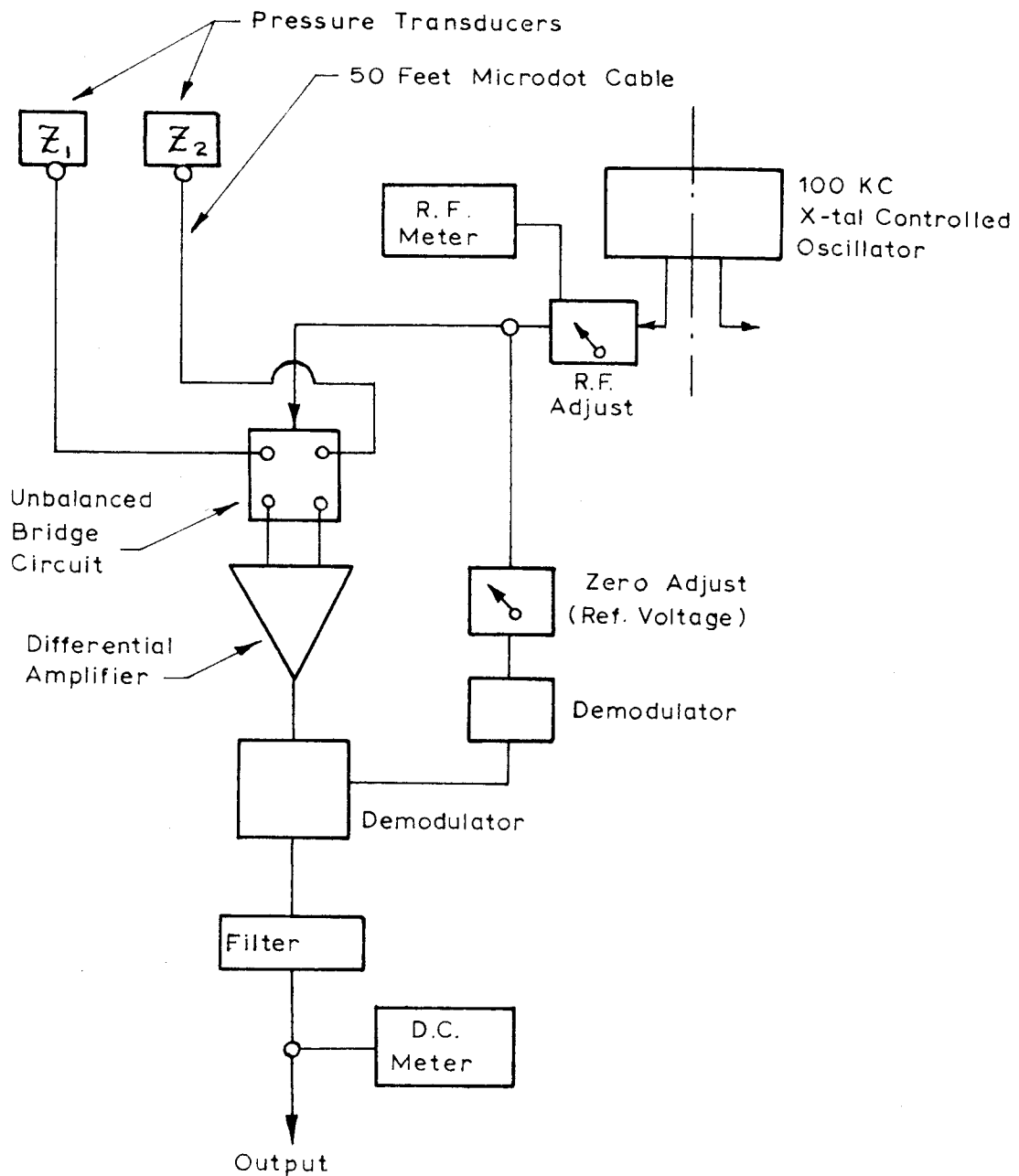
| Station | Y/D | $\Delta X$ (inches) | $\Delta R$ (inches) |
|---------|-------|------|--------|
| 1 | 0.056 | 1.55 | 0 |
| 2 | 0.167 | 1.24 | -0.20 |
| 3 | 0.278 | 1.35 | +0.20 |
| 4 | 0.389 | 1.74 | -0.20 |
| 5 | 0.500 | 1.35 | +0.20 |
| 6 | 0.611 | 1.74 | -0.20 |
| 7 | 0.722 | 1.35 | +0.20 |
| 8 | 0.833 | 1.74 | -0.20 |
| 9 | 0.944 | 1.55 | 0 |

Note : 1. Cylinder Diameter = D = 8.54 inches

2. $\Delta R$ = Relative Displacement (X-direction) of the Orifice with respect to Pressure Transducer Centerline

3. Only One Side of Instrumentation Sector Shown for sake of clarity.

4. Orientation Corresponds to  Lift  Mode.

Figure A.6    Block Diagram of Carrier Amplifier
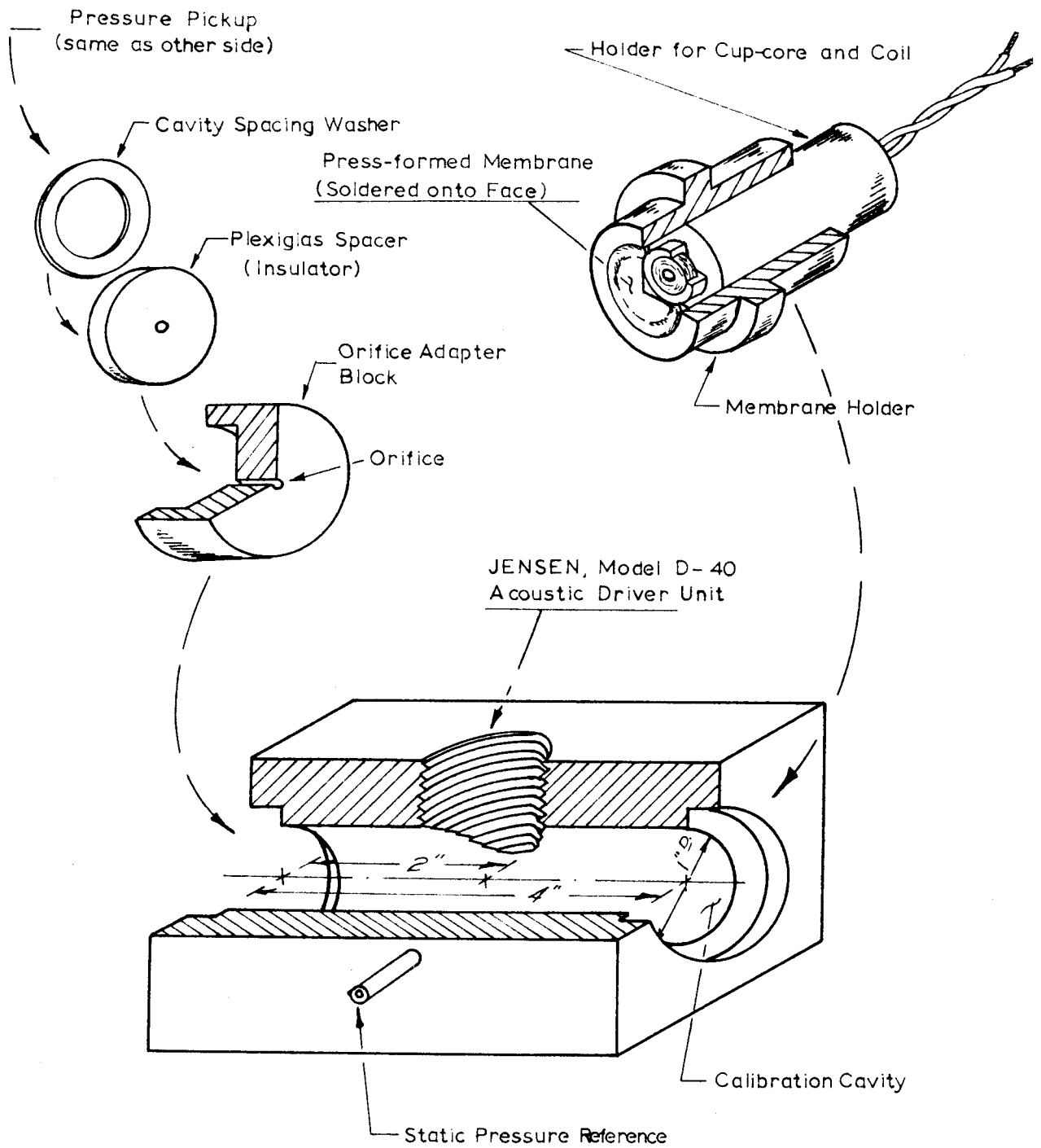
Figure A.7    Orifice Test—Experimental Setup
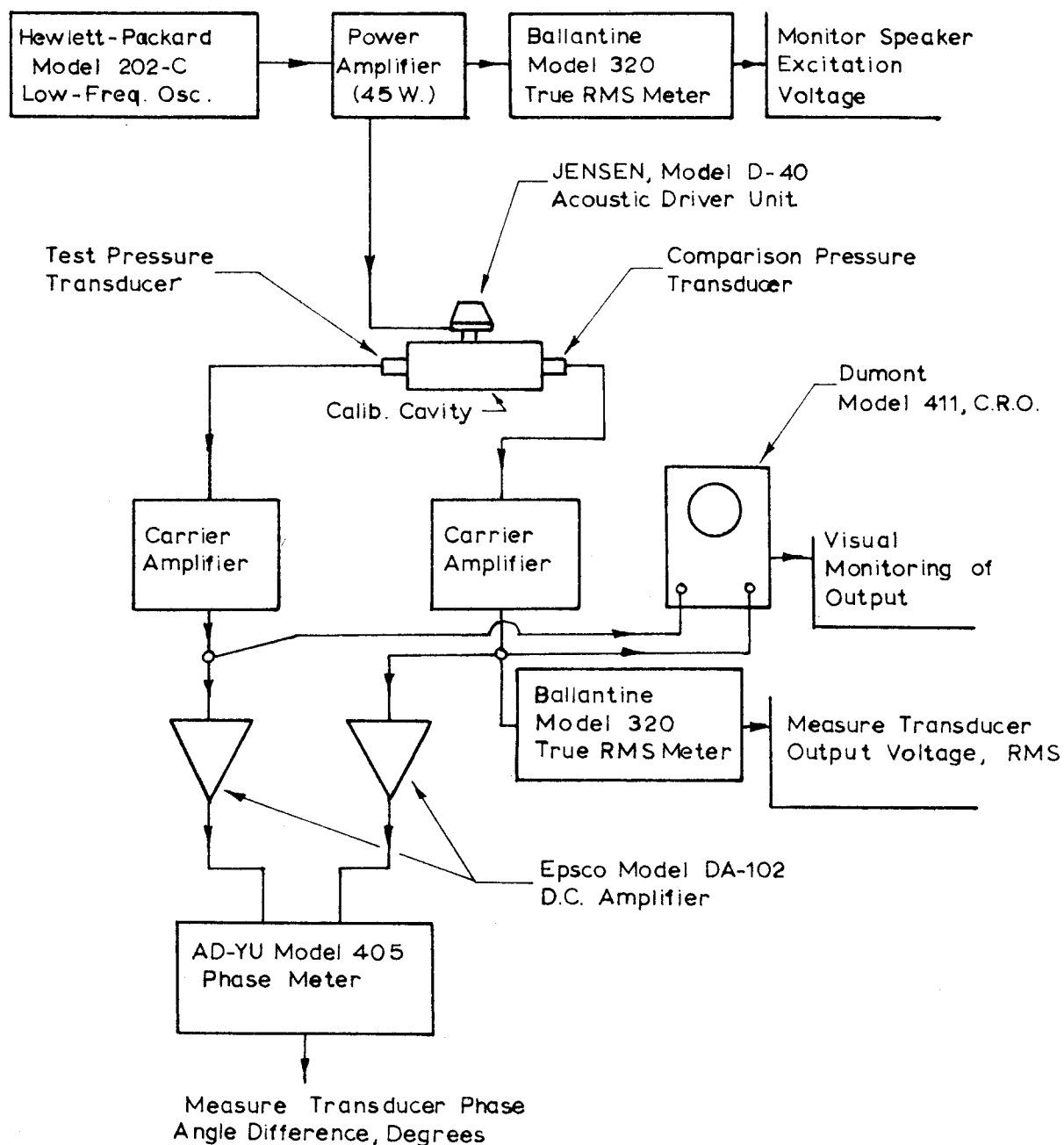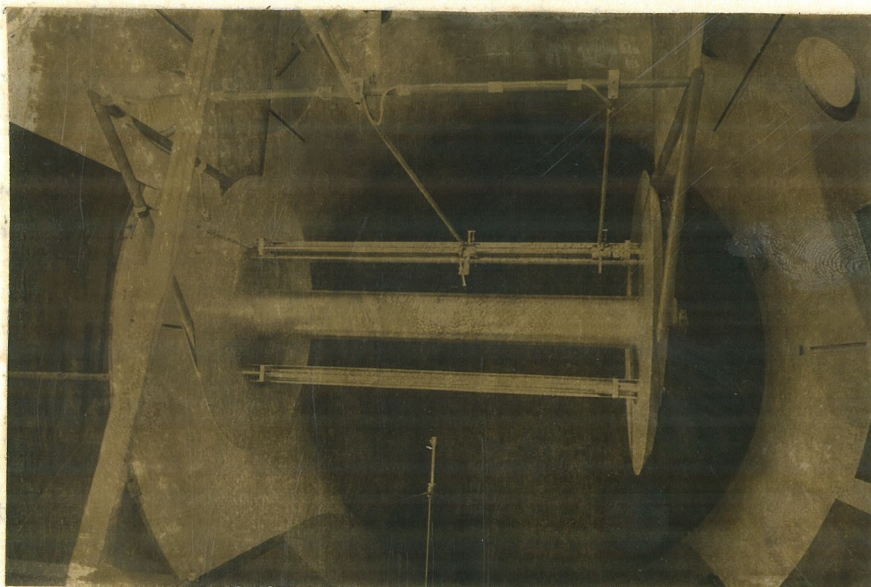
Figure A.8    Schematic of Orifice Calibration Circuitry
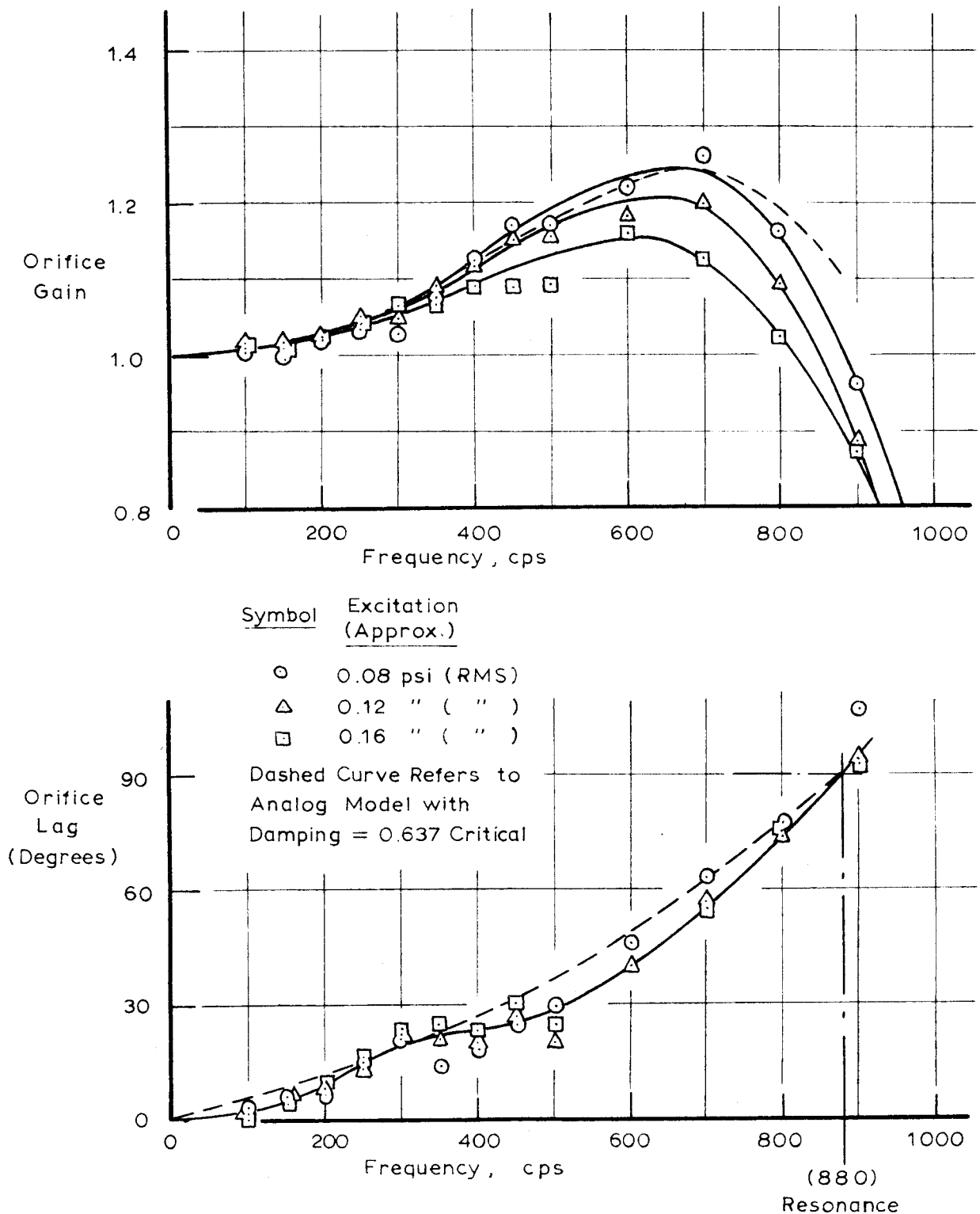
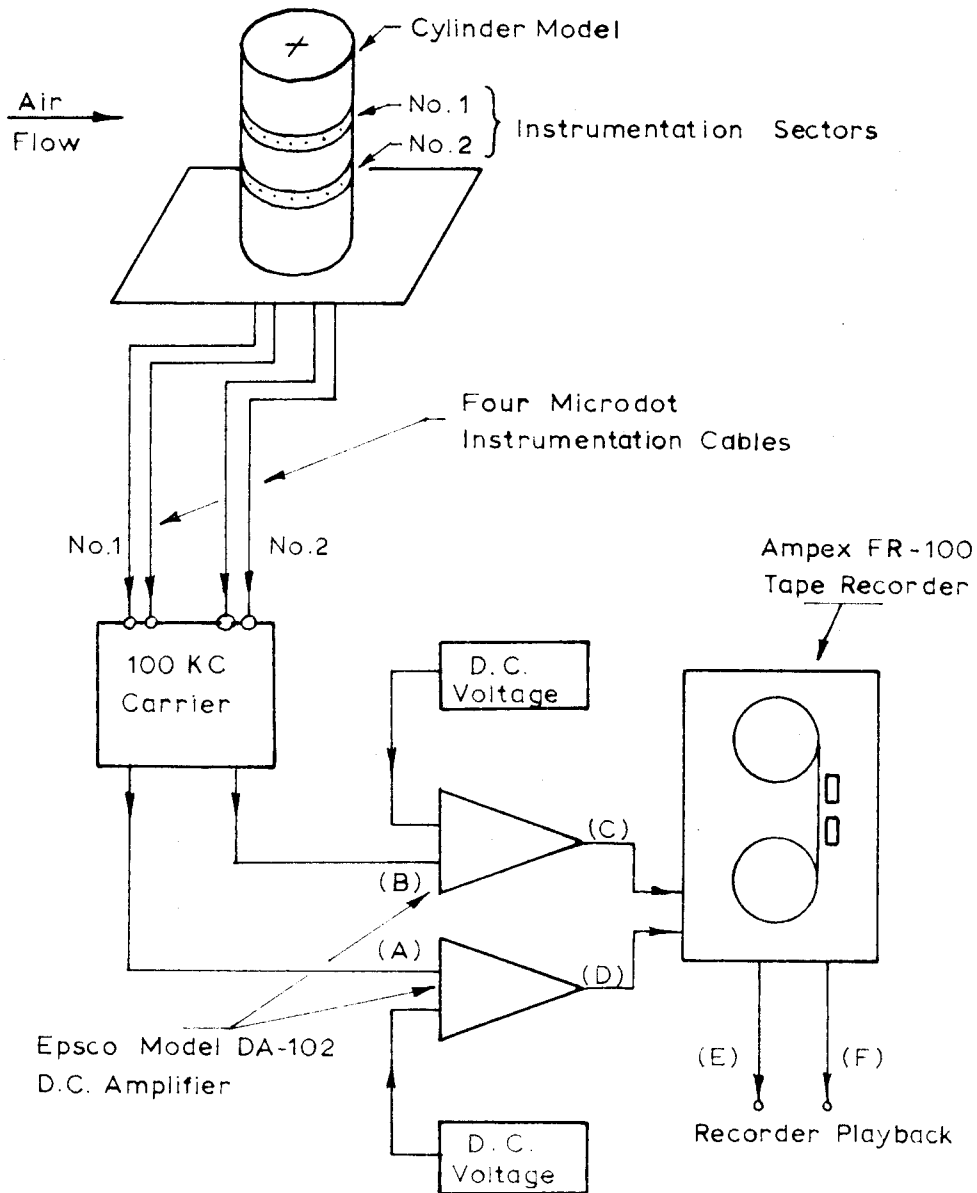Figure A.9    Pressure Orifice Response Traits

108
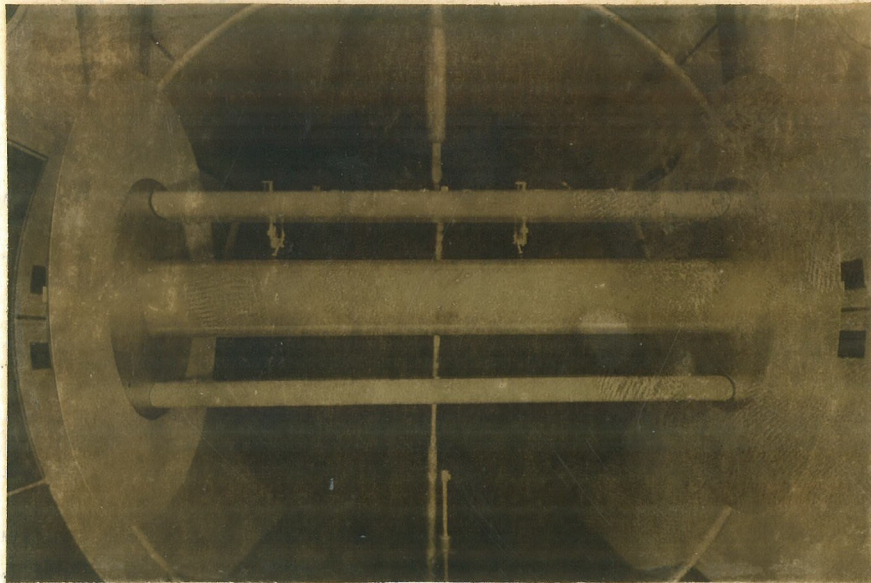


a. Front View



b. Rear View

Figure A.10     Cylinder Model with End Plates

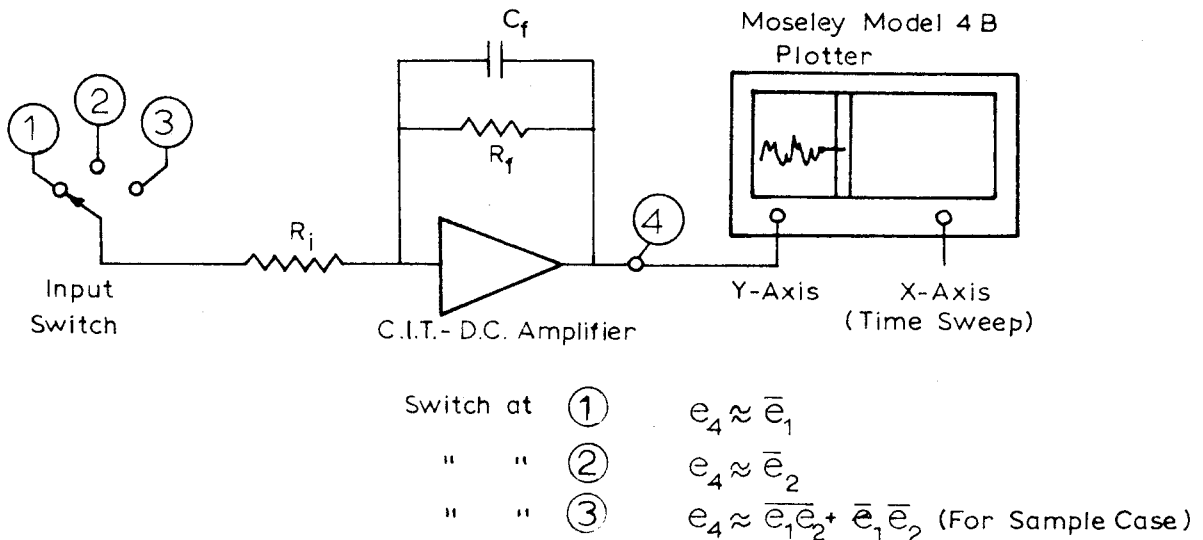Figure B.1     Schematic of Data Recording Circuitry
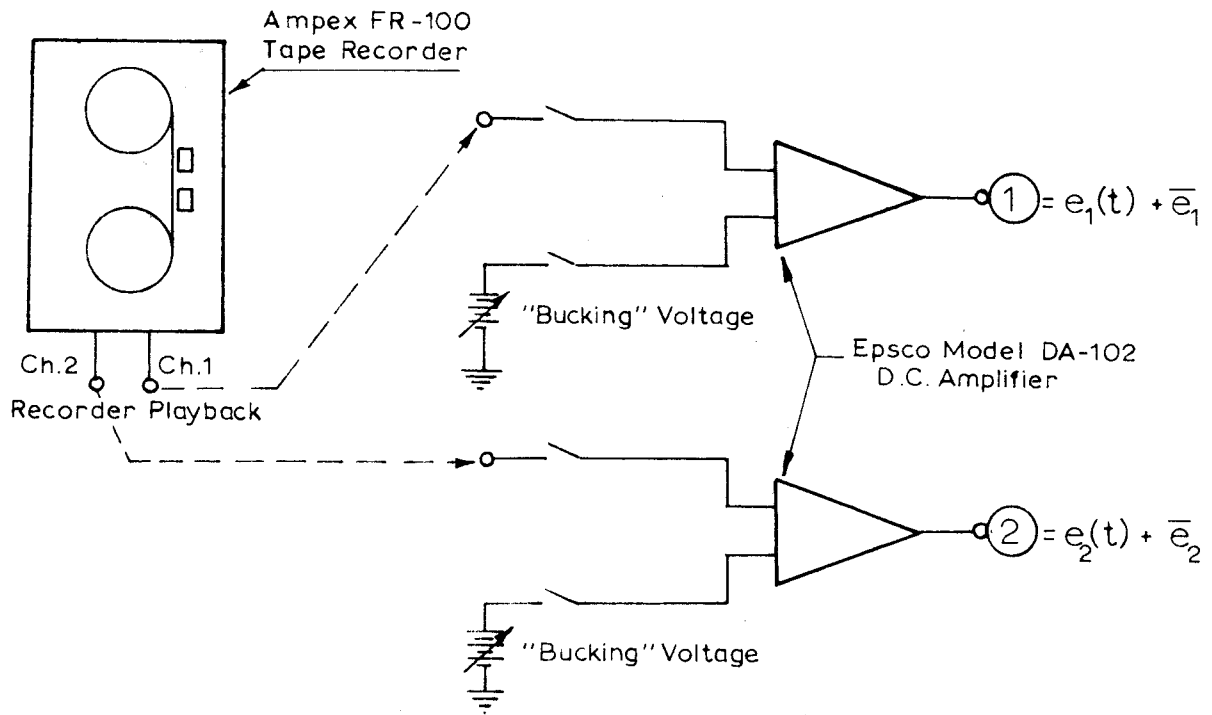
A. Amplifying Circuits
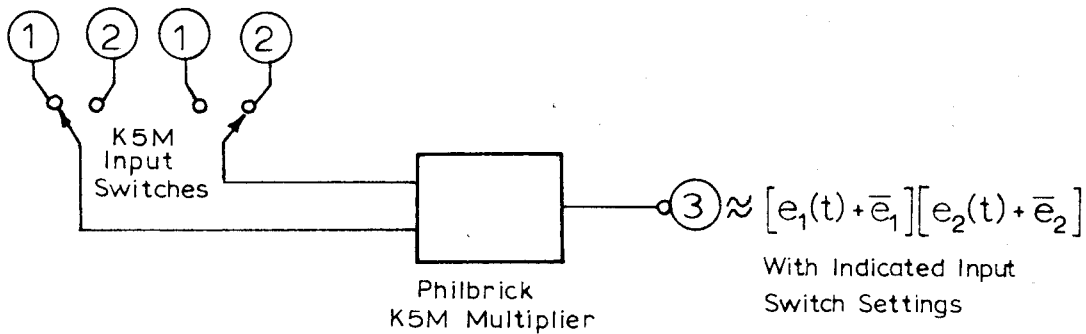
B. Multiplying Circuits

C. Time Averaging Circuit

Switch at ①　$e_4 \approx \bar{e}_1$

"　"　②　$e_4 \approx \bar{e}_2$

"　"　③　$e_4 \approx \overline{e_1 e_2} + \bar{e}_1 \bar{e}_2$ (For Sample Case)

Figure B.2　Schematic of Analog Circuitry